

MAGNETIC NANOSTRUCTURED GRAPHENE

ULRIK SVANBORG MØLLER

2013
NANOPHYSICS AND -MATERIALS
MASTER'S THESIS



AALBORG UNIVERSITY
DENMARK

Magnetic Nanostructured Graphene

Master's thesis by
Ulrik Svanborg Møller

Supervisor: Professor Thomas Garm Pedersen
Aalborg University, Skjernvej 4A, DK-9220 Aalborg Øst
Institute of Physics and Nanotechnology

English abstract

Electronic properties of nanostructured graphene are determined in the framework of a third nearest neighbour mean field Hubbard model. Band gaps and magnetic ground states of 0D graphene flakes, 1D graphene nanoribbons and 2D triangular graphene antidots with hexagonal holes are considered. Structures with sublattice imbalance are found to be ferromagnetic, while for balanced sublattices we identify a critical size above which the ground state is antiferromagnetic. The antiferromagnetic ground state increases the band gap, giving large band gaps with a profound effect on the optical response. Finally, we examine the stability of the antiferromagnetic states for increased temperature and doping. We find the structures to depolarize for $T \sim 1000$ K and doping $\sim 1\%$ impurities.

Danish abstract

Elektroniske egenskaber af nanostruktureret grafen bestemmes med en tredje nærmeste nabo middelfelt Hubbard model. Båndgab og magnetisk grundtilstand bestemmes for 0D grafen flager, 1D grafen nanobånd og 2D triangulære grafen antidots med hexagonelle huller. Strukturer med undergitre i ubalance er ferromagnetiske, mens en kritisk størrelse bestemmes for balancerede undergitre. Strukturer større end denne er antiferromagnetiske. Den antiferromagnetiske grundtilstand øger båndgabet, hvilket har en stor effekt på den optiske respons. Stabiliteten af antiferromagnetiske tilstande undersøges for øget temperatur og doping. For $T \sim 1000$ K og doping $\sim 1\%$ urenheder afpolariseres strukturen.

submitted on the 10th of July 2013

Number of pages: 81

Number of appendices: 2

Preface

This master's thesis considers the subject of nanostructured graphene in the framework of the mean field Hubbard model. The thesis consists of 4 chapters and 2 appendices. The first chapter introduces the state of the art of nanostructured graphene. The second chapter introduces the Hubbard model and methods for solving the model. It is described how the model was implemented and solved numerically. The third chapter presents and discusses the results. Results are presented for 0D, 1D and 2D structures. The conclusion is found in chapter 4.

In appendix A the key concepts of the second quantization are introduced. Appendix B consists of an article made in collaboration with Mads Lund Trolle and Thomas Garm Pedersen. The article considers a subset of the results from chapter 3 in addition to DFT results.

Citations are denoted in square brackets, where the number corresponds to a publication in the bibliography. Equations are referenced as (1.1). Vectors are represented as \mathbf{r} , matrices are denoted \mathbf{M} and operators are shown as \hat{O} .

I would like to thank the following people for their support: Ph.D. fellow Mads Lund Trolle for many interesting discussions and proofreading the manuscript. Ph.D. fellow Lasse Christiansen for proofreading the manuscript. Palle Wolter for designing the front page.

Contents

Contents	v
1 Introduction	1
2 Methods	3
2.1 Hubbard Model	3
2.2 Implementation	16
3 Results and discussion	23
3.1 Ribbons	23
3.2 Nanoflakes	32
3.3 Triangular Antidot Lattices	38
4 Conclusion	53
Bibliography	55
A Second Quantization	61
B Large and stable band gaps in spin-polarized graphene antidot lattices	67

Chapter 1

Introduction

Graphene is the first stable truly 2 dimensional material discovered and consists of a single layer of carbon atoms. Its discovery in 2004 was rewarded the Nobel prize in physics[1]. Graphene appears to be a new wonder material for physicists, chemists and engineers, with a number of properties ranging from e.g. high electron mobility, transparency, flexibility and high mechanical strength [2]. This combination of many unique properties in a single material may allow the emergence of new, disruptive technologies, e.g. printable and flexible electronics. The material is also interesting from a purely scientific point of view with a linear dispersion reminiscent of massless relativistic particles.

Graphene can be manufactured in a number of ways. When graphene was first discovered it was mechanically exfoliated from graphite in what was to become known as the duct tape method. However, in order to introduce graphene to commercial markets the production must be scalable for mass production and the quality must be sufficient for the intended purpose. Several production methods are currently being developed based on either exfoliation of graphite samples or growth of graphene on a substrate. Using chemical vapour deposition (CVD) on copper substrates large area graphene samples have been produced[3]. Another method, synthesis on silicon carbide (SiC), allows for domain sizes up to hundreds of micrometers and control of the number of graphene layers grown. In order to improve the quality of the produced graphene the domain size, number of layers and doping level must be controlled. [2]

Graphene has been suggested as a promising candidate for production of nanoscale transistors. However, in order to use graphene as a transistor a major challenge must be overcome: The introduction of a band gap. Pristine graphene is a semimetal with a vanishing band gap, and thus it

will be impossible to turn the transistor off at ambient temperatures by utilizing conventional Field Effect Transistor designs. [4, 5]

It has been shown experimentally that a band gap can be introduced in graphene by confinement of the structure, in particular by patterning the structure into one dimensional graphene nanoribbons (GNRs) [6–8]. Theoretical studies of GNRs predict a band gap opening which depends on the width of the ribbon and the type of the edge [9, 10]. For zigzag edges a peculiar antiferromagnetic ground state is found. Experimentally, the presence of localized states on the edge of GNRs have been confirmed in agreement with theoretical predictions [11].

Another method for introducing a band gap in graphene is the introduction of a periodic array of holes in the structure. These structures are known as graphene antidot lattices (GALs) and can be produced with holes in the sub 100 nm size [12–15]. While holes fabricated with lithographic methods are expected to have irregular hole shapes it has been found that annealing will allow the edges to reconstruct to armchair or zigzag edges [16, 17]. For two dimensional patterning spin polarization has been observed [18, 19].

Theoretically the band gap of GALs have been determined for different geometries and holes [20–27]. For armchair edges the band gap determined using mean field methods are in agreement with less computationally demanding tight binding calculations. For zigzag edges a band gap is found to open for some structures using mean field methods.

In this work we strive to systematically examine the dependence of the band gap of GALs on the unit cell dimensions. This will be done in the framework of a mean field model capturing the intricate spin behavior predicted by DFT calculations. The main focus will be on graphene nanostructures with zigzag edges. To determine properties of unit cells with thousands of atoms the computational demands of the DFT method are excessive. We thus choose the Hubbard model, where the computational demands are significantly lowered, but the interesting spin properties can still be examined.

Methods

2.1 Hubbard Model

The Hubbard model is an idealized model for strongly interacting electrons in a solid. It is a tight binding model with on-site Coulomb interactions. It was originally developed to examine ferromagnetic properties originating from the Coulomb interaction[28]. The Coulomb interaction is independent of electron spin and does not favor any magnetic ordering. Thus ferromagnetic properties arise because of quantum mechanical interactions between electrons.

2.1.1 Tight-binding

We consider a lattice of N_s atoms. The nuclei are fixed at positions \mathbf{R}_n . The electrons of interest for electronic and optical properties are the electrons which can be excited by low amounts of energy, the valence electrons. The core electrons screen the attractive potential between the valence electrons and the core and can be modeled using an appropriate pseudo potential centered at \mathbf{R}_n . The Hamiltonian of a single valence electron is then

$$\hat{H} = -\frac{\hbar^2}{2m}\nabla^2 + \sum_n^{N_s} V(\mathbf{r} - \mathbf{R}_n). \quad (2.1)$$

In the case of infinitely separated atoms the eigenfunction of the Hamiltonian is a linear combination of atomic orbitals (LCAO) centered at the lattice sites. In the tight binding method the electrons are assumed to be tightly bound to a single atom with limited interaction with other atoms in the lattice. Thus it is assumed that the electron wave function is spanned

2. METHODS

by a basis of atomic orbitals, and the molecular orbital is then a linear combination of atomic orbitals centered at each lattice site \mathbf{R}_n ,

$$\psi(\mathbf{r}) = \sum_n^N c_n \varphi_n(\mathbf{r} - \mathbf{R}_n), \quad (2.2)$$

where φ is an atomic orbital, the index n is a composite index of the orbital type and lattice site and N is the number of states in the basis. To determine the coefficients $c_n \in \mathbb{C}$ the electronic energy,

$$E = \frac{\langle \psi | \hat{H} | \psi \rangle}{\langle \psi | \psi \rangle}, \quad (2.3)$$

is minimized with respect to the coefficients c_n . The terms in equation (2.3) are quadratic in c_n , so taking the partial derivative with respect to c_n and equating to zero results in a linear equation [29]. This is the secular equation

$$\sum_n^N (H_{m,n} - ES_{m,n})c_n = 0, \quad m = 1, 2, \dots, N, \quad (2.4)$$

where $H_{m,n}$ is the Hamiltonian matrix element of the atomic orbitals φ_m and φ_n

$$H_{m,n} = \langle \varphi_m | \hat{H} | \varphi_n \rangle = \int \varphi_m^*(\mathbf{r} - \mathbf{R}_m) \hat{H} \varphi_n(\mathbf{r} - \mathbf{R}_n) d\mathbf{r}, \quad (2.5)$$

and $S_{m,n}$ is the overlap matrix element

$$S_{m,n} = \langle \varphi_m | \varphi_n \rangle = \int \varphi_m^*(\mathbf{r} - \mathbf{R}_m) \varphi_n(\mathbf{r} - \mathbf{R}_n) d\mathbf{r}.$$

The secular equation (2.4) can furthermore be expressed in the matrix form

$$\mathbf{H}\mathbf{c} = E\mathbf{S}\mathbf{c}, \quad (2.6)$$

where \mathbf{H} is the Hamiltonian matrix, \mathbf{S} is the overlap matrix and \mathbf{c} is a vector of the coefficients c_n . Ignoring the trivial solution $\mathbf{c} = 0$, solving the equation results in N values of E and N linearly independent choices of \mathbf{c} . The coefficients \mathbf{c} are chosen to obey the normalization condition

$$\langle \psi | \psi \rangle = \sum_m^N \sum_n^N c_m^* c_n S_{m,n} = 1.$$

Evaluating the matrix elements leads to three types of integrals, one-, two- and three-center integrals depending on the number of atomic sites involved in the integration. The matrix elements of the kinetic energy and the overlap result in one- and two-center integrals, while the matrix elements of the potential energy result in up to three-center integrals. Solving the integrals is eased considerably by exploiting the symmetry of the atomic orbitals in the basis. In the Slater-Koster approximation [30] the Hamiltonian matrix elements are approximated with two-center matrix elements and fitted to theoretical or empirical data.

Crystal Structure

Utilizing the crystal symmetry the number of states in the basis N can be reduced considerably. The crystal structure is defined by the translation vector

$$\mathbf{T} = \sum_i^D n_i \mathbf{a}_i, \quad n_i \in \mathbb{Z},$$

where D is the dimensionality of the crystal and \mathbf{a}_i are the primitive vectors spanning the unit cell. The positions of the atoms in the unit cell will be denoted $\boldsymbol{\tau}_m$. Similarly the reciprocal lattice is defined by the reciprocal lattice vector

$$\mathbf{G} = \sum_i^D m_i \mathbf{b}_i, \quad m_i \in \mathbb{Z},$$

where the primitive reciprocal lattice vectors \mathbf{b}_i are defined by

$$\mathbf{a}_i \cdot \mathbf{b}_j = 2\pi\delta_{ij}.$$

The Brillouin Zone is found from \mathbf{G} as the Wigner-Seitz cell. Any physical quantity $f(\mathbf{r})$ is invariant for a translation \mathbf{T} . The sites of the reciprocal lattice \mathbf{G} are the points for which the Fourier components of the Fourier transform of $f(\mathbf{r})$ are non-zero.

The electron density must be conserved for a translation \mathbf{T} , and thus the wavefunction must be conserved besides a phase change. According to the Bloch theorem this phase change is

$$\psi(\mathbf{r} + \mathbf{T}) = e^{i\mathbf{k}\cdot\mathbf{T}} \psi(\mathbf{r}), \quad (2.7)$$

where \mathbf{k} is the wave vector. When evaluating equations with the phase \mathbf{k} it is sufficient to consider \mathbf{k} in the first Brillouin Zone as all possible eigenstates are specified there, because $e^{i(\mathbf{k}+\mathbf{G})\cdot\mathbf{T}} = e^{i\mathbf{k}\cdot\mathbf{T}}$. [31, 32]

2. METHODS

Incorporating the periodicity of crystals in Tight Binding calculations is done by replacing the atomic orbitals in the LCAO (2.2) by Bloch sums of atomic orbitals defined by

$$\varphi_{n,\mathbf{k}}(\mathbf{r}) = A_{n,\mathbf{k}} \sum_{\mathbf{T}} e^{i\mathbf{k}\cdot\mathbf{T}} \varphi_n[\mathbf{r} - (\mathbf{T} + \boldsymbol{\tau}_n)], \quad (2.8)$$

where $A_{n,\mathbf{k}}$ is a normalization constant. Notice that $\mathbf{T} + \boldsymbol{\tau}_n = \mathbf{R}_n$. The Bloch sums satisfy the Bloch theorem (2.7) and are orthonormal with respect to \mathbf{k} . Assuming the atomic orbitals are orthonormal, the normalization constant is determined

$$\begin{aligned} 1 &= \langle \varphi_{n,\mathbf{k}} | \varphi_{n,\mathbf{k}} \rangle \\ &= |A_{n,\mathbf{k}}|^2 \sum_{\mathbf{T}_1, \mathbf{T}_2} e^{-i\mathbf{k}\cdot\mathbf{T}_1} e^{i\mathbf{k}\cdot\mathbf{T}_2} \langle \varphi_n[\mathbf{r} - (\boldsymbol{\tau}_n + \mathbf{T}_1)] | \varphi_n[\mathbf{r} - (\boldsymbol{\tau}_n + \mathbf{T}_2)] \rangle \\ &= |A_{n,\mathbf{k}}|^2 \sum_{\mathbf{T}_1, \mathbf{T}_2} e^{i\mathbf{k}\cdot(\mathbf{T}_2 - \mathbf{T}_1)} \delta_{\mathbf{T}_1, \mathbf{T}_2} \\ &= |A_{n,\mathbf{k}}|^2 N_{\mathbf{T}} \Leftrightarrow \\ |A_{n,\mathbf{k}}|^2 &= \frac{1}{N_{\mathbf{T}}}. \end{aligned}$$

$N_{\mathbf{T}}$ is the number of unit cells included in the sum. Thus the magnitude of $A_{n,\mathbf{k}}$ is $N_{\mathbf{T}}^{-1/2}$ independent of n and \mathbf{k} . By replacing the atomic orbitals in (2.2) with Bloch sums, the electron wavefunction is

$$\psi_{\mathbf{k}}(\mathbf{r}) = \sum_n^N c_{n,\mathbf{k}} \varphi_{n,\mathbf{k}}(\mathbf{r}) = \sum_n^N c_{n,\mathbf{k}} \sum_{\mathbf{T}} e^{i\mathbf{k}\cdot\mathbf{T}} \varphi_n[\mathbf{r} - (\mathbf{T} + \boldsymbol{\tau}_n)],$$

where the normalization constant is contained in the coefficients $c_{n,\mathbf{k}}$. Alternatively, by choosing the phase of $A_{n,\mathbf{k}}$ as $e^{i\mathbf{k}\cdot\boldsymbol{\tau}_n}$, the wavefunction will be

$$\psi_{\mathbf{k}}(\mathbf{r}) = \sum_n^N c_{n,\mathbf{k}} \sum_{\mathbf{T}} e^{i\mathbf{k}\cdot(\mathbf{T} + \boldsymbol{\tau}_n)} \varphi_n[\mathbf{r} - (\mathbf{T} + \boldsymbol{\tau}_n)].$$

Noting that $\mathbf{R}_n = \mathbf{T} + \boldsymbol{\tau}_n$ this corresponds to summing over N atomic orbitals per unit cell.

The matrix elements between the atomic orbitals in the unit cell with $\mathbf{T} = \mathbf{0}$ and any unit cell is introduced

$$\begin{aligned} H_{m,n}(\mathbf{T}) &= \int \varphi_m^*(\mathbf{r} - \boldsymbol{\tau}_m) \hat{H} \varphi_n[\mathbf{r} - (\mathbf{T} + \boldsymbol{\tau}_n)] d\mathbf{r}, \\ S_{m,n}(\mathbf{T}) &= \int \varphi_m^*(\mathbf{r} - \boldsymbol{\tau}_m) \varphi_n[\mathbf{r} - (\mathbf{T} + \boldsymbol{\tau}_n)] d\mathbf{r}. \end{aligned} \quad (2.9)$$

The Hamiltonian matrix element of Bloch sums is now evaluated

$$H_{m,n}(\mathbf{k}) = \langle \varphi_{m,\mathbf{k}} | \hat{H} | \varphi_{n,\mathbf{k}} \rangle = A_{m,\mathbf{k}}^* A_{n,\mathbf{k}} \sum_{\mathbf{T}_1, \mathbf{T}_2} e^{i\mathbf{k} \cdot (\mathbf{T}_2 - \mathbf{T}_1)} \langle \varphi_m[\mathbf{r} - (\mathbf{T}_1 + \boldsymbol{\tau}_m)] | \hat{H} | \varphi_n[\mathbf{r} - (\mathbf{T}_2 + \boldsymbol{\tau}_n)] \rangle.$$

As all lattice points are indistinguishable all terms in the sum over \mathbf{T}_1 are equal. Thus \mathbf{T}_1 is chosen as $\mathbf{0}$ and the result is

$$H_{m,n}(\mathbf{k}) = A_{m,\mathbf{k}}^* A_{n,\mathbf{k}} N_{\mathbf{T}} \sum_{\mathbf{T}_2} e^{i\mathbf{k} \cdot \mathbf{T}_2} \langle \varphi_m(\mathbf{r} - \boldsymbol{\tau}_m) | \hat{H} | \varphi_n[\mathbf{r} - (\mathbf{T}_2 + \boldsymbol{\tau}_n)] \rangle = A_{m,\mathbf{k}}^* A_{n,\mathbf{k}} N_{\mathbf{T}} \sum_{\mathbf{T}} e^{i\mathbf{k} \cdot \mathbf{T}} H_{m,n}(\mathbf{T}).$$

Similar arguments can be used to evaluate the overlap matrix element $S_{m,n}(\mathbf{k})$. The magnitude of $A_{n,\mathbf{k}}$ was found to be $N_{\mathbf{T}}^{-1/2}$ which cancels the factor of $N_{\mathbf{T}}$. So for $A_{n,\mathbf{k}} = N_{\mathbf{T}}^{-1/2}$ the matrix elements are

$$H_{m,n}(\mathbf{k}) = \sum_{\mathbf{T}} e^{i\mathbf{k} \cdot \mathbf{T}} H_{m,n}(\mathbf{T}), \quad S_{m,n}(\mathbf{k}) = \sum_{\mathbf{T}} e^{i\mathbf{k} \cdot \mathbf{T}} S_{m,n}(\mathbf{T}). \quad (2.10)$$

Alternatively, by choosing the normalization constant as $A_{n,\mathbf{k}} = e^{i\mathbf{k} \cdot \boldsymbol{\tau}_n} N_{\mathbf{T}}^{-1/2}$ the matrix elements become

$$H_{m,n}(\mathbf{k}) = \sum_{\mathbf{T}} e^{i\mathbf{k} \cdot \Delta \mathbf{R}(\mathbf{T})} H_{m,n}(\mathbf{T}), \quad S_{m,n}(\mathbf{k}) = \sum_{\mathbf{T}} e^{i\mathbf{k} \cdot \Delta \mathbf{R}(\mathbf{T})} S_{m,n}(\mathbf{T}), \quad (2.11)$$

where $\Delta \mathbf{R}(\mathbf{T}) = \mathbf{T} + \boldsymbol{\tau}_n - \boldsymbol{\tau}_m$ is the displacement vector between the sites the matrix element (2.9) is evaluated for.

[32]

Many-Electron Wave Function

By solving the matrix equation (2.6) using the matrix elements of equation (2.10) or (2.11) N linearly independent sets of \mathbf{c}_m with corresponding eigenvalues E_m are obtained. The set of wavefunctions $\psi_m(\mathbf{r})$ constitutes a complete basis set of the Hamiltonian (2.1). As the Hamiltonian is independent of spin the $\psi_m(\mathbf{r})$ are doubly degenerate.

The linearly independent spin functions are chosen as eigenfunctions of the \hat{s}_z spin operator and will be denoted $\alpha(\varsigma)$, the spin up function, and $\beta(\varsigma)$, the spin down function. The functions are orthonormal with eigenvalues $\frac{1}{2}\hbar$ and $-\frac{1}{2}\hbar$ respectively. The eigenvalues will be represented with \uparrow and \downarrow . Thus the spinorbitals of the Hamiltonian (2.1) are $\psi_{m,\uparrow}(\mathbf{x})$ and $\psi_{m,\downarrow}(\mathbf{x})$, where the argument $\mathbf{x} = \{\mathbf{r}, \varsigma\}$.

2. METHODS

Considering a many-electron system the single-electron Hamiltonian (2.1) will be denoted \hat{h}_i . Ignoring the electron-electron interaction for now, the many-electron Hamiltonian is

$$\hat{H} = \sum_i^{N_e} \hat{h}_i,$$

where N_e is the number of electrons in the system. The many-electron wave function is the Slater determinant of the single-electron states $\psi_{m,\sigma}(\mathbf{x})$. The ground state can be formed by choosing the N_e spin orbitals with the lowest eigenvalues E_m . It is obtained using the anti-symmetrization operator (A.5)

$$\Psi_{GS}(\mathbf{x}_1, \mathbf{x}_2, \dots, \mathbf{x}_{N_e}) = \hat{S}_- \prod_{i=1}^{N_e} \psi_i(\mathbf{x}_i),$$

where i is the electron number and is a composite index for $\{m, \sigma\}$.

Tight Binding in Second Quantization

We consider a lattice consisting of N_s lattice sites which are atomic sites in a solid. The sites are numbered $1, 2, \dots, N_s$. For simplicity we consider a single-orbital model where each atomic site carries a single non-degenerate orbital. Furthermore the atomic orbitals are assumed to be orthogonal, so the overlap matrix \mathbf{S} is identical to the identity matrix \mathbf{I} . In this model the electrons can be thought of as living on the lattice sites and can tunnel to nearby sites.

A single electron state with a fixed spin is a LCAO, which will be denoted

$$\boldsymbol{\varphi} = (\varphi_i)_{i=1,2,\dots,N_s}, \quad (2.12)$$

where $\varphi_i \in \mathbb{C}$ is the vector component for site i and $\boldsymbol{\varphi}$ is thus identical to the vector \mathbf{c} in equation (2.6).

The single electron state can be defined using the fermion creation and annihilation operators defined by equation (A.9). The set of quantum numbers consists of the site index i and the spin quantum number σ . Thus the operator $\hat{c}_{i,\sigma}^\dagger$ creates an electron at site i with spin σ while the operator $\hat{c}_{i,\sigma}$ annihilates an electron at site i with spin σ . A new set of operators are defined

$$\hat{C}_\sigma^\dagger(\boldsymbol{\varphi}) = \sum_i^{N_s} \varphi_i \hat{c}_{i,\sigma}^\dagger, \quad \hat{C}_\sigma(\boldsymbol{\varphi}) = \sum_i^{N_s} (\varphi_i)^* \hat{c}_{i,\sigma},$$

where φ is a single-electron state given by equation (2.12). These operators satisfy the anticommutator relations

$$\begin{aligned}\{\hat{C}_\sigma^\dagger(\varphi), \hat{C}_\tau(\psi)\} &= \delta_{\sigma,\tau} \langle \varphi, \psi \rangle, \\ \{\hat{C}_\sigma(\varphi), \hat{C}_\tau(\psi)\} &= \{\hat{C}_\sigma^\dagger(\varphi), \hat{C}_\tau^\dagger(\psi)\} = 0,\end{aligned}$$

for any φ, ψ and $\sigma, \tau = \uparrow, \downarrow$. $\langle \varphi, \psi \rangle$ is the inner product between discrete vector states φ and ψ . If the states φ and ψ are orthonormalized the operators $\hat{C}_\sigma^\dagger(\varphi)$ and $\hat{C}_\sigma(\varphi)$ will obey the anticommutator relations (A.6) and (A.7), and are thus fermion creation and annihilation operators which creates or annihilates an electron in state φ with spin σ . The single-electron state φ with spin σ is thus obtained by

$$\Psi = \hat{C}_\sigma^\dagger(\varphi)|0\rangle.$$

The tunneling amplitude that an electron tunnels/hops from site j to i with $i \neq j$ is denoted $t_{i,j}$. By tunneling the electron is annihilated at site j and created at site i . The hopping Hamiltonian is then

$$\hat{H}_{hop} = \sum_{i,j,\sigma} t_{i,j} \hat{c}_{i,\sigma}^\dagger \hat{c}_{j,\sigma}. \quad (2.13)$$

The Hamiltonian is a one-electron operator in second quantization as described in equation (A.10). $t_{i,j}$ are matrix elements and corresponds to the Hamiltonian matrix elements from equation (2.5). The single electron Schrödinger equation is

$$\hat{H}_{hop} \Psi = E \Psi.$$

The equation has N_s eigenvalues E_j with corresponding eigenvectors $\varphi^{(j)}$. The eigenvectors are orthogonal $\langle \varphi^{(j)}, \varphi^{(k)} \rangle = \delta_{j,k}$. The N_e -electron wavefunction of the system is then

$$\hat{C}_\sigma^\dagger(\varphi^{(1)}) \dots \hat{C}_\sigma^\dagger(\varphi^{(N_e)})|0\rangle.$$

[33]

2.1.2 Electron-Electron Interaction

When adding multiple electrons to a system the electrons will repel each other and the electron-electron repulsion must be included in the Hamiltonian. Thus the one-electron \hat{H}_{hop} (2.13) is modified by inclusion of the electron-electron repulsion. The operator is a two-electron operator which

2. METHODS

in second quantization is formulated as in equation (A.11). The Hamiltonian is then

$$\hat{H} = \sum_{i,j,\sigma} t_{i,j} \hat{c}_{i,\sigma}^\dagger \hat{c}_{j,\sigma} + \frac{1}{2} \sum_{\sigma_1,\sigma_2} \sum_{i,j,k,l} \left\langle i, j \left| \frac{e^2}{4\pi\epsilon_0 |\mathbf{r}_2 - \mathbf{r}_1|} \right| k, l \right\rangle \hat{c}_{i,\sigma_1}^\dagger \hat{c}_{j,\sigma_2}^\dagger \hat{c}_{l,\sigma_2} \hat{c}_{k,\sigma_1}.$$

The two-electron matrix element corresponds to (A.12). It involves 4 atomic orbitals centered on the lattice sites i, j, k and l and can be written

$$\left\langle i, j \left| \frac{e^2}{4\pi\epsilon_0 |\mathbf{r}_2 - \mathbf{r}_1|} \right| k, l \right\rangle = \frac{e^2}{4\pi\epsilon_0} \int \int \frac{\varphi^*(\mathbf{r}_2 - \mathbf{R}_i) \varphi(\mathbf{r}_2 - \mathbf{R}_k) \varphi^*(\mathbf{r}_1 - \mathbf{R}_j) \varphi(\mathbf{r}_1 - \mathbf{R}_l)}{|\mathbf{r}_2 - \mathbf{r}_1|} d\mathbf{r}_2 d\mathbf{r}_1.$$

In the Hubbard model only the on-site matrix element is included and all others are ignored. Thus the two-electron Coulomb interaction is treated as a short range interaction. This is justified by the consideration that the coulomb force is largest when two electrons are at the minimum possible distance. The Hubbard model is thus a minimum model for studying properties of strongly interacting electron systems. By defining the value

$$U = \left\langle i, i \left| \frac{e^2}{4\pi\epsilon_0 |\mathbf{r}_2 - \mathbf{r}_1|} \right| i, i \right\rangle,$$

the on-site two-electron interaction is

$$\hat{H}_{int} = \frac{U}{2} \sum_{i,\sigma_1,\sigma_2} \hat{c}_{i,\sigma_1}^\dagger \hat{c}_{i,\sigma_2}^\dagger \hat{c}_{i,\sigma_2} \hat{c}_{i,\sigma_1} = U \sum_i \hat{n}_{i,\uparrow} \hat{n}_{i,\downarrow}, \quad (2.14)$$

where (A.8) was used. The Hubbard Hamiltonian is then

$$\hat{H} = \hat{H}_{hop} + \hat{H}_{int} = \sum_{i,j,\sigma} t_{i,j} \hat{c}_{i,\sigma}^\dagger \hat{c}_{j,\sigma} + U \sum_i \hat{n}_{i,\uparrow} \hat{n}_{i,\downarrow}. \quad (2.15)$$

When solving the model there are a number of symmetries which can be exploited when choosing the basis sets. The Hubbard Hamiltonian commutes with the operators for the total particle number N_e and the total spin. As the total particle number is $N_e = N_\uparrow + N_\downarrow$ and the total spin is $S_z = (N_\uparrow - N_\downarrow)/2$ conservation of spin and electron number corresponds to conservation of N_\uparrow and N_\downarrow . The model can then be solved with basis states spanning the Hilbert space for a fixed N_\uparrow and N_\downarrow . Furthermore, for periodic systems the Hamiltonian commutes with the Translation operator, so the basis functions can be chosen as Bloch sums as in equation (2.8).

The Hubbard model can be seen as an approximation of the extended Hubbard model where nonlocal Coulomb matrix elements are considered. It was found by Schüler *et al.* [34] that the effective Hubbard U is reduced by more than 50% compared to a purely local interaction. [28, 33, 35]

Exact Diagonalization

We consider a lattice consisting of 2 atomic sites. The total number of possible electron configurations is 4^{N_s} . However if we fix the number of spin up and down electrons the number of basis states reduces to the number of ways N_σ can be distributed on N_s lattice sites. The number is

$$N_{basis} = \binom{N_s}{N_\uparrow} \binom{N_s}{N_\downarrow}, \quad (2.16)$$

where $\binom{N}{M}$ is a binomial coefficient.

We choose the system at half filling corresponding to $N_e = 2$. The system is chosen to have total spin $S_z = 0$ corresponding to $N_\uparrow = N_\downarrow = 1$. Then the total number of basis states is 4. Choosing the default sorting order of the quantum numbers as sorting by spin index first, then lattice index, the basis states will be represented in the occupation number representation $|n_{1,\uparrow}, n_{2,\uparrow}, n_{1,\downarrow}, n_{2,\downarrow}\rangle$. The basis states are

$$\varphi_1 = |0, 1; 1, 0\rangle, \quad \varphi_2 = |1, 0; 1, 0\rangle, \quad \varphi_3 = |1, 0; 0, 1\rangle, \quad \varphi_4 = |0, 1; 0, 1\rangle.$$

We are now ready to consider the Hamiltonian matrix for the Hubbard Hamiltonian (2.15) operating on a linear combination of the basis states. The matrix elements $t_{i,j}$ are chosen as $t_{1,1} = t_{2,2} = 0$ and $t_{1,2} = t_{2,1} = -t$. The values of t and U are real and positive. The Hamiltonian matrix is then

$$\mathbf{H} = \begin{vmatrix} 0 & -t & 0 & -t \\ -t & U & -t & 0 \\ 0 & -t & 0 & -t \\ -t & 0 & -t & U \end{vmatrix}.$$

The corresponding eigenvalue equation is $\mathbf{H}\mathbf{c} = E\mathbf{c}$. This equation has the characteristic equation and eigenvalues

$$E(U - E)(E(U - E) + 4t^2) = 0 \Leftrightarrow E_0 = \frac{U - \sqrt{U^2 + 16t^2}}{2}, \quad E_1 = 0, \quad E_2 = U, \quad E_3 = \frac{U + \sqrt{U^2 + 16t^2}}{2} \quad (2.17)$$

2. METHODS

The ground state of the system has the energy E_0 . The eigenvector for this eigenvalue is

$$\mathbf{c}_0 = N(2t, -E_0, 2t, -E_0),$$

where N is a normalization constant. After normalization the eigenvector describes the ground state wave function. Notice that for $U = 0$ all basis states are weighted equally. Reasonable choices of t and U for graphene are $t = 2.7$ eV and $U = 2.0$ eV. For these constants the eigenvector is

$$\mathbf{c}_0 = (0.544, 0.452, 0.544, 0.452).$$

For the ground state the eigenvalues of the number operator $\hat{n}_{i,\sigma}$ is 0.5 for all combinations of i and σ . Thus in the ground state the electrons are equally distributed.

The probability of observing the system in state φ_1 or φ_3 is 0.591 and is the probability that the electrons are located at different atoms. Thus the introduction of the on-site electron-electron repulsion has made it energetically favourable for the electrons to be at different atoms. This correlation between the electrons lowers the total energy.

Using the Exact Diagonalization approach it is possible to solve the Hubbard model exactly. However the size of the basis set (2.16) increases rapidly with system size. For a system with 20 sites at half filling the number of basis states is on the order of 10^{10} . While the matrix \mathbf{H} is very sparse the computational demands are excessive. Thus in order to reduce the size of the basis sets it is essential to exploit symmetries of the system. For larger systems it is desirable to use approximate methods. [35]

2.1.3 Mean Field Method

As it was seen for the system with 2 electrons the positions of the electrons correlate in the Hubbard model. In a mean field method the electron-electron interaction is included as an interaction between the electron and the mean density of electrons in the system. In this scheme correlations are included only on average, but the resulting Hamiltonian is a one-electron operator allowing a smaller basis set to be chosen.

in the mean field method, the number operator is replaced by

$$\hat{n}_{i,\sigma} = \langle n_{i,\sigma} \rangle + \delta \hat{n}_{i,\sigma},$$

which is the mean field $\langle n_{i,\sigma} \rangle$ plus a small correction. Thus evaluating

$$\begin{aligned}\hat{n}_{i,\uparrow}\hat{n}_{i,\downarrow} &= \langle n_{i,\uparrow} \rangle \langle n_{i,\downarrow} \rangle + \delta\hat{n}_{i,\uparrow}\langle n_{i,\downarrow} \rangle + \delta\hat{n}_{i,\downarrow}\langle n_{i,\uparrow} \rangle + \delta\hat{n}_{i,\uparrow}\delta\hat{n}_{i,\downarrow} \\ &\approx \langle n_{i,\uparrow} \rangle \langle n_{i,\downarrow} \rangle + (\hat{n}_{i,\uparrow} - \langle n_{i,\uparrow} \rangle)\langle n_{i,\downarrow} \rangle + (\hat{n}_{i,\downarrow} - \langle n_{i,\downarrow} \rangle)\langle n_{i,\uparrow} \rangle \\ &\approx \hat{n}_{i,\uparrow}\langle n_{i,\downarrow} \rangle + \hat{n}_{i,\downarrow}\langle n_{i,\uparrow} \rangle - \langle n_{i,\uparrow} \rangle \langle n_{i,\downarrow} \rangle,\end{aligned}$$

it is found that by neglecting the second order term $\delta\hat{n}_{i,\uparrow}\delta\hat{n}_{i,\downarrow}$ the interaction operator (2.14) can be approximated as the interaction with the mean of the number operator. The Hamiltonian of the Hubbard model in the mean field approximation is then

$$\hat{H} = \sum_{i,j,\sigma} t_{i,j} \hat{c}_{i,\sigma}^\dagger \hat{c}_{j,\sigma} + U \sum_i (\hat{n}_{i,\uparrow}\langle n_{i,\downarrow} \rangle + \hat{n}_{i,\downarrow}\langle n_{i,\uparrow} \rangle - \langle n_{i,\uparrow} \rangle \langle n_{i,\downarrow} \rangle), \quad (2.18)$$

which is a one-electron operator. In order to find the eigenstates of the operator the mean of the number operator must be found. The average occupation of site i is the electron density of site i , and thus

$$\langle n_{i,\sigma} \rangle = \sum_j f_{FD}(E_{j,\sigma}) \left| \psi_{i,\sigma}^{(j)} \right|^2, \quad (2.19)$$

where f_{FD} is the Fermi-Dirac distribution function and $E_{j,\sigma}$ is the eigenvalue of the eigenstate $\psi_{i,\sigma}^{(j)}$. The electron density is then obtained by starting with an initial guess and iterating until self-consistently, that is

$$\mathbf{n}_{old} = \mathbf{n}_{new}. \quad (2.20)$$

As the Hamiltonian is a single electron operator the total energy of the many-electron system is found from

$$E_{tot} = \sum_{j,\sigma} f_{FD}(E_{j,\sigma}) \epsilon_{j,\sigma} - U \sum_i \langle n_{i,\uparrow} \rangle \langle n_{i,\downarrow} \rangle. \quad (2.21)$$

We now have the necessary tools for solving the Hubbard model and obtaining the electron density. For describing the spin properties of the system we introduce the local spin polarization

$$p_i = \langle n_{i,\uparrow} \rangle - \langle n_{i,\downarrow} \rangle. \quad (2.22)$$

p_i is thus the number of unpaired electrons on site i .
[36, 37]

Example: Two-electron system

We now revisit the model system solved using exact diagonalization and solve the two-electron system using the mean field approach. The basis states are now one-electron states, and are

$$\varphi_1 = |1, 0; 0, 0\rangle, \quad \varphi_2 = |0, 1; 0, 0\rangle, \quad \varphi_3 = |0, 0; 1, 0\rangle, \quad \varphi_4 = |0, 0; 0, 1\rangle.$$

For the chosen system at half filling the number of basis states is the same as for exact diagonalization. However, in this case the number of basis states scales linearly with the number of lattice sites as

$$N_{basis} = 2N_s,$$

which is a significant improvement over (2.16). The Hamiltonian matrix is

$$\mathbf{H} = \begin{vmatrix} U\langle n_{1,\downarrow} \rangle & -t & 0 & 0 \\ -t & U\langle n_{2,\downarrow} \rangle & 0 & 0 \\ 0 & 0 & U\langle n_{1,\uparrow} \rangle & -t \\ 0 & 0 & -t & U\langle n_{1,\uparrow} \rangle \end{vmatrix}.$$

It is found that the spins only couple through the average electron density, allowing the problem to be broken down to solving 2 characteristic equations of order N_s . The eigenvalues of these equations are

$$(U\langle n_{1,\sigma} \rangle - \epsilon)(U\langle n_{2,\sigma} \rangle - \epsilon) - t^2 = 0 \Leftrightarrow \\ \epsilon = \frac{U \pm \sqrt{4t^2 + U^2 - 4U^2\langle n_{1,\sigma} \rangle\langle n_{2,\sigma} \rangle}}{2}.$$

Assuming the electrons are evenly distributed like for the exact diagonalization method, the lowest energy is found to be $\epsilon_0 = U/2 - t$ with the eigenvector $\mathbf{c}_0 = \sqrt{2}/2(1, 1)$. It was tested that for a different start density the system iterated to evenly distributed electrons. Using equation (2.21), the total energy of the system is

$$E_{tot} = 2\epsilon_0 - U/2 = U/2 - 2t.$$

Using the values $t = 2.7$ eV and $U = 2.0$ eV the total energy of the system is found to be $E_{MF} = -4.40$ eV for the mean field calculation and $E_{ED} = -4.49$ eV for the exact diagonalization calculation. Thus the correlation energy is $E_{cor} = 90$ meV. The same electron density was found using both methods.

Changing units to t , we examine the total energy as a function of the quantity U/t . The energy of the exact diagonalization approach is found

from equation (2.17), while the energy of the mean field approach is found by iterating the electron density until convergence and applying equation (2.21). The results are shown in figure 2.1. For $U = 0$ the energy is equal for the two approaches. While the energy of the MF approach increases linearly with U until $U = 2t$ the ED energy increases slower. For $U = t$ the correlation energy is 4% of the ED energy and for $U = 2t$ it is 19%. Thus the importance of correlation increases significantly with U . At $U = 2t$ the mean field density becomes antiferromagnetic as shown in figure 2.1b. While this decreases the rate of growth of the correlation energy, the electron density is no longer in agreement with the electron density obtained using the ED approach. In fact, the ED electron density remains paramagnetic for all values of U . This demonstrates that for large values of U the effects of correlation cannot be ignored.

In a work by Ijäs and Harju [37], the correlation energy is fitted by an exponential function in a local density approximation approach. For large U this method increases the agreement between the total energy of the system and the ED energy. However, the approach does not increase the agreement between the electron densities for spin unpolarized systems. For highly correlated systems the approximation $\delta\hat{n}_{i,\uparrow}\delta\hat{n}_{i,\downarrow} \approx 0$ is invalid, showing the limits of mean field methods. In the majority of this work we choose $U/t \approx 0.75$ and use the mean field method. For electron-electron interactions of this magnitude it remains to be seen whether magnetic ordering of the ground state is caused by insufficient treatment of electron correlation.

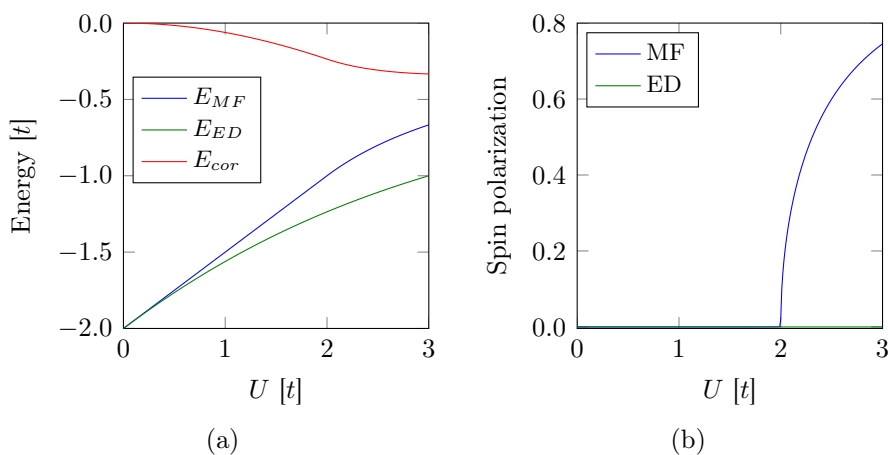


Figure 2.1: Comparison of total energy (a) and local spin polarization of atom 1 (b) of 2 atom, 2 electron system.

2.2 Implementation

In this work 0D, 1D and 2D nanostructured graphene is modeled using the Hubbard model, which is solved using the mean field approximation. In this section the method used for obtaining the electron density is described.

First, a suitable set of basis orbitals must be chosen for describing the electronic properties of interest. The second shell electrons of carbon atoms in graphene are either in sp_2 orbitals, which participate in σ bonding in the graphene plane, or in a p_z orbital participating in π bonding out of plane. The π electrons are loosely bound in a molecular orbital extending across the whole molecule, while the σ electrons are tightly bound. We wish to describe the low energy properties, and thus we choose a basis consisting of a single π orbital per carbon atom.

As it was found that the spins can be dealt with separately, the Hamiltonian matrix \mathbf{H} described by the mean field Hamiltonian (2.18) is of the order N , where N is the number of atoms in the unit cell. We choose the overlap matrix $\mathbf{S} = \mathbf{I}$, and thus overlap of the π orbitals is neglected. The matrix elements are found from equations (2.11) and (2.9). For the π orbitals the Hamilton matrix elements in equation (2.9) depend only on the distance between the atoms. The values of the interaction is determined by either fitting to experimental results or by calculation [38].

The values of \mathbf{k} in the matrix elements are discretized in the irreducible Brillouin zone (IRBZ) For 1D and 2D systems. The number of independent \mathbf{H} that can be constructed is then $2N_{\mathbf{k}}$, where $N_{\mathbf{k}}$ is the number of \mathbf{k} points included in the discretization. In this work we consider 2 dimen-

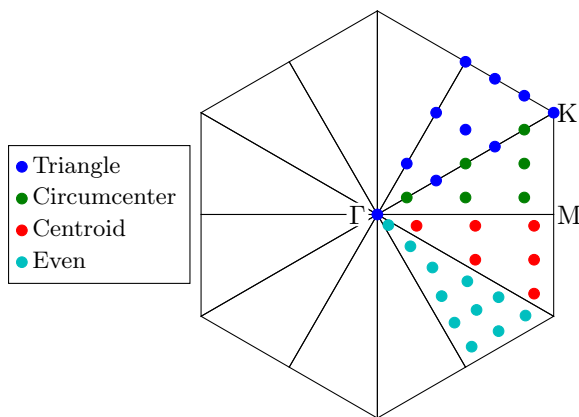


Figure 2.2: *First Brillouin zone and 12 times degenerate IRBZ of hexagonal lattice. The high symmetry points Γ , K and M are shown. The dots represent different choices for discretization of \mathbf{k} .*

sional hexagonal lattices with hexagonal Brillouin zones. The irreducible Brillouin zone is 12 times degenerate within the first Brillouin zone. 4 types of discretization were considered in this work shown in figure 2.2, and the properties of the structures examined were invariant with respect to choice of \mathbf{k} point sampling for sufficiently high $N_{\mathbf{k}}$. For 1D structures the results were sampled with at least $N_{\mathbf{k}} = 512$, and for the 2D structures the results were sampled at $N_{\mathbf{k}} \geq 45$ with the triangle sampling shown in figure 2.2. For the numerical integration the degeneracy of the \mathbf{k} point in the first Brillouin zone was considered by multiplying with the degeneracy.

We are now ready to discuss the iteration scheme for obtaining self-consistent electron densities. The implementation was conducted in the programming language Fortran 2008. This choice was made primarily because of the availability of optimized libraries and compilers from Intel[39] for solving eigenvalue equations. Furthermore, with the introduction of Fortran 2003 object oriented features are a part of the Fortran standard allowing a higher level of abstraction in the code. The final program consists of ~ 5000 lines of code. Here, we limit the discussion to the most important features.

The iteration routine is outlined in figure 2.3. We start with an input electron density \mathbf{n}_{in} . \mathbf{H} is determined from the Hamiltonian (2.18). The eigenvalue problem is solved, and an output electron density \mathbf{n}_{out} is deter-

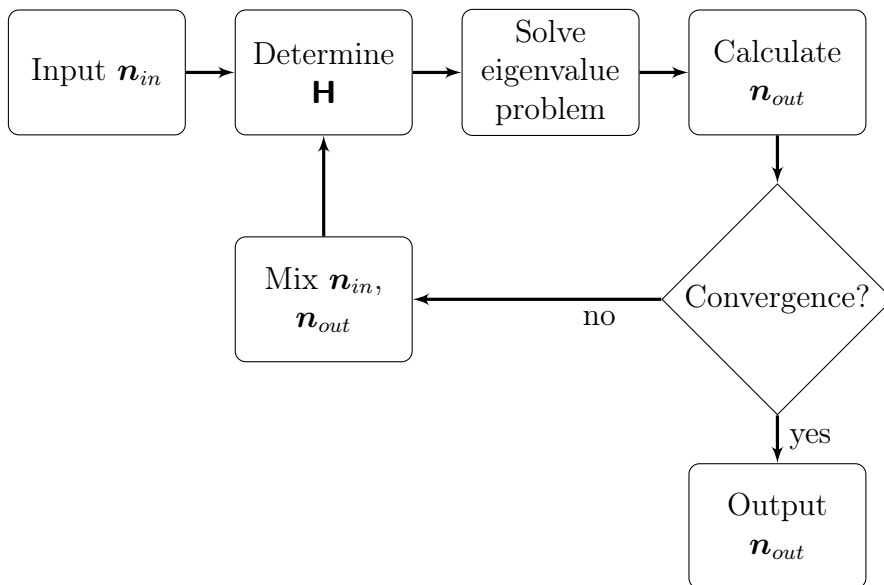


Figure 2.3: Flow chart of routine for determining the electron density self-consistently.

2. METHODS

mined. If the convergence check is fulfilled the routine is done, outputting \mathbf{n}_{out} . Otherwise, a new input density is determined as a mix of \mathbf{n}_{in} and \mathbf{n}_{out} and the routine continues until the convergence criterion is fulfilled.

As input density we choose either an antiferromagnetic or ferromagnetic density where the edges are polarized. The electron density is normalized to the correct number of electrons. It is found that for a paramagnetic start density the routine does not converge. Thus it is required that the input density breaks spin symmetry.

The most computationally demanding part of the routine is solving the eigenvalue problem, and thus the limiting factor for how many atoms can be included in the unit cell. The routine `HEEVR` from `Intel Math Kernel Library LAPACK95` [40] was used for obtaining the eigenvalues and eigenvectors of \mathbf{H} . For 1D or 2D systems the number of independent Hamilton matrices is $2N_{\mathbf{k}}$. Eigenvalues of these matrices can be found in parallel, and thus a parallelization scheme was made using the `openMP` API [41]. This approach decreased the calculation time by a factor equal to the number of threads available for solving the problem.

The output electron density is determined from the eigenvalues and eigenvectors. First, the Fermi energy E_F is found. This is done by requiring the total electron number to be $N(1 + d)$, where d is the doping per unit cell which introduces Nd charges. In this work we limit the discussion to n-type doping by e.g. nitrogen. The Fermi energy is then found by solving for E_F

$$N(1 + d) = N_{\mathbf{k}}^{-1} \sum_{j,\sigma} f_{FD}(\epsilon_{j,\sigma}, E_F, T),$$

where T is the temperature. The equation is solved using a binary search algorithm. The electron density is then found using equation (2.19).

The convergence test of the algorithm ensures that the output density is equal to the input density (2.20). For numerical stability we require

$$\max(|\mathbf{n}_{in} - \mathbf{n}_{out}|) < 10^{-6}$$

for both spins. For most systems solved using the routine the number of iterations required are 10-20.

If the electron density did not converge, the electron densities \mathbf{n}_{in} and \mathbf{n}_{out} are mixed for supplying a new guess for determining the new \mathbf{H} . For finding the ground state, no mixing was required for convergence. When including temperature, doping or starting from a ferromagnetic density simple mixing was applied using

$$\mathbf{n}_{in}^{(i+1)} = \alpha \mathbf{n}_{out}^{(i)} + (1 - \alpha) \mathbf{n}_{in}^{(i)},$$

where the superscript i is the iteration number and α is a constant determining how much of \mathbf{n}_{out} is included in the new input density. For the cases where simple mixing was used α was chosen as 0.5. Thus mixing dampens the charge redistribution between iterations [42]. For antiferromagnetic states in nanostructured graphene, electrons localize on one of the sublattices depending on their spin, e.g. spin up electrons on sublattice A and spin down electrons on sublattice B. As the electron-electron repulsion of the mean field Hamiltonian (2.18) only interact with onsite electrons of opposite spin only the minority spin electrons are repelled from the sublattice, resulting in the antiferromagnetic states.

2.2.1 Density of states

The density of states of a 2D system with discretized \mathbf{k} is

$$D(E) = \frac{1}{A} \sum_{i,\mathbf{k},\sigma} \delta(\epsilon_{i,\mathbf{k},\sigma} - E),$$

where A is the area, $\epsilon_{i,\mathbf{k},\sigma}$ is the eigenvalue with band index i , \mathbf{k} point \mathbf{k} and spin σ . In order to include a finite broadening $\hbar\Gamma$ the function can be convoluted with e.g. a Gaussian lineshape

$$g(E, E_0) = \frac{2}{\hbar\Gamma} \sqrt{\frac{\ln 2}{\pi}} \exp\left(\ln 2 \left[-2 \frac{(E - E_0)}{\hbar\Gamma}\right]^2\right),$$

here shown in the full width half maximum (FWHM) form. For systems with a sufficiently high sampling of \mathbf{k} points the density of states can then be found. However, as the calculation time scales linearly with the number of \mathbf{k} points it is of interest to approximate $D(E)$. In this work we use the improved triangle method for 2D systems presented by Pedersen *et al.* [43]. The method can be used to evaluate integrals of the form

$$S(E) = \int F(\mathbf{k}) \delta(\epsilon_{i,\sigma}(\mathbf{k}) - E) d^2k,$$

and is thus a useful method for evaluating properties involving the density of states.

The projected density of states $P_n(E)$ is the density of states projected on an orbital φ_n . It is found using the equation

$$P_n(E) = \frac{1}{A} \sum_{i,\mathbf{k},\sigma} \delta(\epsilon_{i,\mathbf{k},\sigma} - E) \langle \psi_{i,\mathbf{k},\sigma} | \varphi_n \rangle \langle \varphi_n | \psi_{i,\mathbf{k},\sigma} \rangle,$$

2. METHODS

which for φ_n being a member of the orthonormalized set of orbitals spanning $\psi_{i,\mathbf{k}}$ reduces the bra-ket's to $|c_{n,i,\mathbf{k},\sigma}|^2$.

We address the optical response of the structures by means of linear perturbation theory. The optical response is the interaction between the optical electric field \mathcal{E} oscillating at frequency ω and the current density \mathcal{J} , which for local, isotropic media is given by

$$\mathcal{J}(\omega) = \sigma(\omega)\mathcal{E}(\omega),$$

where σ is the conductivity of the material. The conductivity can be separated in the intraband and the interband conductivity $\sigma = \sigma_{intra} + \sigma_{inter}$. In this work we will deal with interband transitions. In linear response theory the interband conductivity is

$$\text{Re}\{\sigma_{inter}(\omega)\} = \frac{e^2}{2\pi m_0^2 \omega} \sum_{n,m} f_{nm} |\langle \psi_m | \hat{\mathbf{p}} | \psi_n \rangle|^2 \delta(E_{mn} - \hbar\omega), \quad (2.23)$$

where m_0 is the electron mass, $f_{nm} = f_{FD}(E_n) - f_{FD}(E_m)$. Assuming the electron wavefunctions ψ are spanned by a set of orthogonal basis functions φ_i the momentum matrix element is

$$\langle \psi_m | \hat{\mathbf{p}} | \psi_n \rangle = \sum_{i,j} c_{m,j}^* c_{n,i} \langle \varphi_j | \hat{\mathbf{p}} | \varphi_i \rangle.$$

It can be shown that

$$\langle \varphi_j | \hat{\mathbf{p}} | \varphi_i \rangle = \frac{im_0}{\hbar} \langle \varphi_j | [\hat{H}_0, \mathbf{r}] | \varphi_i \rangle.$$

Thus, the matrix elements of the momentum operator are

$$\langle \psi_m | \hat{\mathbf{p}} | \psi_n \rangle = \frac{im_0}{\hbar} \sum_{i,j} c_{m,j}^* c_{n,i} (\mathbf{r}_i - \mathbf{r}_j) \langle \varphi_j | \hat{H}_0 | \varphi_i \rangle$$

in an orthogonal basis with negligible intra-atomic contributions to the momentum matrix elements as shown by Pedersen *et al.* [44]. The matrix elements of the unperturbed Hamilton operator can be evaluated using (2.11).

For systems at $T = 0$ K (or systems with a significant band gap) the values of f_{nm} becomes zero for both $n, m \in c$ or $n, m \in v$ where c is the index for conduction states and v is the index for valence states. We thus only need to consider valence - conduction band transitions, and can restrict n to c and m to v by multiplying by 2.

For spin degenerate systems it is sufficient to consider only 1 of the spins and multiply by the degeneracy as the Hamiltonian commutes with the spin operator. For other systems the full set of eigenvalues and eigenvectors must be considered.

For crystal structures the basis set consists of the Bloch sums from equation (2.8). Thus the quantum number n corresponds to a band number and a \mathbf{k} point. We neglect Umklapp scattering and thus only direct transitions where \mathbf{k} is unchanged are considered. The matrix element is then

$$\langle \psi_{m_0, \mathbf{k}} | \hat{\mathbf{p}} | \psi_{n, \mathbf{k}} \rangle = \frac{im}{\hbar} \sum_{i,j} c_{m,j,\mathbf{k}}^* c_{n,i,\mathbf{k}} (\mathbf{r}_i - \mathbf{r}_j) \langle \varphi_{j,\mathbf{k}} | \hat{H}_0 | \varphi_{i,\mathbf{k}} \rangle.$$

By choosing the phase of the Bloch sums as in equation (2.11) the equation becomes

$$\begin{aligned} \langle \psi_{m,\mathbf{k}} | \hat{\mathbf{p}} | \psi_{n,\mathbf{k}} \rangle &= \frac{im_0}{\hbar} \sum_{i,j} c_{m,j,\mathbf{k}}^* c_{n,i,\mathbf{k}} \Delta \mathbf{R}_{i,j} e^{i\mathbf{k} \cdot \Delta \mathbf{R}_{i,j}} H_{i,j} \\ &= \frac{im_0}{\hbar} \sum_{i,j} c_{m,j,\mathbf{k}}^* c_{n,i,\mathbf{k}} \nabla_{\mathbf{k}} H_{i,j}(\mathbf{k}). \end{aligned} \quad (2.24)$$

The optical conductivity can now be evaluated using the matrix elements (2.24) in (2.23). The equation can be solved using the improved triangle method by Pedersen *et al.* [43].

[45]

Chapter 3

Results and discussion

The results of modeling graphene systems of 0, 1 and 2 periodic dimensions in the Hubbard model are presented. We start by examining the spin polarization and band gap dependence of the shape and dimensions of the system. 1 dimensional structures are presented and compared to other models. 0 dimensional structures are examined for explaining why the systems are spin polarized. The results for 2 dimensional systems are presented. Ferromagnetic states are examined and the stability of spin polarized states are examined with respect to temperature and doping. Finally we consider optical response and how the Hubbard model changes the properties.

The calculations using the Hubbard model are conducted using the mean field Hamiltonian (2.18). Tight binding calculations are performed using third nearest neighbours (3NN) and orthogonal basis sets. The systems are iterated using the iteration routine presented in section 2.2.

The parameters of the Hubbard model are chosen as $U = 2.0$ eV and $t_1 = -2.7$ eV for nearest neighbours, $t_2 = -0.2$ eV for next nearest neighbours and $t_3 = -0.18$ eV for third nearest neighbours [46]. Unless otherwise specified the systems are at half filling (1 electron per atom) and modeled at an electron temperature of 0 K.

3.1 Ribbons

Graphene nanoribbons are a class of nanostructured graphene with an infinitely periodic dimension and two edges. The two simplest types, the zigzag nanoribbon (ZGNR) and the armchair nanoribbon (AGNR) will be examined here. The unit cell of either type is characterized by a single parameter, the number of carbon dimers in the unit cell N . We denote zigzag

3. RESULTS AND DISCUSSION

nanoribbons N -ZGNR and armchair nanoribbons N -AGNR. The width of the nanoribbon is $w = Na/2$ for armchair nanoribbons and $w = Na\sqrt{3}/2$ for zigzag nanoribbons, where $a = 2.461 \text{ \AA}$ is the graphene lattice constant.

In this work the main goal is to examine the band gap of nanostructured graphene, and thus the applied model must predict the bands accurately close to the band gap. *Ab initio* calculations of the band structure by Son *et al.* [9] showed that a nearest neighbour tight binding model is insufficient for determining the band gap of armchair and zigzag nanoribbons. The tight binding model only found a band gap for 2/3 of the armchair ribbons, while in the *ab initio* calculations all ribbons displayed a band gap. To improve the tight binding model we include interactions up to third nearest neighbours and include the Hubbard interaction. The parameter set chosen was optimized by Hancock *et al.* [46] for fitting the band structures of ZGNRs and AGNRs.

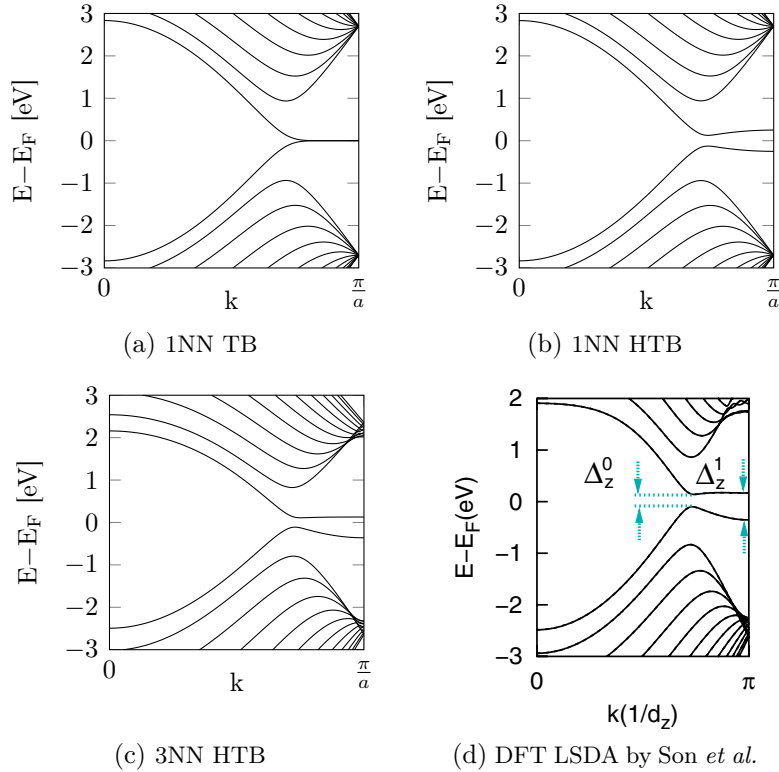


Figure 3.1: Bandstructure of a zigzag nanoribbon with $N = 12$. (a) is determined using the 1NN tight binding model, (b) is determined using the 1NN Hubbard model, (c) is determined using the 3NN Hubbard model and (d) is determined from *ab initio* calculations by Son *et al.* [9].

A comparison of band structures for a 12-ZGNR is presented in figure 3.1. Starting from a 1NN tight binding model, it is found that inclusion of the Hubbard term introduces a band gap of 0.254 eV. Introduction of third nearest neighbour interactions reduces the direct band gap to 0.228 eV, breaks the electron-hole symmetry and improves the agreement with *ab initio* calculations.

Band structures of AGNRs determined using the 3NN Hubbard model are presented in figure 3.2 and compared to DFT calculations by Son *et al.* [9]. In the low energy range the band structures are found to be in agreement and the band gap is nonzero for all types of AGNR. In the AGNR structures no spin polarization is found, and thus the Hubbard contribution to the band gap is zero.

Using the 3NN Hubbard model, the band gap is calculated as a function of width of the zigzag/armchair nanoribbon and presented in figure 3.3. It is found that the band gap decreases for increasing width for all nanoribbons. The armchair ribbons split in 3 groups depending on their size parameter with the band gap following $E_{3p} > E_{3p+1} > E_{3p+2}$, where p is an integer. Comparing to DFT LSDA calculations by Son *et al.* [9] the band gaps are

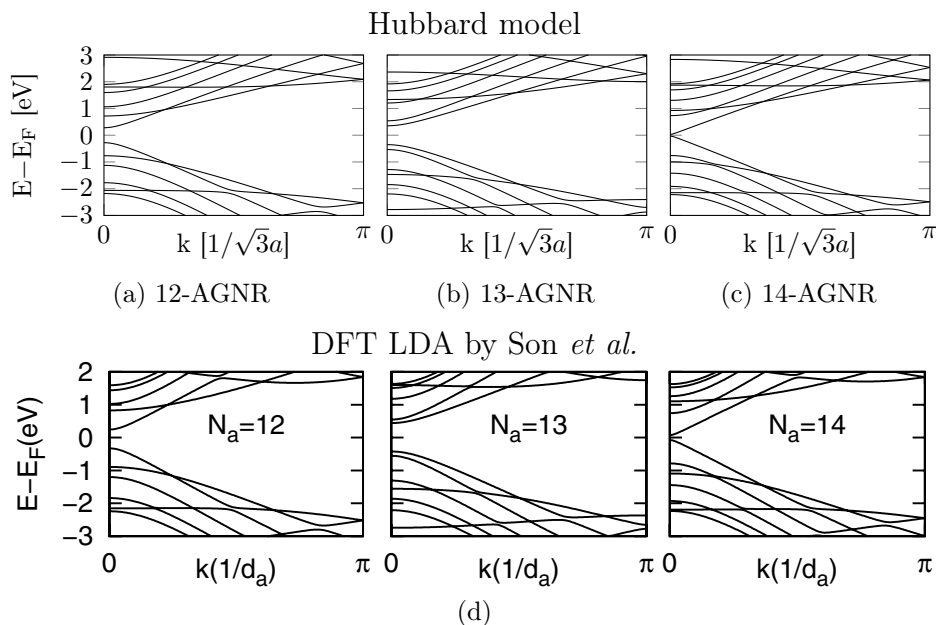


Figure 3.2: (a), (b) and (c): Armchair bandstructures for $N = 12, 13$ and 14 , respectively, determined using the 3NN Hubbard model. (d): Armchair bandstructures for $N = 12, 13$ and 14 from *ab initio* calculations by Son *et al.* [9].

3. RESULTS AND DISCUSSION

found to be lower for the $3p$ and $3p+2$ groups. This is caused by inclusion of structure relaxation in the DFT calculations. According to Son *et al.* [9] the bond length between edge atoms decreases by $\sim 3.5\%$, and as found by Hancock *et al.* [46] modifying the t_1 edge parameter to $1.06t_1$ will improve the agreement between the models. Considering 2D structure relaxation the C-C bond lengths are found in the range $[0.96; 1.02]a_0$, where a_0 is the C-C bond length for pristine graphene [47, 48]. This increases the band gap by up to 15% [47].

In the ground state of armchair nanoribbons the total and local magnetic moments are zero. For zigzag nanoribbons a local magnetic moment is found at the edges which decays further into the bulk as shown in figure 3.4. The orientation of the magnetic moments at the opposing edges is

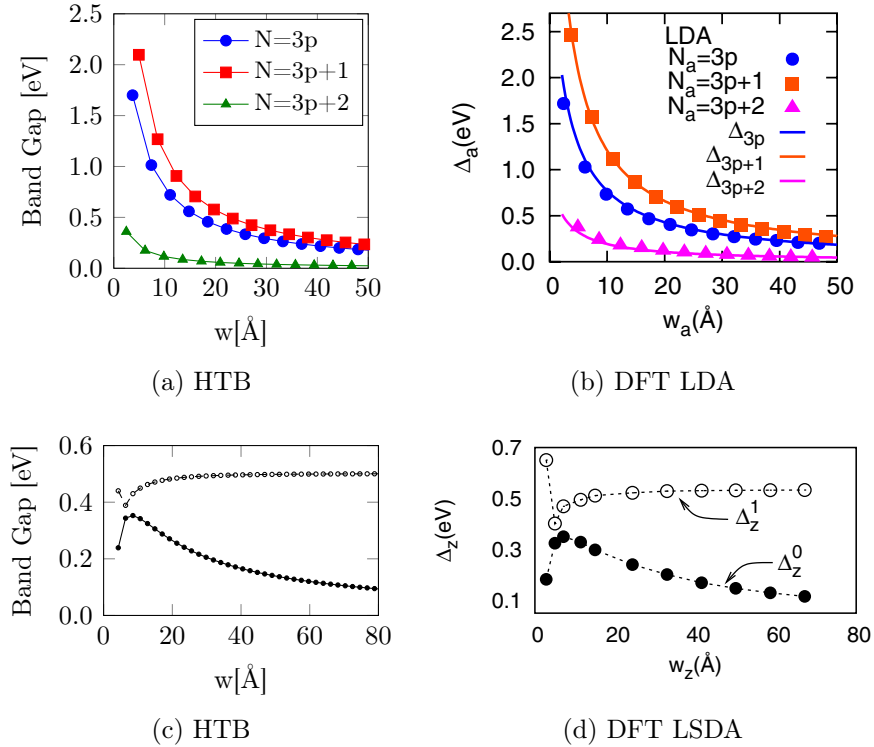


Figure 3.3: Band gap as a function of width of nanoribbon. (a) and (c) are determined using the 3NN Hubbard model while (b) and (d) are determined from *ab initio* calculations by Son *et al.* [9]. (a) and (b) are for armchair nanoribbons while (c) and (d) are for zigzag nanoribbons. In (c) and (d) the band gap is shown as the solid line (---), while the dashed line (- - -) is the gap at $k = \frac{\pi}{a}$.

antiparallel with a total magnetic moment of zero. The orientation of the magnetic moments alternate with the sublattice, and thus the ground state is antiferromagnetic.

In figure 3.4 the spin density obtained using the Hubbard model and illustrated using Slater-type orbitals is compared to the spin density obtained by Son *et al.* [9]. The results are in agreement with the largest differences appearing at the edge caused by structure relaxation and terminating hydrogen atoms included in the *ab initio* model. By relaxing the structure the edge atom bond lengths decrease by $\sim 2\%$, which can be modeled by using $t_{edge} = 1.03t_1$ for the t_1 parameter for edge atoms [46, 48]. It was shown by Fürst *et al.* [23] that dangling σ bonds lift the spin degeneracy and change the band structure near the Fermi level. Thus in the Hubbard model it is assumed dangling σ bonds are passivated by hydrogen.

The local spin polarization defined by equation (2.22) as a function of ribbon width is plotted in figure 3.5. Summing the spin density of half of the ribbon the total polarization converges towards $\frac{1}{3}$ unpaired electrons. The spin polarization of the edge atom stabilizes for smaller N at ≈ 0.25 unpaired electrons.

The contributions to the electron density of the bands are shown in figure 3.6 for a 12-ZGNR. It is found that the contributions to the electron density of bands 1-11 are approximately equal for all atoms. Band 12 is

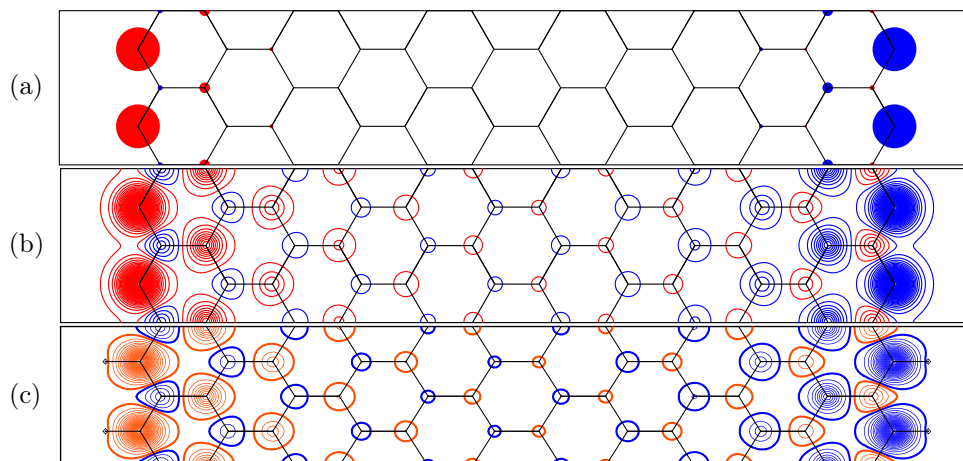


Figure 3.4: *Spin density plot of a 12-ZGNR. (a) is determined using the 3NN Hubbard model and shows the local spin density as the radius of the circles. Red is spin up and blue is spin down. In figure (b) the weights shown in (a) are applied to Slater-type orbitals for illustrating the spin density and comparing to *ab initio* results of Son *et al.* [9] in (c).*

3. RESULTS AND DISCUSSION

the highest occupied band and is found to contribute the most to the spin density at the edges. The states of band 12 are found to be a mix of bulk states and edge states which decrease exponentially with distance from the edge atom.

The projected density of states on the left edge atom shown in figure 3.7 shows that the states with energy within 0.5 eV of the Fermi level are the edge states. Spin up states are located below the Fermi level in band 12 while spin down states are located above the Fermi level in band 13. Examining the edge projection of states in band 12 it is found that for $k < \frac{2\pi}{3a}$ the states are bulk states, while for $k > \frac{2\pi}{3a}$ the localization of the states on the edge atom increases until $k = \frac{\pi}{a}$, where the states are located only on the edge atom. By symmetry and reversal of spins, all arguments are valid for the other edge.

We now examine the metastable ferromagnetic state presented in figure 3.8a. The state is obtained by preparing the system in a ferromagnetic state and iterating until a self-consistent electron density is obtained. The spin symmetry of the band structure is broken and the resulting system is metallic with spin up and spin down bands crossing the fermi level as shown in figure 3.8b. For increasing ribbon width, this crossover point approaches $k = \frac{2\pi}{3a}$. Thus the total magnetic moment approaches $2/3\mu_B$ as shown in figure 3.8c per unit cell, corresponding to 1/3 unpaired electrons per edge.

The difference between the ferromagnetic and antiferromagnetic states is a spin flip of either edge, and thus the magnetic interaction between the edges can be examined by determining the energy difference between the states. This is shown in figure 3.8d calculated using the 3NN Hubbard model. The calculated energy difference is smaller than the energy difference calculated by Pisani *et al.* [49] shown in figure 3.8e using DFT LSDA and GGA-PBE, but the results are of the same magnitude and less than 10 meV. However, using the B3LYP functional, Pisani *et al.* [49] report $\Delta E \approx 25$ meV for $N \sim 8$ allowing room temperature magnetic ordering.

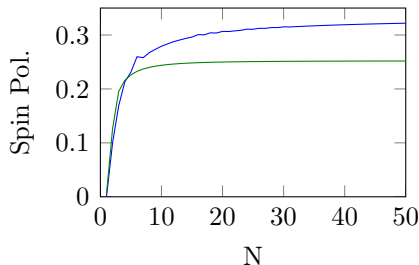


Figure 3.5: Spin polarization of half of ribbon (—) and edge atom (—).

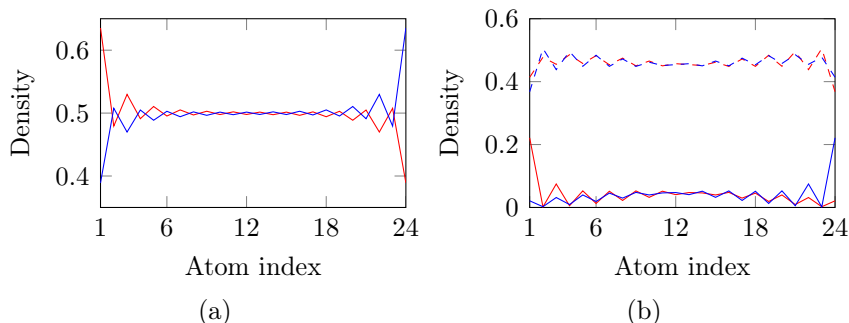


Figure 3.6: (a) Electron density of spin up (—) and spin down (—) electrons for a 12-ZGNR. The atom index is the atoms of the unit cell numbered from one edge to the other. (b) Contribution to the electron density of bands 1-11 (\uparrow - - -, \downarrow - - -) and band 12 (\uparrow —, \downarrow —).

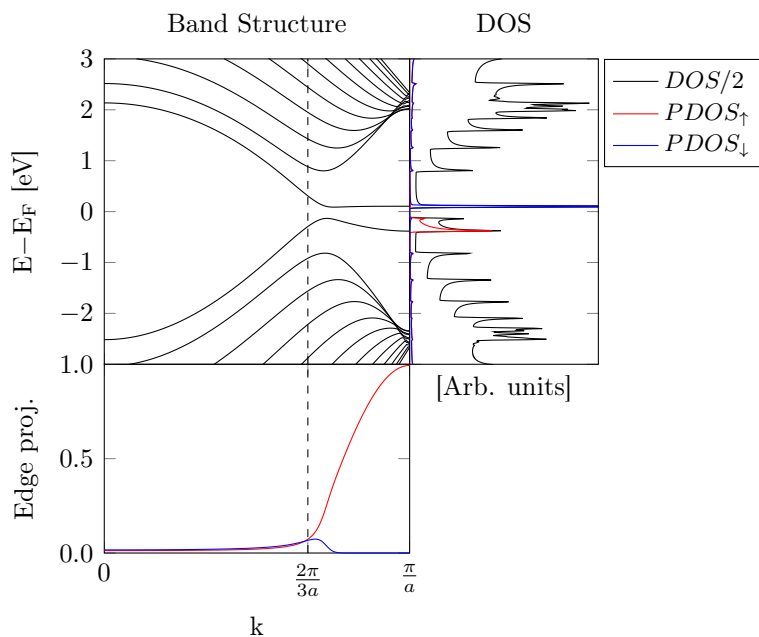


Figure 3.7: All figures are for a 12-ZGNR. The edge atom in the plots is the left edge atom in the unit cell (figure 3.4). Top left: Band structure. Top right: Density of states (—), projected density of states on the edge atom for spin up (—) and spin down (—). Bottom left: Projection of eigenstates in the highest occupied band (band 12) on the edge atom. Determined using $\langle \psi_{12,k,\sigma} | \varphi_{edge} \rangle$, where the first index is the band number, second index the k value, third index the spin and φ_{edge} is the π orbital of the edge atom. — is spin up and — spin down.

3. RESULTS AND DISCUSSION

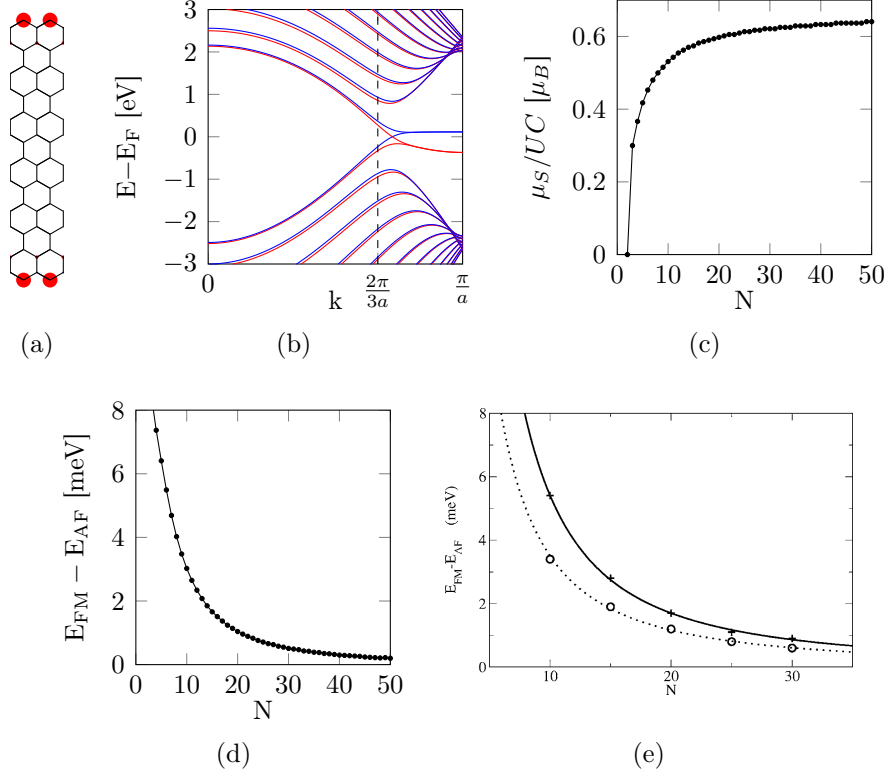


Figure 3.8: *Metastable ferromagnetic state of zigzag nanoribbons. (a) Spin density plot of a 12-ZGNR in the ferromagnetic state. (b) Band structure of the 12-ZGNR with red being spin up bands and blue being spin down bands. (c) Total magnetic moment per unit cell as a function of nanoribbon width. (d) Difference in total energy per unit cell between ferromagnetic and antiferromagnetic states as a function of ribbon width determined using the 3NN Hubbard model in equation (2.21). (e) Energy difference between ferromagnetic and antiferromagnetic states as a function of ribbon width determined using DFT LSDA (circle) and GGA-PBE (plus) by Pisani et al. [49].*

3.2 Nanoflakes

Different geometries of 0-dimensional graphene flakes are examined in the Hubbard model to determine spin properties of the systems. As larger 1- or 2- dimensional systems in some cases can be considered to consist of arrays of these flakes some properties might be predicted by examining 0-dimensional structures. Because of their simplicity the 0D structures are examined to explain the origin of spin polarization.

We first examine triangular graphene flakes of the type presented in figure 3.9a. The ground state is found to be ferromagnetic (FM) in the Hubbard model. The total spin of the ground state increases linearly with the size as shown in figure 3.9d, and is proportional to the sublattice imbalance $N_A - N_B$ as predicted by Lieb's theorem. This spin polarization causes the introduction of an energy gap between the highest occupied molecular orbital and lowest unoccupied molecular orbital states (from now on denoted the band gap) compared to the approximately zero band gap found in tight binding calculations as shown in figure 3.9c. The band gap is found to decrease with the size of the flake.

Combining two triangular flakes a bowtie geometry can be made as presented in figure 3.9b. The state presented in figure 3.9b is the ground state, and has total spin $S_z = 0$. This is in accordance with Lieb's theorem, as the sublattices are balanced. However, two domains with opposing spin polarization are found. This is predicted by graph theory for hexagonal graphs, which predicts the number of zero energy states as the nullity η of the graph [50]. The nullity of the structure is $\eta = 2\alpha - N$, where α is the maximum number of non-adjacent atoms and N is the total number of atoms. The nullity of the structure in figure 3.9b is 2. According to the Stoner criterion, the system becomes magnetic when the exchange energy gain is larger than the kinetic energy penalty for spin polarizing the system. The kinetic energy penalty is proportional to the energy of the state and the exchange energy gain is proportional to U , and thus the zero energy states become spin polarized. [51]

The size of the bowtie flake is given by two parameters, size S corresponding to the triangle size and width W corresponding to the number of atoms joining the triangle-like domains. The ground state is found to be antiferromagnetic (AFM). A plot of the band gap and spin for increasing size is presented in figure 3.9e and for increasing width in figure 3.9f. It is found that the band gap decreases for increasing size which agrees with the result for triangular domains. It is found that the band gap of the antiferromagnetic system is independent of the width of the bowtie for $S - W > 1$ or $W > 2$.

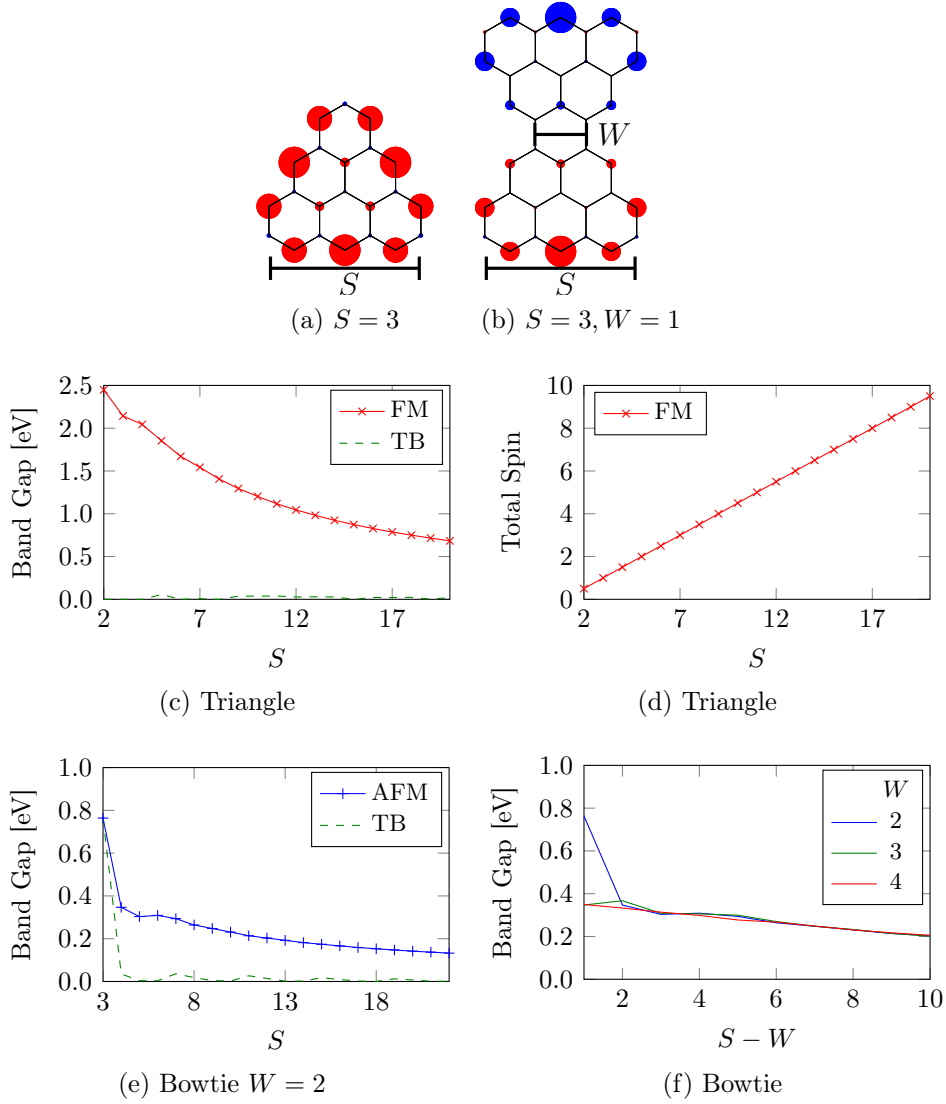


Figure 3.9: Ground state spin density of triangle (a) and bowtie (b) graphene flakes. The spin is shown as red (spin up) and blue (spin down) circles where the radius is the magnitude of the spin density. The band gap is shown in (c) and total spin in (d) for increasing size of triangle flakes. The band gap for increasing size of bowtie flakes is shown in (e) and increasing width of bowtie flakes in (f). The band gap is shown for antiferromagnetic states and for tight binding calculations.

3. RESULTS AND DISCUSSION

We now examine square graphene flakes of the type presented in figure 3.10a. The graphene flakes are characterized by the size S , which is the number of hexagons along the zigzag direction, and the width W , which is the number of dimer atom pairs along the armchair direction. The ground state in figure 3.10a is spin polarized at the zigzag edge, while the armchair edge is only spin polarized at the boundary to the zigzag edge. The ferromagnetic state presented in figure 3.10b is a local minimum obtained by starting from a ferromagnetic density and iterating. The electron density is similar to the antiferromagnetic state with local deviations under 1% to the densities of the antiferromagnetic state 3.10a with the spin down and spin up densities have been flipped above the middle. The ferromagnetic state can be excited by a magnetic field, and has total spin equal to the sum of the magnitude of the spins of the spin up and down domains in figure 3.10a.

For increasing size the band gap is presented in figure 3.10c and total spin in figure 3.10d. For $S < 4$ no spin polarization is found, and the band gap consists only of the tight binding contribution. For $S \geq 4$ the system is spin polarized. The band gap of the antiferromagnetic state is approximately constant, while the band gap of the ferromagnetic state decreases with the size and increases with the total spin of the state. We expect that for $S \rightarrow \infty$ the band gap for ferromagnetic states closes in agreement with the results for ZGNRs. The total spin is seen to change when S increases by ≈ 5 . For the 6-ZGNR case, it is found that the number of spin polarized electrons per edge is ≈ 0.25 from figure 3.5. This is consistent with the spin increasing by 1 for S increasing by 4, which we thus expect for larger sizes when the effects of the edge diminishes.

The band gap of the ground state is presented in figure 3.10e for increasing width. For small sizes < 7 it is seen that the band gap of the examined structures is in one of two groups, even width and odd width. This behavior is caused by the choice of unit cells. For even width the total system is antiferromagnetic, while for odd width the sublattices are unbalanced resulting in a total spin of 0.5. The band gap is dominated by this behavior for small S , while for large S the band gap is found to decrease for increasing width consistent with results for ZGNRs. We note that the tight binding band gap of odd width square flakes is 0, as a spin degenerate zero energy state is found at the Fermi energy.

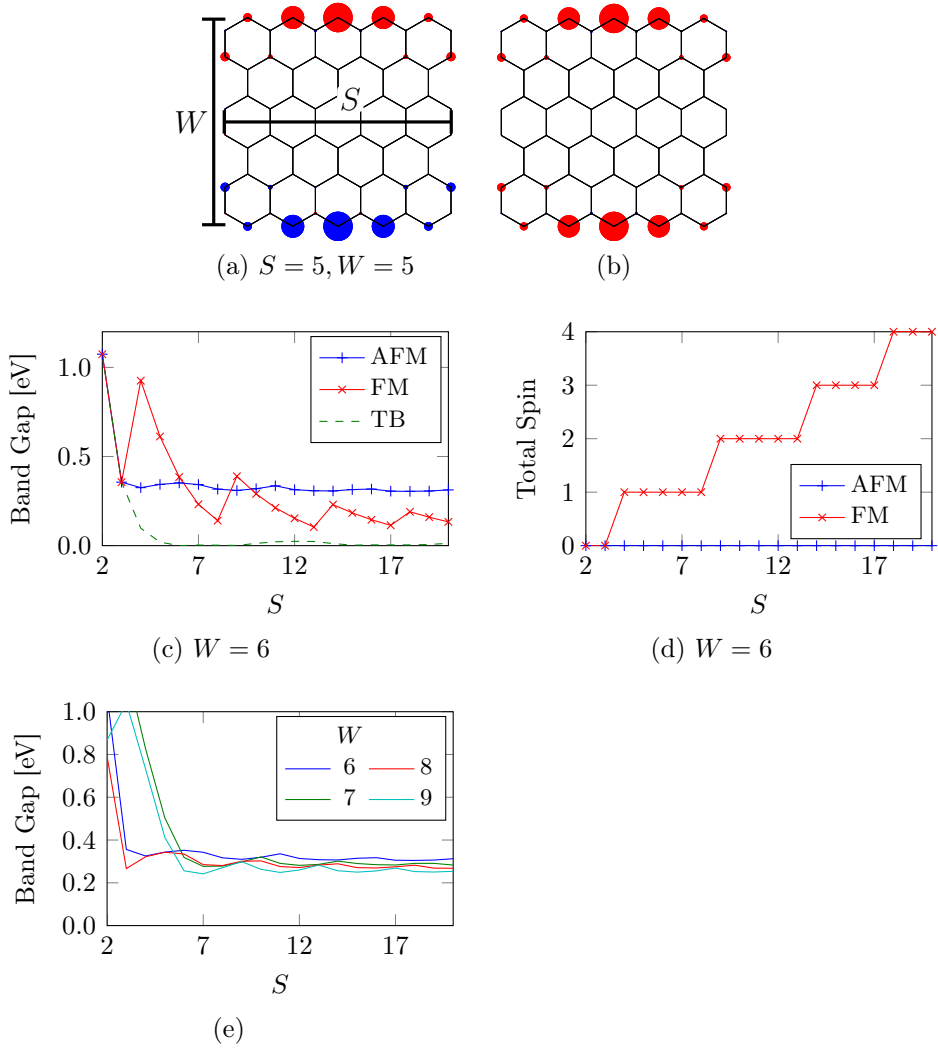


Figure 3.10: (a) Ground state spin density of square graphene flakes. The spin is shown as red (spin up) and blue (spin down) circles where the radius is the magnitude of the spin density. (b) is a ferromagnetic state. The band gap is shown in (c) and total spin in (d) for increasing size of square flakes for antiferromagnetic states, ferromagnetic states and for tight binding calculations. (e) Comparison of band gap for the ground state of square graphene flakes with varying widths.

3. RESULTS AND DISCUSSION

We now consider rhombic and hexagonal flakes. The size S of rhombic flakes as presented in figure 3.11a and hexagonal flakes as presented in figure 3.11c is controlled by a single parameter, the number of hexagons along an edge. It is found that below a critical size the system is unpolarized. The critical size is 4 for rhombs, 9 for antiferromagnetic hexagons and 10 for ferromagnetic hexagons as can be seen in figures 3.11d and 3.11f. Below these values the band gaps consist only of the tight binding contribution, while for higher values the antiferromagnetic band gap is found to be higher than the ferromagnetic band gap. Furthermore it can be seen that the maximum local spin polarization stabilizes at a constant value for both the antiferromagnetic and ferromagnetic systems.

For all examined zigzag structures with balanced numbers of A and B atoms over a certain size, the antiferromagnetic state is the ground state. The edges are spin polarized with alternating majority spin at the A and B edges. For unbalanced lattices there is no minimum size requirements for magnetism.

We define the angle between the edges as the angle between the normal vectors of the edges and denote the place the edges meet as the edge corner. The critical size for onset of spin polarization is found to depend on the angle between the edges. For a zigzag edge corner with an angle of 60° the new edge is a zigzag edge, but with a change of sublattice. This corresponds to a change of spin polarization as shown for bowtie, rhomb and hexagon flakes. In the hexagonal flake, where all edge corners are 60° , the largest critical size of $S = 9$ is found. For zigzag edge corners of 120° the edge belongs to the same sublattice. This was the case for corners in the triangle, bowtie and rhomb flakes. In the triangle structure with only 120° corners no critical size was found, all structures were spin polarized. Finally for edge corners of 90° the corner connects a zigzag edge with an armchair edge. This is the case for square graphene flakes, where the critical size is found to be $S = 4$.

The most important parameter determining the critical size is the choice of Hubbard U . Bhowmick and Shenoy [52] found that for $U = 2t$ the number of repeat units of zigzag edge atoms is 3-4 for onset of spin polarization, while for $U = 1.2t$ the number of repeat units is 5-6. In their work the main focus was zigzag-armchair corners of 30° . In this work our choice of Hubbard $U \approx 0.75t_1$ and inclusion of third nearest neighbour interactions result in critical sizes of 4-9 depending on the edge corner angle.

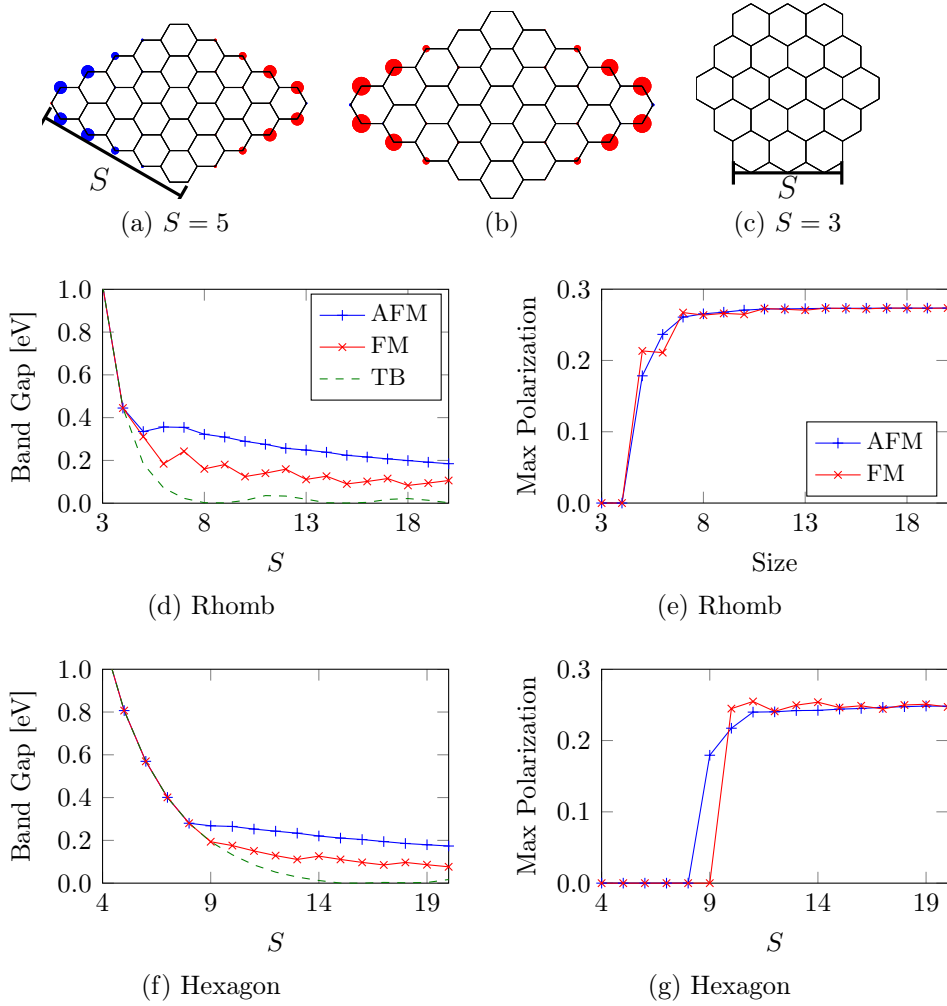


Figure 3.11: Ground state spin density of rhombic (a) and hexagonal (c) graphene flakes. The spin is shown as red (spin up) and blue (spin down) circles where the radius is the magnitude of the spin density. (b) is a ferromagnetic rhombic state. The band gap is shown to the left and maximum local spin polarization determined using equation (2.22) to the right for increasing size of rhombic flakes (d), (e) and hexagonal flakes (f), (g). The band gap is shown for antiferromagnetic states, ferromagnetic states and for tight binding calculations.

3.3 Triangular Antidot Lattices

In this work, we study triangular graphene antidot lattices. As zigzag edges are a requisite for spin polarization, the types of holes studied will be hexagonal holes with zigzag edges, in the following denoted graphene hexagonal antidot lattices (GHALs). The structures studied can be described with a set of parameters L, S and W , where L is the unit cell side length, S is the side length of the antidot hole and W the smallest width separating holes from different unit cells. For the chosen structures 2 of the parameters are sufficient to describe the structures uniquely, so we choose the set $\{W, S\}$ for emphasizing the importance of the actual graphene structure. For converting the parameters to physical dimensions parameters along a zigzag edge are multiplied by $a = 2.461 \text{ \AA}$, the graphene lattice constant, and parameters along an armchair edge are multiplied by $\frac{a\sqrt{3}}{2}$.

We start by examining GHALs with unit cells of the type shown in figure 3.12a. This structure can be described as ZGNRs of width $W = 2(L - S)$ and finite length S joined in a lattice. Thus for large holes spin polarized edges are expected and a band gap approximately equal to those of ZGNRs shown in figure 3.3c. Furthermore, for vanishing holes the structure reduces to intrinsic graphene with no spin polarization and band gap. We thus expect a transition region to exist and seek to identify the size evolution of the properties. Previously, Yu *et al.* [27] showed the existence of an antiferromagnetic ground state for GHALs with sufficiently large unit cells using DFT GGA calculations.

The ground state spin density of the $\{W = 6, S = 8\}$ structure is shown in figure 3.12b. It is seen that the edges of the hole are spin polarized with opposite spin direction for either sublattice resulting in an antiferromagnetic ground state. This is consistent with the ground state results for ZGNRs and hexagonal flakes. The spin density is seen to increase with the distance to the junction. We thus introduce the max spin polarization as a variable for quantifying the spin polarization.

The band gap and maximum spin polarization is shown in figure 3.12c for a variety of $\{W, S\}$ pairs. It is found that for $S < 6$ the structures are paramagnetic, no spin polarization is found. For $S \geq 6$ the structure becomes spin polarized. The maximum spin polarization increases with S for $6 \geq S < 10$ and then stabilizes at a value approximately equal to the ZGNR edge atom polarization.

For $S < 6$ the band gap determined using the Hubbard model is equal to the band gap determined using tight binding. For $S \geq 6$ the tight binding band gap goes to zero while the Hubbard band gap increases with the spin polarization and stabilizes at a value within 0.05 eV of the corresponding

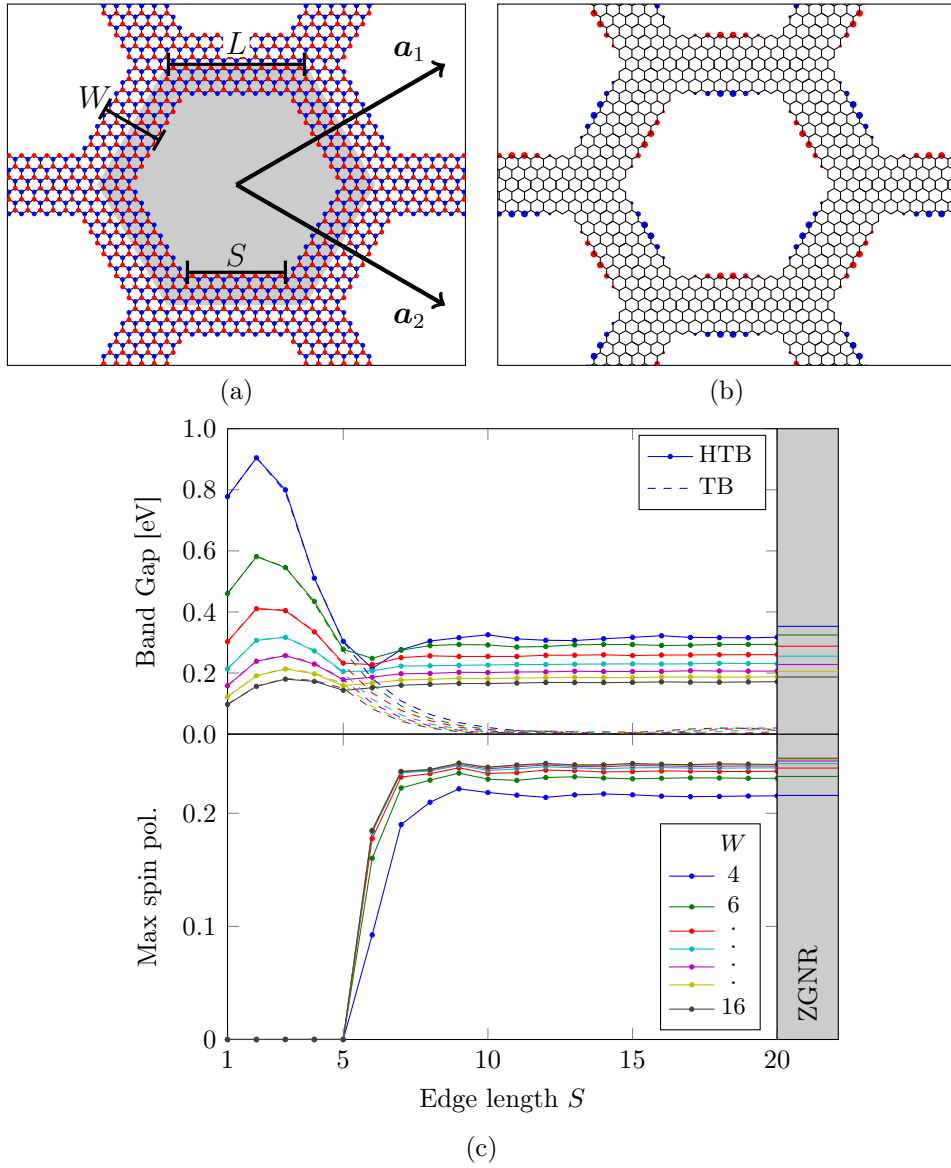


Figure 3.12: *Triangular GHAL with even width.* (a) *Shaded region: Unit cell of $\{W = 6, S = 8\}$ and $L = 11$ GHAL with carbon atoms colored red for sublattice A and blue for sublattice B. \mathbf{a}_1 and \mathbf{a}_2 are the unit cell lattice vectors and the parameters L , S and W are shown.* (b) *Ground state spin density of the structure shown in (a).* (c) *Top: Band gaps of GHALs calculated using the Hubbard (---) and tight binding (---) model. The color shows the width W of the corresponding ZGNR and the band gaps of the ZGNRs are shown in the shaded region. Bottom: Max spin polarization of GHALs for different edge lengths and widths.*

ZGNR value. Thus for large holes the electronic properties are dominated by the ZGNR parts of the structure with the junctions being less significant. The band gap is determined primarily by the width W with a size dependence shown in figure 3.3c.

The spin polarization and band gaps obtained with the Hubbard model are in agreement with DFT LSDA calculations by Trolle *et al.* [53]. Furthermore the DFT calculations agree with a critical size $S = 6$ as the onset for spin polarization.

Examining the edge spin polarization shown in figure 3.13 it is found that the spin polarization increases for the first 4 atoms from the junction and then stabilizes at ≈ 0.24 . Thus for $S \geq 8$ the spin density of the middle edge atoms resembles that of ZGNR edge atoms shown in figure 3.5. The maximum spin polarization shown in figure 3.12c thus quantifies how much the middle of the ZGNR slabs resemble ZGNRs. For larger edge lengths it is seen that the spin polarization fluctuates with 2 maxima for $S = 13$ and 3 for $S = 17$. This is caused by edge states of higher order becoming available.

The band structure and density of states for a $\{4, 8\}$ GHAL is shown in figure 3.14. The bands close to the Fermi energy are found to be approximately dispersionless and in groups of 3. Because of the bands being spin degenerate, a group of bands then corresponds to 1 electron per edge in the unit cell. By examining the projected density of states on the edge atoms it is found that the states closest to the Fermi level are the main contributors to the edge spin polarization, as the degree of localization decreases for lower energy states and the contributions are canceled by approximately equal localization of spin down states.

To the best of our knowledge this is the first systematic study of the band gap behaviour in GHALs with holes large enough for spin polarization to occur. The simple scaling law $E_{gap} \approx \alpha N_{rem}^{1/2} / N_{tot}$, where N_{rem} is the number of atoms removed in the hole, N_{tot} the total number of atoms in the unit cell without the hole and α a fitting parameter, was proposed by Pedersen *et al.* [20] for circular holes. The model was extended to both armchair and zigzag triangular and rhombic holes by Liu *et al.* [25] by setting α from 4 to 25 eV. Both zigzag triangular and rhombic holes are spin polarized. For hexagonal holes with even width Ouyang *et al.* [24] showed that by introduction of an exponential function the scaling law could be applied to spin unpolarized GHALs.

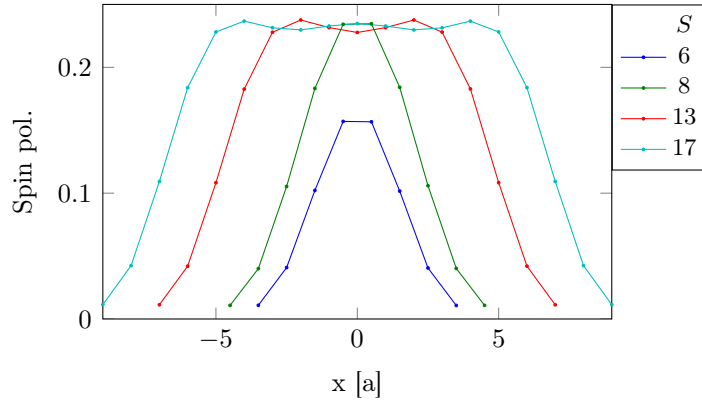


Figure 3.13: Spin polarization of atoms along the S line in figure 3.12a. All atoms except the first and last are edge atoms. The spin polarization is shown for $W = 6$ and $S = 6, 8, 13$ and 17 . The spin polarization is found to increase for the first four edge atoms to a value of ≈ 0.24 and then fluctuate around the value.

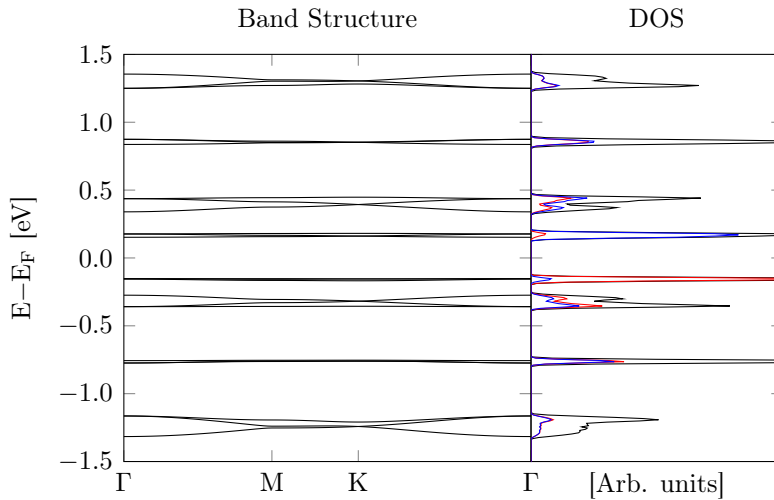


Figure 3.14: Band structure and density of states of $\{4, 8\}$ GHAL. The low energy bands are found in groups of 3 very flat bands. In the density of states plot the projected density of states on sublattice A edge atoms is shown as red lines for spin up and blue lines for spin down. It is found that the states closest to the Fermi level are most localized on the edge atoms with the majority of the spin up states below the Fermi level and the majority of the spin down states above the Fermi level.

3. RESULTS AND DISCUSSION

By considering the area of the hexagonal unit cells the ratio $N_{rem}^{1/2}/N_{tot}$ for GHALs can be shown to be

$$\frac{N_{rem}^{1/2}}{N_{tot}} = \frac{(2A_{hole}/A_{grapheneUC})^{1/2}}{2A_{UC}/A_{grapheneUC}} = \frac{S}{\sqrt{6}(S + W/2)^2},$$

where A is the area of the subscript. Thus for $S \rightarrow \infty$ and constant W $N_{rem}^{1/2}/N_{tot} \rightarrow 0$. However for large S the band gap depends only on W , and thus the simple scaling law cannot be applied to spin polarized GHALs. This is shown in figure 3.15, where it is seen that the scaling law fits for the smallest values of S (1 and 2). For $2 < S < 6$ the modifications by Ouyang *et al.* [24] are needed, but for $S \geq 6$ no scaling with $N_{rem}^{1/2}/N_{tot}$ is found.

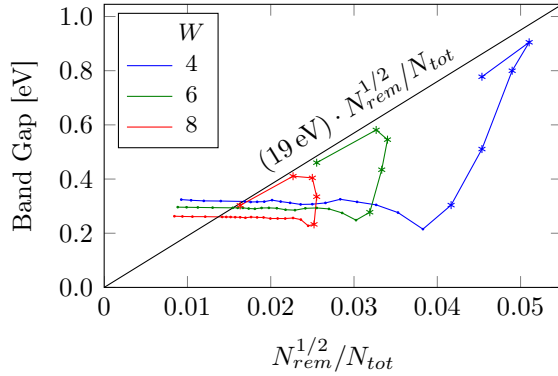


Figure 3.15: Comparison of band gap with the scaling law $E_{gap} \approx \alpha N_{rem}^{1/2}/N_{tot}$ proposed by Pedersen *et al.* [20]. The value $\alpha = 19 \text{ eV}$ was chosen as an adequate fit for the values $S \leq 2$. In the plot, values with $S < 6$ are represented with a star (*) and values with $S \geq 6$ are represented with a dot (·). For $S \geq 6$ the band gap stabilizes and is constant with $N_{rem}^{1/2}/N_{tot}$. The highest value of S shown is $S = 40$.

3.3.1 Other unit cells

The band gap of GHALs with small holes has been shown to depend on the specific unit cells resulting in either semiconducting or metallic behaviour [21, 24, 54]. We thus extend the discussion to unit cells predicted as metallic. First unit cells of the type shown in figure 3.16a are examined, where the width W is uneven. For large holes a spin polarized antiferromagnetic ground state is found as presented in figure 3.16b.

The band gap and maximum spin polarization is presented in figure 3.16c. The emergence of spin polarization is found to be $S = 5$, an edge

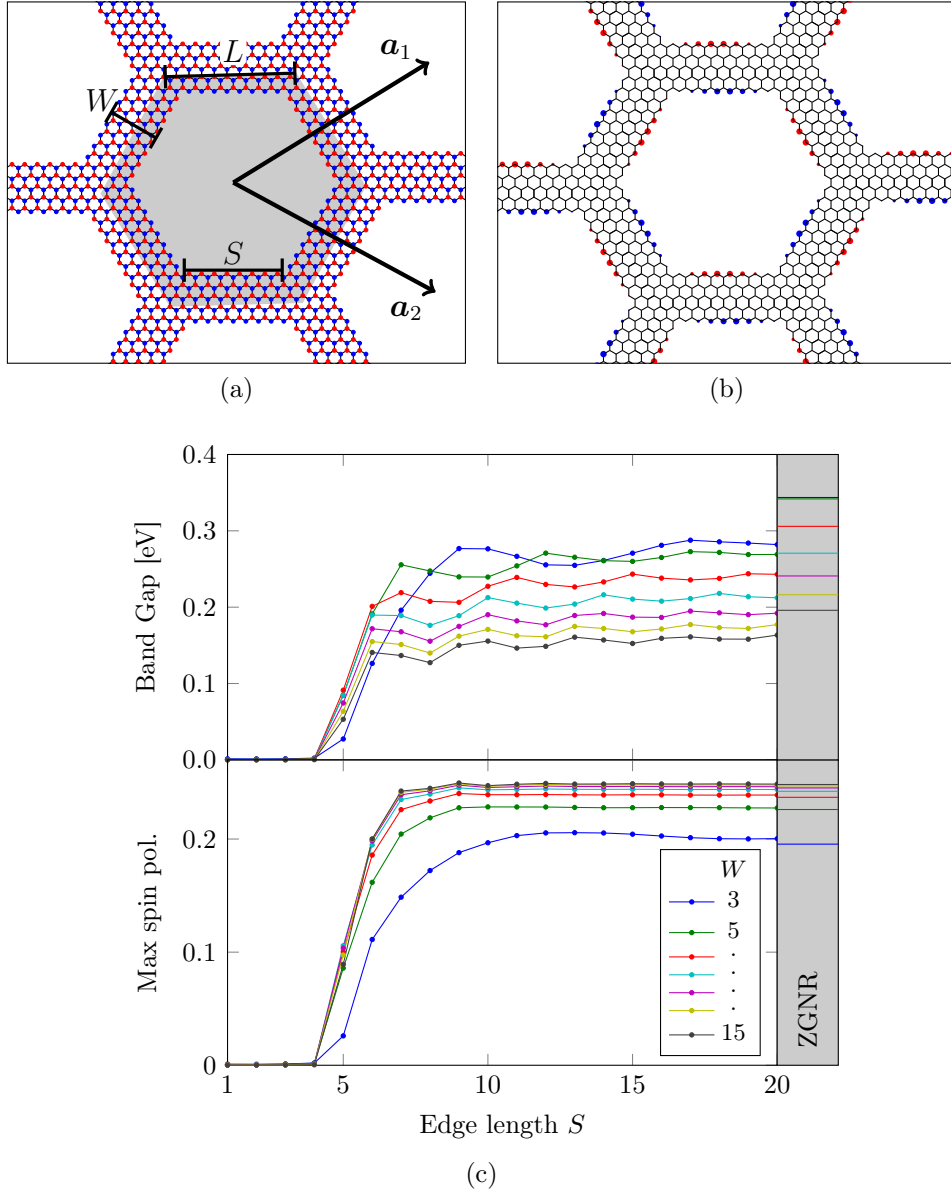


Figure 3.16: Triangular GHAL with uneven width. (a) The shaded region is the unit cell with parameters $\{5, 8\}$ and $L = 10.5$. Compared to unit cells of even W (figure 3.12a), the unit cell is slightly rotated. (b) Ground state spin density of the GHAL shown in (a). (c) Band gap and max spin polarization of uneven width triangular GHAL with properties of corresponding ZGNRs shown in the shaded region.

3. RESULTS AND DISCUSSION

length 1 shorter than for the even width case. The spin polarization then increases to approximately the ZGNR edge value. For $S < 5$ the band gap is zero, but for $S \geq 5$ the spin polarization opens a band gap which is ~ 0.05 eV smaller than the ZGNR band gap.

It was shown by Ouyang *et al.* [24] that for GHALs with uneven width the band gap was zero for small holes. This is confirmed here, but for larger holes an appreciable band gap opens. Thus, while the tight binding band gap is only significant for small holes and even widths, the spin polarization band gap is significant for larger holes and independent of the specific unit cell configuration.

We now examine GHALs where the graphene layer has been rotated 30° . Thus the unit cell vectors are at an angle of 30° or 90° to the carbon bonds, unlike the previous cases where the unit cell vector was parallel or at an angle of 60° to the carbon bonds. The unit cell is shown in figure 3.17a and is seen to consist of triangular domains of side length S with junctions of width W to three other triangles. We define the parameter L as the length of the edge of the unit cell, and thus $W = L - 2S$. We use the notation $\{W, S\}_R$ for defining unit cells of rotated GHALs.

Using 1NN tight binding calculations, Petersen *et al.* [21] showed that for $L = 3n$ with n being an integer a significant band gap was found, while for other cases the structure was metallic. This is also the case for 3NN tight binding as shown in figure 3.17c. The band gap of the semiconducting structures is seen to decrease with increasing edge length being ≈ 0 eV for $S \geq 6$.

Including the Hubbard interaction the system becomes spin polarized. The spin polarization is seen to begin at $3 \leq S < 6$ for $W < 8$. An example of the antiferromagnetic ground state is shown in figure 3.17a, where the triangular domains are seen to be spin polarized as either spin up or down. For small widths the edges of the triangles can interact with each other, lowering the energy barrier for spin polarization and resulting in holes of smaller edge lengths being spin polarized. For $S \geq 6$ all examined structures are spin polarized with a maximum spin polarization ≈ 0.25 for increasing S .

The spin polarization introduces a band gap for all structures regardless of L value. For the examined parameters the band gap is found to be from 0.1 eV to 0.3 eV and decrease with the edge length. This is also the case for bowtie flakes shown in figure 3.9, and the band gap is found to be of the same magnitude as for bowties. The band gap is found to decrease with increasing W , but no clear order is present.

It is concluded that the spin polarization band gap is a significant effect for GHALs with zigzag edges. While the tight binding band gap decreases

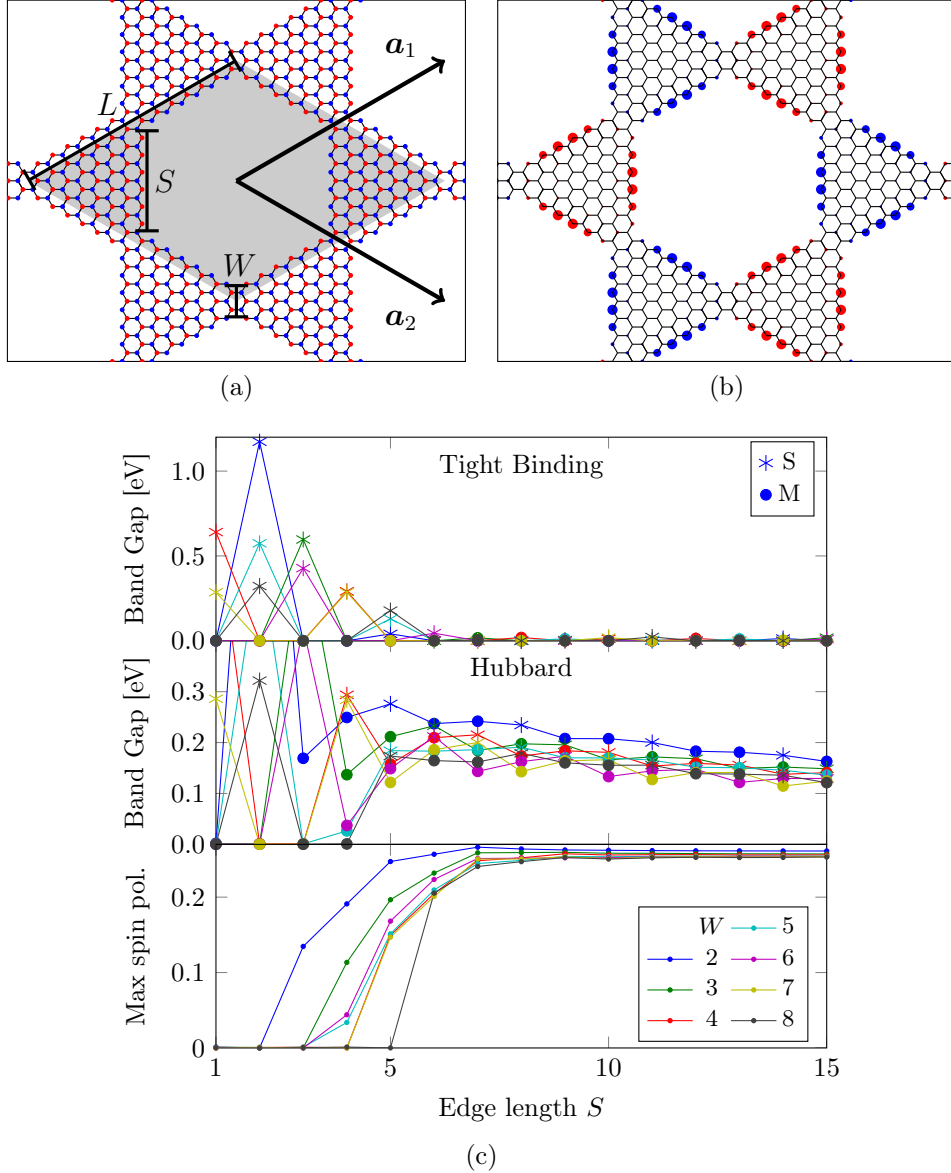


Figure 3.17: (a) Unit cell of rotated triangular GHAL with parameters $\{2,6\}_R$ and $L = 14$. (b) Ground state spin density of the GHAL shown in (a). (c) Band gaps of rotated triangular GHALs determined using the tight binding model (top) and Hubbard model (middle). Petersen et al. [21] determined that for $L = 3n$ where n is an integer the structure was semi-conducting in a 1NN TB model, and thus we label those structures with a star (*) and metallic structures with a dot (•). The bottom plot is the max spin polarization.

with hole size and becomes insignificant the spin polarization band gap is significant for large holes and depends on the dimensions and arrangement of the remaining atoms.

3.3.2 Ferromagnetic States

By preparing the GHAL systems in a ferromagnetic electron configuration and iterating until convergence, a metastable ferromagnetic electron configuration is found. We consider GHALs with even width of the type shown in figure 3.12a. A ferromagnetic spin density is shown in figure 3.18a. It is found that the spin density is similar to the spin density of the antiferromagnetic configuration with all spins being aligned.

Examining the spin resolved density of states shown in figure 3.18b it is seen that 1 spin down and 3 spin up groups of bands are just below the Fermi level. Each group consist of 3 bands, and thus there is a surplus of 6 spin up electrons per unit cell, 1 for each edge. The band gap is found as the minimum energy required for excitation of an electron to a conduction band where the spin is conserved. We note that the spin splitting gap between the valence spin up and conduction spin down bands is significantly smaller than the band gap.

The band gap and total spin is shown in figure 3.18c for GHALs. It is seen that the onset of spin polarization varies from $6 \leq S < 9$. The majority of the total spins have the value $3n$ where n is an integer, with the total spin increasing with increased edge length. Thus the balance of spin up and spin down bands shifts with groups of 3 bands at a time, resulting in the number of unpaired electrons increasing with 1 per edge. Furthermore it is seen that for $W = 16$ and $S > 13$ the total spin increases when S increases with 3, corresponding to 1 electron added for 3 edge atoms. This is in correspondence with the $1/3$ unpaired electrons per edge found for ZGNRs of large widths.

The band gap is found to decrease with increasing edge length and increase when the total spin increases by 3. This is in agreement with the results for square graphene flakes shown in figure 3.10. For the cases where the total spin takes values $\neq 3n$ the band gap decreases dramatically, corresponding to a transition within a group of 3 bands. For the case of $S \rightarrow \infty$ it is expected that the band gap goes to zero as in the ZGNR case, and for the largest holes explored here where $S = 20$ the band gap is approximately 0.1 eV.

The magnetic interaction energy, the difference between the total energy of the ferromagnetic and antiferromagnetic states, is presented in figure 3.19 for some of the structures examined. The energy is divided by $3S$, so it is

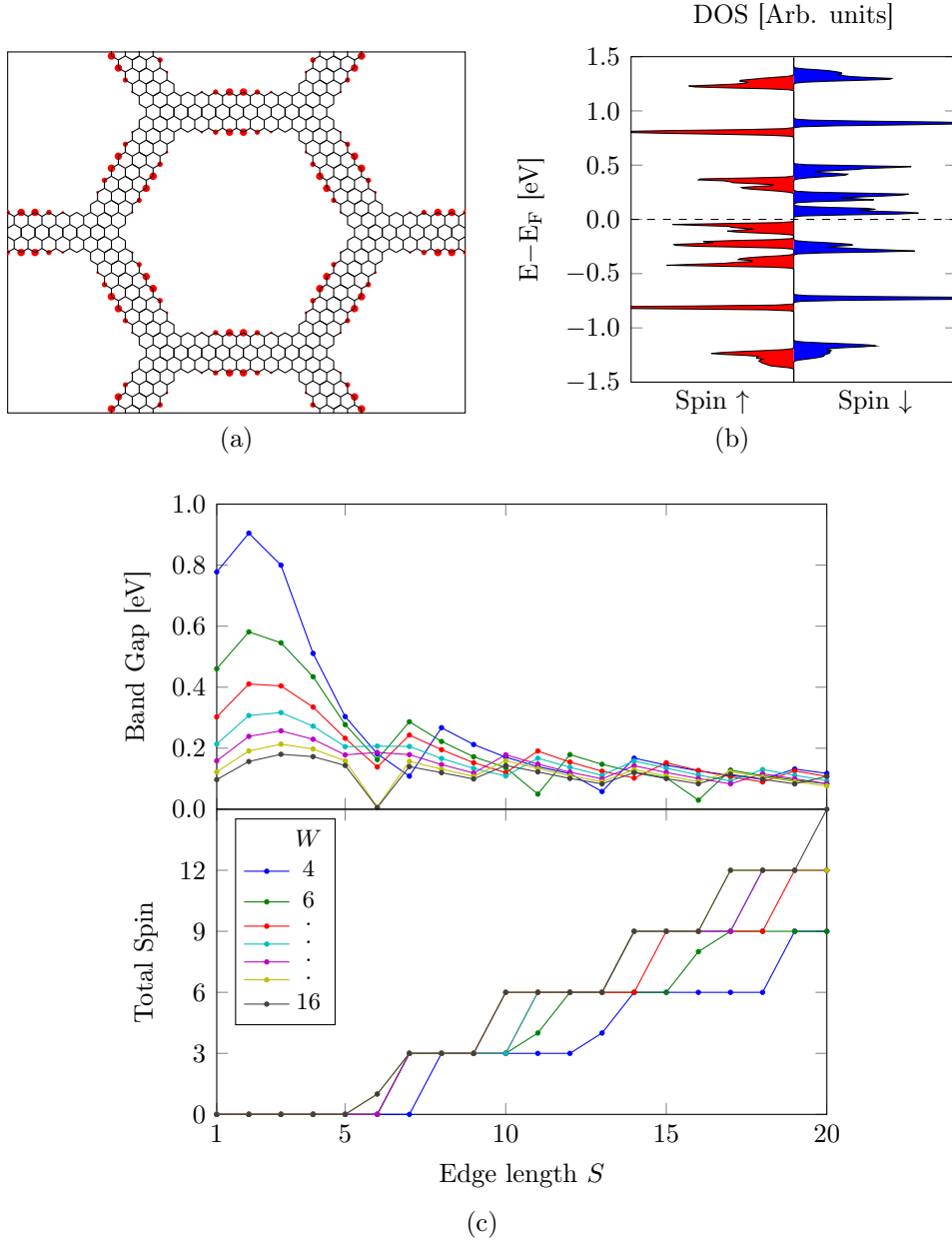


Figure 3.18: (a) Metastable ferromagnetic spin density of $\{4, 8\}$ GHAL. (b) Spin resolved density of states of $\{4, 8\}$ GHAL. (c) Band gap (top) and total spin (bottom) of ferromagnetic states in GHALs. The total spin is found to mainly increase in steps of 3. When the total spin is different from $3n$ with n an integer the corresponding band gap is significantly lower. The systems $\{10, 6\}$ and $\{12, 6\}$ converged to an antiferromagnetic electronic configuration.

3. RESULTS AND DISCUSSION

the magnetic interaction energy per 2 edge atoms corresponding to the ZGNR unit cell and the energy can be directly compared to figure 3.8d (assuming no contribution from the junctions). The magnetic interaction energy is found to be positive for $S \geq 6$ corresponding to the emergence of antiferromagnetic states. After the onset of ferromagnetism, the magnitude of the magnetic interaction is found to be in the interval from 2.5 to 7.5 meV. This is in agreement with the magnitudes found for ZGNRs.

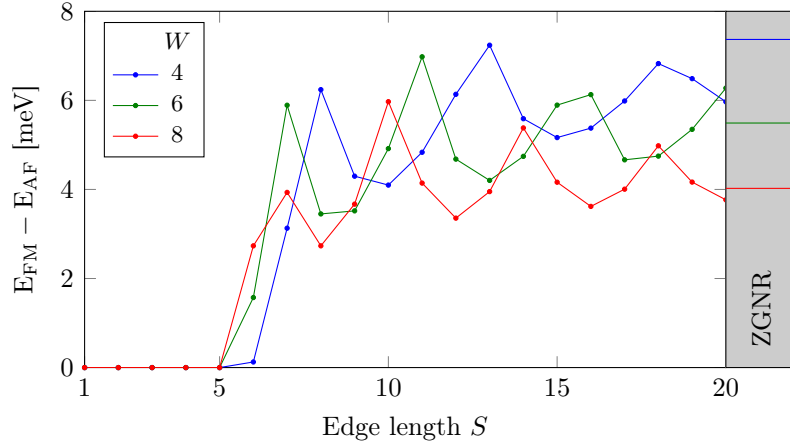


Figure 3.19: *Difference in total energy per 2 edge atoms between ferromagnetic and antiferromagnetic states of GHALs (left) and ZGNRs (right, shaded region) determined using the 3NN Hubbard model in equation (2.21).*

3.3.3 Stability of spin polarization

It was shown in figure 3.14 that above the Fermi level a number of states localized on the same edge and sublattice but with opposite spin are present. Thus modifying the distribution of electrons by doping or temperature might modify the spin properties and quench the band gap. Here, we explore how the band gap and spin polarization of antiferromagnetic GHALs with even width are modified by temperature and electron doping.

We assume the electrons are either injected by a charge reservoir or that the dopant concentration is sufficiently small that the electronic properties are not changed significantly. We thus model the added electrons as a shift of the Fermi energy supplying additional electrons. P doping is not considered in this work. The calculations were conducted at room temperature.

In figure 3.20 it is shown how the band gap and spin polarization of different GHALs are modified by a fractional doping up to 1%. The band

gap is assumed to be across the same valence-conduction transition as the undoped case as the doping concentrations are low. While the spin polarization is still significant, the band gap and max spin polarization is found to decrease linearly with doping concentration. As the spin polarization approaches 0 the band gap decreases nonlinearly. This is an effect caused by the finite temperature. The band gap decreases with the spin polarization, reducing to the tight binding value when the structure becomes paramagnetic.

Describing the rate of change in polarization as $\Delta p_{max} = -\alpha \Delta n$, where α is a proportionality factor and Δn is the doping concentration, it is found that for a fixed hole size S , α increases with increased width W of the structure. For a fixed width α is found to decrease with increased hole size. This can be explained by noting that the doping applied is proportional to the number of atoms in the unit cell and the number of unpaired electrons is proportional to the number of edge atoms ($1/3$ per atom for $W \rightarrow \infty$ and $S \rightarrow \infty$ as shown in figure 3.5). Thus it is found that

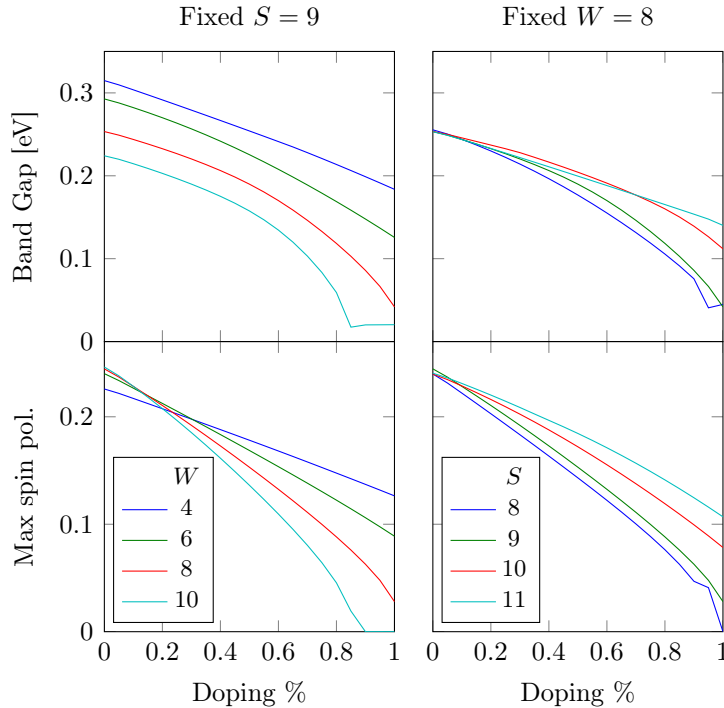


Figure 3.20: Band gap and max spin polarization for even width GHALs as a function of electron doping. The doping corresponds to adding electrons as a fraction of the number of atoms in the unit cell.

3. RESULTS AND DISCUSSION

$$\alpha \propto \frac{N_{edge}}{N_{atoms}} = \frac{6S}{1.5W^2 + 6SW},$$

where N_{edge} is the number of edge atoms and N_{atoms} the number of atoms per unit cell. For $S \rightarrow \infty$ the ratio N_{edge}/N_{atoms} reduces to W^{-1} , the ZGNR case.

In order to fully address the case of substitutional doping the effects of including dopant atoms must be addressed further, e.g. using methods as presented by Pedersen and Pedersen [55]. Furthermore, it was shown by Jung and MacDonald [56] that the phase diagram of doped ZGNRs switches between ferromagnetic, antiferromagnetic and paramagnetic states for increased doping, which was not considered in this work.

Next we consider the temperature stability of the spin polarization in GHALs. We model the antiferromagnetic systems by applying finite temperature Fermi-Dirac statistics for calculating the electron density. The results are shown in figure 3.21. It is found that for temperatures above ≈ 1000 K the spin polarization goes to zero, and the band gap decreases to the tight binding value. Thus at a temperature of ≈ 1000 K the structure becomes paramagnetic with no spin order. For antiferromagnetic materials

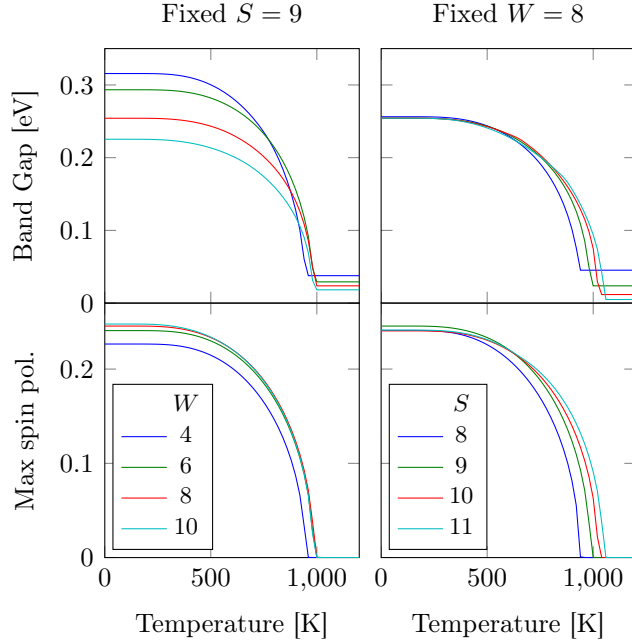


Figure 3.21: *Band gap and max spin polarization for even width GHALs as a function of temperature.*

this temperature is known as the Néel temperature.

At room temperatures the band gap and spin polarization is close to the 0 K case. The local polarization decreases smoothly with the temperature until it reaches the Néel temperature. Thus the antiferromagnetic / paramagnetic transition is classified as a second order transition [31]. As the temperature increases, electrons are excited to states above the band gap. These conduction states are localized on the edges with spin opposite to the valence edge states, thus lowering the spin polarization. This lowers the band gap, allowing more electrons to be excited across the band gap.

The results indicate that for room temperatures and low doping the effects of spin polarization of zigzag GHALs are significant and modify the band gap of the structures significantly. In the present discussion of temperature effects the effect of spin correlation length is ignored. According to calculations by Yazyev and Katsnelson [57], the spin correlation length is on the order of ~ 1 nm at room temperature, limiting the long range magnetic ordering in graphene structures.

3.3.4 Optical response

For demonstrating the effect of inclusion of the Hubbard interaction we calculate the optical conductivity of a set of GHALs including and excluding the Hubbard interaction. The results are shown in figure 3.22. It is found that for $S < 6$ the optical properties are approximately equal with and without the Hubbard interaction. This is expected as before the onset of polarization the band structures are identical. For $S \geq 6$ the antiferromagnetic ground states appears, and the band gap stabilizes at a fixed value. This is seen in the optical spectrum as the absorption edge is shifted to higher energies compared to the tight binding calculations.

In the calculations of the optical spectra a broadening of 20 meV was introduced by convolution with a Gaussian line shape function as suggested by Pedersen *et al.* [43]. The inhomogeneous broadening is introduced as fabrication of samples will introduce irregularities, and variations of shape, size of holes and geometrical disorder will broaden the peaks in the optical spectra. The broadening blurs the details of the spectra. An extensive study of disorder in graphene was conducted by Yuan *et al.* [58], who found that a considerable amount of geometrical disorder was required before the features of the optical spectra were indistinguishable.

3. RESULTS AND DISCUSSION

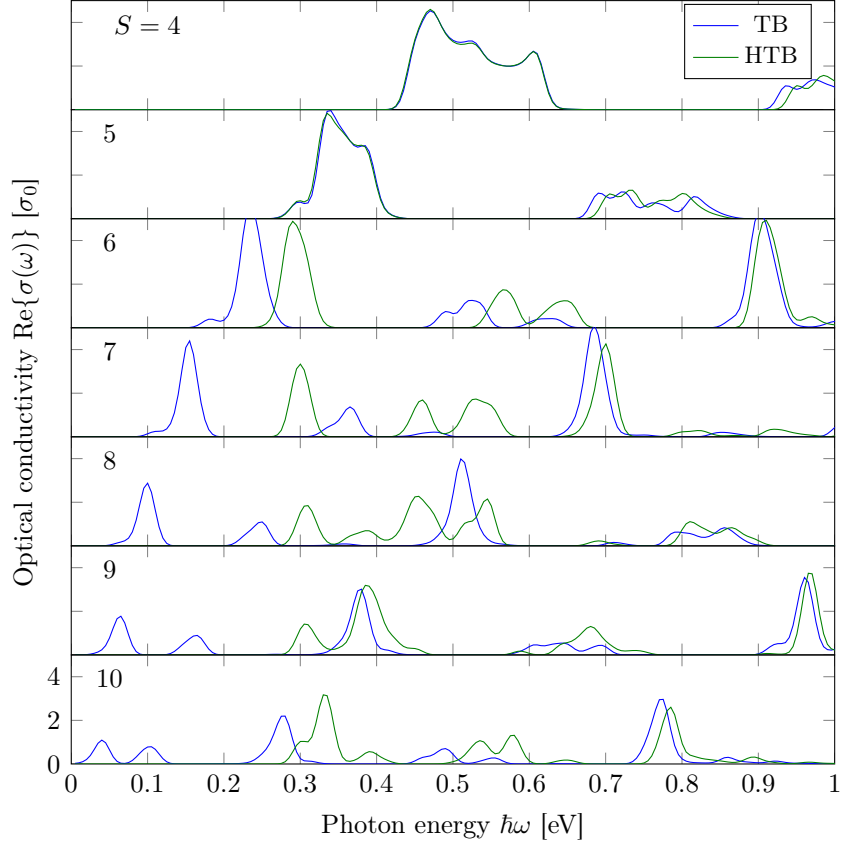


Figure 3.22: *Optical conductivity of GHALs with width 6 and edge length 4-10 shown in top left corner. The calculations are conducted including and excluding the Hubbard interaction and with a broadening of $\hbar\Gamma = 20$ meV. The units of the optical conductivity are $\sigma_0 = e^2/4\hbar$, the optical conductivity of graphene at $\hbar\omega = 0$.*

Conclusion

In the framework of the mean field Hubbard model with third nearest neighbour interactions it was found that zigzag edges of nanostructured graphene become antiferromagnetic with local magnetic moments up to $\approx \mu_B/3$ per zigzag edge atom. Critical sizes for the number of zigzag edge atoms were identified above which the zigzag edge became spin polarized. The critical size was found to depend on the edge corner angle and was for 0D structures found to be 9 graphene lattice constants for 120° corners and 4 graphene lattice constants for 90° corners. For 60° angles no critical size was found.

For all structures examined the band gap was found to decrease with increased size of the smallest dimension of the structure. For hexagonal holes in a triangular lattice the band gap is found to depend on the width of the corresponding ZGNR. For large holes the band gaps are found to be within 0.05 eV of the band gap of the corresponding ZGNR. Thus the band gaps of these structures cannot be approximated with the scaling law proposed by Pedersen *et al.* [20]. The inclusion of electron-electron repulsion blue shifted the optical response of the structures.

For a metastable ferromagnetic state for hexagonal holes in a triangular lattice, the band gap was found to decrease for increased hole size approaching zero for infinite size. The magnetic interaction energy was found to decrease with the width of the structure and for small widths it was ~ 5 meV.

The antiferromagnetic state of hexagonal holes in a triangular lattice was found to depolarize for a temperature of ~ 1000 K and doping of $\sim 1\%$ impurities. At room temperatures and low doping the electric and optical properties are changed significantly by inclusion of electron-electron interactions in a mean field approach.

Bibliography

- [1] KS Novoselov, AK Geim, SV Morozov, D Jiang, Y Zhang, SV Dubonos, IV Grigorieva, and AA Firsov. “Electric field effect in atomically thin carbon films”. In: *Science* 306.5696 (2004), pp. 666–669 (cit. on p. 1).
- [2] KS Novoselov, VI Fal, L Colombo, PR Gellert, MG Schwab, K Kim, *et al.* “A roadmap for graphene”. In: *Nature* 490.7419 (2012), pp. 192–200 (cit. on p. 1).
- [3] Alfonso Reina, Xiaoting Jia, John Ho, Daniel Nezich, Hyungbin Son, Vladimir Bulovic, Mildred S Dresselhaus, and Jing Kong. “Large area, few-layer graphene films on arbitrary substrates by chemical vapor deposition”. In: *Nano letters* 9.1 (2008), pp. 30–35 (cit. on p. 1).
- [4] Semiconductor Industry Association. *The International Technology Roadmap for Semiconductors*. 2012. URL: <http://www.itrs.net/Links/2012ITRS/Home2012.htm> (cit. on p. 2).
- [5] Frank Schwierz. “Graphene transistors”. In: *Nature nanotechnology* 5.7 (2010), pp. 487–496 (cit. on p. 2).
- [6] Melinda Y Han, Barbaros Özyilmaz, Yuanbo Zhang, and Philip Kim. “Energy band-gap engineering of graphene nanoribbons”. In: *Physical Review Letters* 98.20 (2007), p. 206805 (cit. on p. 2).
- [7] Xiaolin Li, Xinran Wang, Li Zhang, Sangwon Lee, and Hongjie Dai. “Chemically derived, ultrasmooth graphene nanoribbon semiconductors”. In: *Science* 319.5867 (2008), pp. 1229–1232 (cit. on p. 2).
- [8] C Stampfer, J Güttinger, S Hellmüller, F Molitor, K Ensslin, and T Ihn. “Energy gaps in etched graphene nanoribbons”. In: *Physical review letters* 102.5 (2009), p. 56403 (cit. on p. 2).

- [9] Y.W. Son, M.L. Cohen, and S.G. Louie. “Energy gaps in graphene nanoribbons”. In: *Physical Review Letters* 97.21 (2006), p. 216803 (cit. on pp. 2, 24–27).
- [10] Motohiko Ezawa. “Peculiar width dependence of the electronic properties of carbon nanoribbons”. In: *Physical Review B* 73.4 (2006), p. 045432 (cit. on p. 2).
- [11] Chenggang Tao, Liying Jiao, Oleg V Yazyev, Yen-Chia Chen, Juanjuan Feng, Xiaowei Zhang, Rodrigo B Capaz, James M Tour, Alex Zettl, Steven G Louie, *et al.* “Spatially resolving edge states of chiral graphene nanoribbons”. In: *Nature Physics* 7.8 (2011), pp. 616–620 (cit. on p. 2).
- [12] Myungwoong Kim, Nathaniel S Safron, Eungnak Han, Michael S Arnold, and Padma Gopalan. “Fabrication and characterization of large-area, semiconducting nanoperforated graphene materials”. In: *Nano letters* 10.4 (2010), pp. 1125–1131 (cit. on p. 2).
- [13] Jingwei Bai, Xing Zhong, Shan Jiang, Yu Huang, and Xiangfeng Duan. “Graphene nanomesh”. In: *Nature nanotechnology* 5.3 (2010), pp. 190–194 (cit. on p. 2).
- [14] Milan Begliarbekov, Onejae Sul, John Santanello, Nan Ai, Xi Zhang, Eui-Hyeok Yang, and Stefan Strauf. “Localized states and resultant band bending in graphene antidot superlattices”. In: *Nano letters* 11.3 (2011), pp. 1254–1258 (cit. on p. 2).
- [15] Jonathan Eroms and Dieter Weiss. “Weak localization and transport gap in graphene antidot lattices”. In: *New Journal of Physics* 11.9 (2009), p. 095021 (cit. on p. 2).
- [16] Çağlar Ö Girit, Jannik C Meyer, Rolf Erni, Marta D Rossell, C Kisielowski, Li Yang, Cheol-Hwan Park, MF Crommie, Marvin L Cohen, Steven G Louie, *et al.* “Graphene at the edge: stability and dynamics”. In: *science* 323.5922 (2009), pp. 1705–1708 (cit. on p. 2).
- [17] Xiaoting Jia, Mario Hofmann, Vincent Meunier, Bobby G Sumpter, Jessica Campos-Delgado, José Manuel Romo-Herrera, Hyungbin Son, Ya-Ping Hsieh, Alfonso Reina, Jing Kong, *et al.* “Controlled formation of sharp zigzag and armchair edges in graphitic nanoribbons”. In: *Science* 323.5922 (2009), pp. 1701–1705 (cit. on p. 2).
- [18] K Tada, T Hashimoto, J Haruyama, H Yang, and M Chshiev. “Spontaneous spin polarization and spin pumping effect on edges of graphene antidot lattices”. In: *physica status solidi (b)* 249.12 (2012), pp. 2491–2496 (cit. on p. 2).

-
- [19] T Shimizu, J Nakamura, K Tada, Y Yagi, and J Haruyama. “Magnetoresistance oscillations arising from edge-localized electrons in low-defect graphene antidot-lattices”. In: *Applied Physics Letters* 100.2 (2012), pp. 023104–023104 (cit. on p. 2).
- [20] Thomas G Pedersen, Christian Flindt, Jesper Pedersen, Niels Asger Mortensen, Antti-Pekka Jauho, and Kjeld Pedersen. “Graphene antidot lattices: Designed defects and spin qubits”. In: *Physical review letters* 100.13 (2008), p. 136804 (cit. on pp. 2, 40, 42, 53).
- [21] René Petersen, Thomas Garm Pedersen, and Antti-Pekka Jauho. “Clar Sextet Analysis of Triangular, Rectangular and Honeycomb Graphene Antidot Lattices”. In: *ACS Nano* 5.1 (2011), pp. 523–529 (cit. on pp. 2, 42, 44, 45).
- [22] René Petersen, Thomas Garm Pedersen, and Antti-Pekka Jauho. “Clar sextets in square graphene antidot lattices”. In: *Physica E: Low-Dimensional Systems and Nanostructures* 44.6 (2012), pp. 967–970 (cit. on p. 2).
- [23] Joachim Alexander Fürst, Jesper Goor Pedersen, Christian Flindt, Niels Asger Mortensen, Mads Brandbyge, Thomas G Pedersen, and Antti-Pekka Jauho. “Electronic properties of graphene antidot lattices”. In: *New Journal of Physics* 11.9 (2009), p. 095020 (cit. on pp. 2, 27).
- [24] Fangping Ouyang, Shenglin Peng, Zhongfan Liu, and Zhirong Liu. “Bandgap opening in graphene antidot lattices: the missing half”. In: *ACS nano* 5.5 (2011), pp. 4023–4030 (cit. on pp. 2, 40, 42, 44).
- [25] Wei Liu, ZF Wang, QW Shi, Jinlong Yang, and Feng Liu. “Band-gap scaling of graphene nanohole superlattices”. In: *Physical Review B* 80.23 (2009), p. 233405 (cit. on pp. 2, 40).
- [26] HY He, Y Zhang, and BC Pan. “Tuning electronic structure of graphene via tailoring structure: Theoretical study”. In: *Journal of Applied Physics* 107.11 (2010), pp. 114322–114322 (cit. on p. 2).
- [27] Decai Yu, Elizabeth M Lupton, Miao Liu, Wei Liu, and Feng Liu. “Collective magnetic behavior of graphene nanohole superlattices”. In: *Nano Research* 1.1 (2008), pp. 56–62 (cit. on pp. 2, 38).
- [28] J. Hubbard. “Electron correlations in narrow energy bands”. In: *Proceedings of the Royal Society of London. Series A. Mathematical and Physical Sciences* 276.1365 (1963), pp. 238–257 (cit. on pp. 3, 11).
- [29] J.P. Dahl. *Introduction to the quantum world of atoms and molecules*. World Scientific Pub Co Inc, 2001. ISBN: 9810245653 (cit. on p. 4).

- [30] J.C. Slater and GF Koster. “Simplified LCAO method for the periodic potential problem”. In: *Physical Review* 94.6 (1954), p. 1498 (cit. on p. 5).
- [31] Charles Kittel. *Introduction to Solid State Physics*. 8th edition. John Wiley and Sons, Inc., 2005. ISBN: 0-471-41526-X (cit. on pp. 5, 51).
- [32] R.M. Martin. *Electronic structure: basic theory and practical methods*. Cambridge Univ Pr, 2004. ISBN: 0 521 78285 6 (cit. on pp. 5, 7).
- [33] H. Tasaki. “From Nagaoka’s ferromagnetism to flat-band ferromagnetism and beyond: An introduction to ferromagnetism in the Hubbard model”. In: *Progress of Theoretical Physics* 99.4 (1998), pp. 489–548 (cit. on pp. 9, 11).
- [34] M. Schüler, M. Rösner, T. O. Wehling, A. I. Lichtenstein, and M. I. Katsnelson. “Optimal Hubbard models for materials with nonlocal Coulomb interactions: graphene, silicene and benzene”. In: *ArXiv e-prints* (Feb. 2013). arXiv: 1302.1437 [cond-mat.str-el] (cit. on p. 11).
- [35] H. Fehske, R. Schneider, and A. Weisse. *Computational many-particle physics*. 739. Springer Verlag, 2008. ISBN: 978-3-540-74686-7 (cit. on pp. 11, 12).
- [36] H. Bruus and K. Flensberg. *Many-body quantum theory in condensed matter physics: an introduction*. Oxford University Press, USA, 2004 (cit. on pp. 13, 62, 65).
- [37] M. Ijäs and A. Harju. “Lattice density-functional theory on graphene”. In: *Physical Review B* 82.23 (2010), p. 235111 (cit. on pp. 13, 15).
- [38] Dirk Porezag, Th Frauenheim, Th Köhler, Gotthard Seifert, and R Kaschner. “Construction of tight-binding-like potentials on the basis of density-functional theory: Application to carbon”. In: *Physical Review B* 51.19 (1995), p. 12947 (cit. on p. 16).
- [39] Intel. *Non-Commercial Software Development*. July 2013. URL: <http://software.intel.com/en-us/non-commercial-software-development> (cit. on p. 17).
- [40] Intel Math Kernel Library. *HEEVR routine documentation*. July 2013. URL: <http://software.intel.com/sites/products/documentation/hpc/mkl/mklman/GUID-917A3B87-1503-4458-97AC-EE84F972CECC.htm> (cit. on p. 18).
- [41] OpenMP Architecture Review Board. *The OpenMP® API specification for parallel programming*. July 2013. URL: <http://openmp.org/> (cit. on p. 18).

-
- [42] J. Kohanoff. *Electronic structure calculations for solids and molecules: theory and computational methods*. Condensed matter physics, nanoscience and mesoscopic physics. Cambridge University Press, 2006. ISBN: 9780521815918 (cit. on p. 19).
- [43] T.G. Pedersen, C. Flindt, J. Pedersen, A.P. Jauho, N.A. Mortensen, and K. Pedersen. “Optical properties of graphene antidot lattices”. In: *Physical Review B* 77.24 (2008), p. 245431 (cit. on pp. 19, 21, 51).
- [44] Thomas Garm Pedersen, Kjeld Pedersen, and Thomas Brun Kristensen. “Optical matrix elements in tight-binding calculations”. In: *Physical Review B* 63.20 (2001), p. 201101 (cit. on p. 20).
- [45] T.G. Pedersen and L. Diekhöner. *Electrical, Optical & Magnetic Properties of Nanostructures*. Aalborg University, 2012 (cit. on p. 21).
- [46] Y Hancock, A Uppstu, K Saloriutta, A Harju, and MJ Puska. “Generalized tight-binding transport model for graphene nanoribbon-based systems”. In: *Physical Review B* 81.24 (2010), p. 245402 (cit. on pp. 23, 24, 26, 27).
- [47] Joachim A Fürst, Thomas G Pedersen, Mads Brandbyge, and Antti-Pekka Jauho. “Density functional study of graphene antidot lattices: Roles of geometrical relaxation and spin”. In: *Physical Review B* 80.11 (2009), p. 115117 (cit. on p. 26).
- [48] Tue Gunst, Troels Markussen, Antti-Pekka Jauho, and Mads Brandbyge. “Thermoelectric properties of finite graphene antidot lattices”. In: *Physical Review B* 84.15 (2011), p. 155449 (cit. on pp. 26, 27).
- [49] L Pisani, JA Chan, B Montanari, and NM Harrison. “Electronic structure and magnetic properties of graphitic ribbons”. In: *Physical Review B* 75.6 (2007), p. 064418 (cit. on pp. 28, 30).
- [50] Wei L Wang, Oleg V Yazyev, Sheng Meng, and Efthimios Kaxiras. “Topological frustration in graphene nanoflakes: Magnetic order and spin logic devices”. In: *Physical review letters* 102.15 (2009), p. 157201 (cit. on p. 32).
- [51] Oleg V Yazyev. “Emergence of magnetism in graphene materials and nanostructures”. In: *Reports on Progress in Physics* 73.5 (2010), p. 056501 (cit. on p. 32).
- [52] Somnath Bhowmick and Vijay B Shenoy. “Edge state magnetism of single layer graphene nanostructures”. In: *The Journal of chemical physics* 128 (2008), p. 244717 (cit. on p. 36).

- [53] Mads L. Trolle, Ulrik S. Møller, and Thomas G. Pedersen. “Large and stable band gaps in spin-polarized graphene antidot lattices”. In: *Appendix B (to be published)* (2013) (cit. on p. 40).
- [54] Nobuyuki Shima and Hideo Aoki. “Electronic structure of superhoneycomb systems: a peculiar realization of semimetal/semiconductor classes and ferromagnetism”. In: *Physical review letters* 71.26 (1993), pp. 4389–4392 (cit. on p. 42).
- [55] Thomas Garm Pedersen and Jesper Goor Pedersen. “Self-consistent tight-binding model of B and N doping in graphene”. In: *Physical Review B* 87.15 (2013), p. 155433 (cit. on p. 50).
- [56] J Jung and AH MacDonald. “Carrier density and magnetism in graphene zigzag nanoribbons”. In: *Physical Review B* 79.23 (2009), p. 235433 (cit. on p. 50).
- [57] Oleg V Yazyev and MI Katsnelson. “Magnetic correlations at graphene edges: basis for novel spintronics devices”. In: *Physical review letters* 100.4 (2008), p. 047209 (cit. on p. 51).
- [58] Shengjun Yuan, Rafael Roldán, Antti-Pekka Jauho, and MI Katsnelson. “Electronic properties of disordered graphene antidot lattices”. In: *Physical Review B* 87.8 (2013), p. 085430 (cit. on p. 51).

Appendix A

Second Quantization

In quantum physics, observables are represented by Hermitian operators and quantum states are represented by state vectors in a Hilbert space. The set of all eigenvectors of an Hermitian operator forms a complete basis set of the Hilbert space. The time-evolution of a state is governed by the Schrödinger equation

$$i\hbar\partial_t|\Psi(t)\rangle = \hat{H}|\Psi(t)\rangle,$$

where ∂_t is the time-derivative and $|\Psi(t)\rangle$ is the ket for a state vector in Dirac notation with a corresponding bra given as $(|\Psi\rangle)^\dagger = \langle\Psi|$.

For stationary states where \hat{H} is independent of time the time dependent part can be separated from the ket

$$|\Psi(t)\rangle = |\psi\rangle e^{-iEt/\hbar},$$

where E is the energy eigenvalue for the state $|\psi\rangle$. The energy is found from the eigenvalue equation

$$\hat{H}|\psi\rangle = E|\psi\rangle, \tag{A.1}$$

which is the time-independent Schrödinger equation. The eigenstates are normalizable and are labeled with a set of quantum numbers ν . As the Hamiltonian is a Hermitian operator the set of eigenstates for (A.1) constitutes a complete set, which is a complete basis set of the Hilbert space. This is formulated as the completeness of states

$$\sum_{\nu} |\nu\rangle\langle\nu| = 1. \tag{A.2}$$

Any state of the system can be represented as a linear combination of the eigenstates of the Hamiltonian. The eigenstates are orthogonal with each

other which for normalized eigenstates can be expressed as

$$\langle \psi_{\nu_j} | \psi_{\nu_k} \rangle = \delta_{j,k}.$$

In order to obtain the wave function of a particle in state $|\nu\rangle$, the inner product of the position bra $\langle \mathbf{r} |$ is taken with the ket

$$\langle \mathbf{r} | \nu \rangle = \psi_{\nu}(\mathbf{r})$$

[36]

Many-particle systems

The wavefunction of a system consisting of N identical particles is

$$\psi(\mathbf{r}_1, \mathbf{r}_2, \dots, \mathbf{r}_N), \tag{A.3}$$

which is interpreted by taking the absolute square, which is the probability of finding each of the N particles inside the volume $d\mathbf{r}_j$ surrounding the point \mathbf{r}_j for $j \in N$:

$$|\psi(\mathbf{r}_1, \mathbf{r}_2, \dots, \mathbf{r}_N)|^2 \prod_{j=1}^N d\mathbf{r}_j.$$

Identical particles are indistinguishable. Thus by interchange of two coordinates in the N -particle wavefunction the same physical state results. Thus the state function can at most differ by a prefactor. For fermions such as electrons, the prefactor has the value -1 , so by interchanging two electrons from the wavefunction (A.3) the result is

$$\psi(\mathbf{r}_1, \dots, \mathbf{r}_i, \dots, \mathbf{r}_j, \dots, \mathbf{r}_N) = -\psi(\mathbf{r}_1, \dots, \mathbf{r}_j, \dots, \mathbf{r}_i, \dots, \mathbf{r}_N) \tag{A.4}$$

The N -particle wavefunction (A.3) can be expressed as a linear combination of a complete, orthonormal set of single-particle states $\{\psi_{\nu}(\mathbf{r})\}$. However, in order to satisfy the requirement of indistinguishability the basis for the N -particle wavefunction is chosen to obey the requirement of indistinguishability. This is achieved by using the fermionic anti-symmetrization operator \hat{S}_- , which is defined

$$\hat{S}_- \prod_{j=1}^N \psi_{\nu_j}(\mathbf{r}_j) = \begin{vmatrix} \psi_{\nu_1}(\mathbf{r}_1) & \psi_{\nu_1}(\mathbf{r}_2) & \cdots & \psi_{\nu_1}(\mathbf{r}_N) \\ \psi_{\nu_2}(\mathbf{r}_1) & \psi_{\nu_2}(\mathbf{r}_2) & \cdots & \psi_{\nu_2}(\mathbf{r}_N) \\ \vdots & \vdots & \ddots & \vdots \\ \psi_{\nu_N}(\mathbf{r}_1) & \psi_{\nu_N}(\mathbf{r}_2) & \cdots & \psi_{\nu_N}(\mathbf{r}_N) \end{vmatrix}. \tag{A.5}$$

Thus the fermionic anti-symmetrization operator operating on a product of single-particle states forms a determinant. By interchange of two electrons the determinant obeys equation (A.4). The normalized determinant is denoted the Slater determinant, and the basis for the N -particle wavefunction is chosen as Slater determinants.

In second quantization, the Slater determinant of an N electron state is

$$|n_{\nu_1}, n_{\nu_2}, n_{\nu_3}, \dots\rangle, \quad \sum_j n_{\nu_j} = N,$$

where n_{ν_j} is the occupation number of the state $|\nu_j\rangle$. For fermions the occupation number is either 0 or 1 in agreement with the Pauli exclusion principle. The basis of the state is the complete and ordered set of single-particle states $\{|\nu_1\rangle, |\nu_2\rangle, |\nu_3\rangle, \dots\}$.

The relation between the basis states of the first and second quantization is

$$\hat{S}_- |\psi_{\nu_{n_1}}(\mathbf{r}_1)\rangle |\psi_{\nu_{n_2}}(\mathbf{r}_2)\rangle \cdots |\psi_{\nu_{n_N}}(\mathbf{r}_N)\rangle = \hat{c}_{\nu_{n_1}}^\dagger \hat{c}_{\nu_{n_2}}^\dagger \cdots \hat{c}_{\nu_{n_N}}^\dagger |0\rangle,$$

where the operator $\hat{c}_{\nu_j}^\dagger$ is the fermion creation operator. The Hermitian conjugate of the creation operator is the fermion annihilation operator, \hat{c}_{ν_j} . The operators either lowers or raises the occupation number by one. Thus by operating on a state

$$\begin{aligned} \hat{c}_{\nu_j}^\dagger |\dots, n_{\nu_{j-1}}, n_{\nu_j}, n_{\nu_{j+1}}, \dots\rangle &= C_+(n_{\nu_j}) |\dots, n_{\nu_{j-1}}, n_{\nu_j} + 1, n_{\nu_{j+1}}, \dots\rangle, \\ \hat{c}_{\nu_j} |\dots, n_{\nu_{j-1}}, n_{\nu_j}, n_{\nu_{j+1}}, \dots\rangle &= C_-(n_{\nu_j}) |\dots, n_{\nu_{j-1}}, n_{\nu_j} - 1, n_{\nu_{j+1}}, \dots\rangle. \end{aligned}$$

The normalization constants $C_-(1) = C_+(0)$ are chosen to be 1. As an unoccupied state cannot be emptied further, operation of the annihilation operator on an empty state must yield $\hat{c}_{\nu_j} |\dots, 0, \dots\rangle = 0$, so the normalization constant $C_-(0) = 0$.

As the basis states must obey the fermionic antisymmetry for interchange of electron coordinates, the following must be obeyed:

$$\hat{c}_{\nu_j}^\dagger \hat{c}_{\nu_k}^\dagger |\dots, n_{\nu_j} = 0, \dots, n_{\nu_k} = 0, \dots\rangle = -\hat{c}_{\nu_k}^\dagger \hat{c}_{\nu_j}^\dagger |\dots, n_{\nu_k} = 0, \dots, n_{\nu_j} = 0, \dots\rangle.$$

For this to be true the creation operators must anticommute, and by Hermitian conjugation also the annihilation operators. This leads to the anti-commutator relations

$$\{\hat{c}_{\nu_j}^\dagger, \hat{c}_{\nu_k}^\dagger\} = \{\hat{c}_{\nu_j}, \hat{c}_{\nu_k}\} = 0. \quad (\text{A.6})$$

Furthermore we require that $\hat{c}_{\nu_j}^\dagger$ and \hat{c}_{ν_k} anticommute for $j \neq k$:

$$\{\hat{c}_{\nu_j}^\dagger, \hat{c}_{\nu_k}\} = \delta_{\nu_j, \nu_k}. \quad (\text{A.7})$$

A consequence of (A.6) is the identity $(\hat{c}_{\nu_j}^\dagger)^2 = (\hat{c}_{\nu_j})^2 = 0$. Thus both the creation and annihilation operators will annihilate a state if they act on the state twice. We now define the number operator as

$$\hat{n}_{\nu_j} = \hat{c}_{\nu_j}^\dagger \hat{c}_{\nu_j}. \quad (\text{A.8})$$

Making \hat{n}_{ν_j} operate twice results in

$$(\hat{n}_{\nu_j})^2 = \hat{c}_{\nu_j}^\dagger \hat{c}_{\nu_j} \hat{c}_{\nu_j}^\dagger \hat{c}_{\nu_j} = \hat{c}_{\nu_j}^\dagger (\hat{c}_{\nu_j} \hat{c}_{\nu_j}^\dagger) \hat{c}_{\nu_j} = \hat{c}_{\nu_j}^\dagger (1 - \hat{c}_{\nu_j}^\dagger \hat{c}_{\nu_j}) \hat{c}_{\nu_j} = \hat{c}_{\nu_j}^\dagger \hat{c}_{\nu_j} = \hat{n}_{\nu_j},$$

where (A.7) was used. This can be restated as

$$\hat{n}_{\nu_j}(\hat{n}_{\nu_j} - 1) = 0,$$

and thus the eigenvalues of \hat{n}_{ν_j} can only be either 0 or 1. The operation of the fermionic annihilation and creation operators can then be summarized as

$$\begin{aligned} \hat{n}_\nu |n_\nu\rangle &= n_\nu |n_\nu\rangle, & n_\nu &= 0, 1 \\ \hat{c}_\nu |0\rangle &= 0, & \hat{c}_\nu^\dagger |0\rangle &= |1\rangle, & \hat{c}_\nu |1\rangle &= |0\rangle, & \hat{c}_\nu^\dagger |1\rangle &= 0. \end{aligned} \quad (\text{A.9})$$

One- and Two-electron Operators

We start by examining the one-electron operator for the kinetic energy. The operator is

$$\hat{T}_j = -\frac{\hbar^2}{2m} \nabla_{\mathbf{r}_j}^2.$$

Using the completeness of states (A.2) this can be rewritten as

$$\begin{aligned} \hat{T}_j &= \sum_{\nu_a, \nu_b} |\psi_{\nu_b}(\mathbf{r}_j)\rangle \langle \psi_{\nu_b}(\mathbf{r}_j)| \hat{T}_j |\psi_{\nu_a}(\mathbf{r}_j)\rangle \langle \psi_{\nu_a}(\mathbf{r}_j)| \\ &= \sum_{\nu_a, \nu_b} T_{\nu_a, \nu_b} |\psi_{\nu_b}(\mathbf{r}_j)\rangle \langle \psi_{\nu_a}(\mathbf{r}_j)|, \end{aligned} \quad (\text{A.10})$$

where T_{ν_a, ν_b} is the matrix element of the operator \hat{T}_j for the quantum numbers ν_a and ν_b , which is

$$T_{\nu_a, \nu_b} = -\frac{\hbar^2}{2m} \int \psi_{\nu_b}^*(\mathbf{r}_j) \nabla_{\mathbf{r}_j}^2 \psi_{\nu_a}(\mathbf{r}_j).$$

The total kinetic energy of an N -particle system is then

$$\hat{T}_{tot} = \sum_{j=1}^N \hat{T}_j.$$

A two-electron operator, such as the operator for the Coulomb interaction which is $V(\mathbf{r}_j, \mathbf{r}_k) = \frac{e^2}{4\pi\epsilon_0|\mathbf{r}_j-\mathbf{r}_k|}$, is expressed as

$$\hat{V}_{j,k} = \sum_{\nu_a, \nu_b, \nu_c, \nu_d} V_{\nu_c, \nu_d, \nu_a, \nu_b} |\psi_{\nu_c}(\mathbf{r}_j)\rangle |\psi_{\nu_d}(\mathbf{r}_k)\rangle \langle \psi_{\nu_a}(\mathbf{r}_j)| \langle \psi_{\nu_b}(\mathbf{r}_k)|, \quad (\text{A.11})$$

where

$$V_{\nu_c, \nu_d, \nu_a, \nu_b} = \int \psi_{\nu_c}^*(\mathbf{r}_j) \psi_{\nu_d}^*(\mathbf{r}_k) V(\mathbf{r}_j, \mathbf{r}_k) \psi_{\nu_a}(\mathbf{r}_j) \psi_{\nu_b}(\mathbf{r}_k) d\mathbf{r}_j d\mathbf{r}_k. \quad (\text{A.12})$$

The total interaction energy is then

$$\hat{V}_{tot} = \sum_{j>k}^N \hat{V}_{j,k} = \frac{1}{2} \sum_{j \neq k}^N \hat{V}_{j,k}.$$

As the ground state electronic Hamiltonian only involves one and two electron operators, we now have the tools for describing quantum systems in the second quantization.

[36]

Appendix B

Large and stable band gaps in
spin-polarized graphene
antidot lattices

B. LARGE AND STABLE BAND GAPS IN SPIN-POLARIZED GRAPHENE ANTIDOT LATTICES

Large and stable band gaps in spin-polarized graphene antidot lattices

Mads L. Trolle,^{1,*} Ulrik S. Møller,¹ and Thomas G. Pedersen^{1,2}

¹*Department of Physics and Nanotechnology, Aalborg University, Skjernvej 4A, DK-9220 Aalborg East, Denmark*

²*Center for Nanostructured Graphene (CNG), Aalborg University, DK-9220 Aalborg East, Denmark*

(Dated: June 7, 2013)

Introducing a periodic array of holes, i.e. an antidot lattice, in a graphene sheet has been suggested as a route towards the tantalizing objective of "opening the gap" in this otherwise zero-gap semiconductor. Combining density functional and mean-field Hubbard tight-binding methods we study the effect of spin-polarization on graphene antidot lattices (GALs). Focusing on GALs with extended zigzag edges, we systematically investigate the geometry dependence of spin-polarization, electronic structure, and band gaps. A scaling law for the band gap is established demonstrating marked deviations from circular holes without spin-polarization. Furthermore, we estimate the robustness of the magnetic ordering against raised temperature and doping and, finally, consider how the optical properties are modified by spin-polarization. Our results demonstrate that large, stable band gaps are expected for a range of geometries.

I. INTRODUCTION

Graphene is today one of the most intensively studied novel materials with promising applications within, e.g., flexible two-dimensional electronics or transistor technology¹. These capabilities are facilitated by the extraordinary room-temperature electron mobility² in excess of $10^5 \text{ cm}^2\text{V}^{-1}\text{s}^{-1}$ of exfoliated graphene. Importantly, graphene can now be synthesized on wafer scale using chemical vapour deposition techniques³. However, one of the short-comings of graphene remains its vanishing band gap limiting applications as a substitute for the materials used today in semiconductor devices. Several strategies including confinement in nanoribbons^{4,5} and biased bilayer structures^{6,7} have been suggested with the ultimate goal of "opening the gap". Also, periodic arrays of holes, so-called graphene antidot lattices (GALs), have been proposed as a route towards large-scale gapped graphene⁸. Since their proposal, the physical properties of GALs have been the subject of intense theoretical research focusing on, e.g., their electronic structure⁹⁻¹⁹, optical properties²⁰ or transport capabilities²¹⁻²⁵. Many of these calculations are, with some exceptions^{10,13,14,16-19}, performed neglecting effects of spin-polarization, even though this phenomenon has been demonstrated in recent experiments on zigzag graphene nanoribbons (ZGNRs) using scanning tunnelling spectroscopic methods²⁶. Quite generally, extended regions of zigzag edges in graphene nanostructures favor spin-polarization. This is readily observed by inclusion of a mean-field Hubbard interaction in a tight-binding scheme, which modifies the electronic structure drastically near the band gap²⁷⁻²⁹. In fact, neglecting spin-polarization, ZGNRs are semi-metals characterized by two degenerate, dispersion-less bands at the Fermi level, developing a band gap of several hundred meV with inclusion of a Hubbard-type interaction - a trend also supported by more complex *ab initio* approaches⁵.

The near-perfect zigzag edges necessary for supporting spin-polarization in the aforementioned experiment

can be attributed to the production of the ZGNRs by "un-zipping" carbon nanotubes. While any edges realistically produced in GALs, usually fabricated by lithographic methods³⁰⁻³³, are considerably more disordered, post-process annealing has been shown to reconstruct disordered edges of single holes into zigzag or armchair shapes^{34,35}, making extended regions of these two edge types experimentally feasible. Recently, magnetic force microscopy has revealed spin-polarized zigzag edges in hexagonal GALs on the 100 nm scale fabricated using a nano-porous alumina template³⁶. Thus, with other GAL fabrication techniques approaching the 10 nm regime^{30,31}, special attention towards the theoretical understanding of the magnetic properties and resulting band gap modulations of antidots with extended zigzag edges is warranted.

GALs containing a dissimilar number of atoms in the *A* and *B* sub-lattices are by Lieb's theorem³⁷ predicted to display a net magnetic moment in their ground state, and extensive work has been done on the microscopic modelling of these ferromagnetic systems^{14,18,38}. In addition, GALs with an identical number of *A*- and *B*-atoms are reported to display local spin-polarization at zigzag edges, even though their net magnetic moment vanishes^{14,16}. However, this only occurs for larger holes with smaller ones remaining completely un-polarized³⁸. To our knowledge, no systematic study has been performed on the anti-ferromagnetic spin ordering of GALs with hexagonal holes of varying dimensions, and we therefore here consider spin-polarization in two families of GALs with hexagonal holes in a triangular lattice. These antidots might be envisaged as particularly well ordered reconstructions of roughly circular holes into ones dominated by zigzag edges. Also, this is exactly the structure used by Shimizu *et al.* to interpret their experimental results³⁶, see Fig. 1. We follow the nomenclature of Ref. 12 and denote such lattices, for which all lattice vectors are oriented parallel to carbon-carbon bonds as "triangular" GALs. Calculations neglecting spin-polarization have predicted these structures to be semiconducting with band gaps decreasing with increasing unit cell size

(i.e., with holes constituting a smaller fraction of the unit cell).^{10,22} However, upon rotating the holes further by $\pi/6$ around the hole centre axes, making the angle between GAL lattice vector and carbon-carbon bond $\pi/6$, only structures with a unit cell edge length of $(3n+3)a_0$ (n an arbitrary integer and a_0 the graphene lattice constant) were found to retain a sizeable band gap^{9,12}. Following Ref. 12, we term these "rotated triangular" GALs, and the question remains to what extent this simple rule for band gap opening transfers to the spin-polarized case.

In this paper, we seek to identify the geometrical requirements for GALs supporting spin-polarization, and furthermore consider the effects on the electronic structure of GALs with unit cells and holes on the nm scale. The limits of small and large holes resemble spin-unpolarized graphene and spin-polarized ZGNRs, respectively, and we therefore aim to identify the critical size for the transition. Hence, the minimum edge length required will be identified for both lattice types. We seek to identify to what extent simple rules for band gap opening found neglecting spin-magnetization remain valid in the spin-polarized cases. Additionally, we consider the stability of the polarization with respect to raised temperatures and chemical doping and finally consider the modulation of the linear optical spectra due to inclusion of spin. The applied theoretical frameworks will be presented in the following section. Then, results for the magnitude and stability of spin-polarization and band gaps are shown in Section III along with the optical response. Finally, conclusions are given in Section IV.

II. METHODS

Hexagonal graphene antidots in a triangular lattice can be characterized by a unit-cell edge length parameter L and hole edge length S , both in units of a_0 . These are defined as the number of zigzags along the edges shown in Fig. 1 for triangular GALs, agreeing with the nomencla-

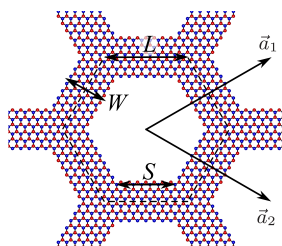


Figure 1. Excerpt of triangular GAL with hexagonal holes. W , S and L represent the sub-ribbon width, edge length and unit cell size, respectively, whereas \vec{a}_1 and \vec{a}_2 are triangular GAL lattice vectors parallel to carbon-carbon bonds. The edges are zigzags of alternating carbon atoms from the A and B sub-lattice illustrated by blue and red atoms, respectively. The dashed line indicates the unit cell.

ture of, e.g., Refs. 12, 22, and 38, making the illustrated GAL an $\{L = 10, S = 7\}$ structure. Alternatively, the structure can be envisaged as consisting of interconnected zigzag sub-ribbons of length S and width $W = L - S$, the latter indicating the number of armchairs, each of length $\sqrt{3}a_0$, connecting the two sub-ribbon edges indicated in Fig. 1. Hence, the limiting case of large S should approach the case of infinite ZGNRs of width W , whereas the case of small S approaches pristine graphene with no spin-polarization. This means that a transition region in S and L must exist where the ground state evolves from having a vanishing spin-polarization to a finite one.

We apply a model based on density-functional theory (DFT) in the local spin-density approximation (LSDA) as implemented in the SIESTA package³⁹ to investigate structures with small unit cells. We verify its agreement with a much simpler mean-field Hubbard tight-binding model, and use this to consider structures with unit cells of several thousand atoms beyond the scope of DFT. Here, characteristic properties such as optical gaps and spin-polarization become asymptotic, allowing for extrapolation to the behaviour of even larger systems.

A. Density-functional theory model

In the DFT model, all dangling bonds are hydrogen-terminated, removing them from the band gap. A double- ζ basis, with an extra polarized term (i.e., a DZP basis) and Troullier-Martins pseudopotentials⁴⁰ with only $2s$ and $2p$ electrons treated as valence for carbon, are used. Exchange-correlation is handled in the Perdew-Zunger parameterization⁴¹. A modest $2 \times 2 \times 1$ Monkhorst-Pack k -grid was found to be sufficient for k -

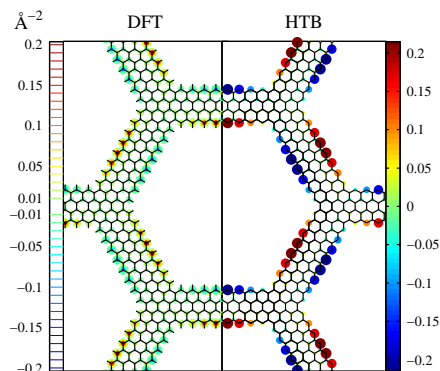


Figure 2. spin-polarization of $\{W = 2, S = 8\}$ triangular GAL, comparing the z -integrated DFT density with the onsite HTB density. Note that the DFT density is plotted as a contour plot, with contour lines at values shown in the left bar while the HTB model is a scatter plot, with dot sizes and color indicating the onsite Hubbard spin density difference.

B. LARGE AND STABLE BAND GAPS IN SPIN-POLARIZED GRAPHENE ANTIDOT LATTICES

3

space integration due to the relatively flat bands and semiconducting nature of the GALs investigated, except for the specific case of $S = 5$ where the spin-polarization was found to vanish with increasing k -grid sampling, making an $8 \times 8 \times 1$ grid necessary. Additionally, several hundred iterations were required to fully converge the spin-densities of $S = 5$ structures, whereas only tens of iterations were necessary with $S \neq 5$. A reciprocal wave vector cut-off of 150 Ry was found to be sufficient. Un-relaxed structures with ideal carbon-carbon and hydrogen-carbon bond lengths, respectively $2.46/\sqrt{3}$ Å and 1.09 Å, were used.

B. Hubbard tight-binding model

Generally, the out-of-plane π -electron system of planar conjugated carbon structures decouples from the in-plane σ system, and since the π -electrons govern optical and electronic properties of the states in the vicinity of the Fermi level we only include these in the Hubbard tight-binding (HTB) treatment. In the mean-field (Hartree-Fock) approximation, the Hubbard Hamiltonian becomes

$$\hat{H} = \sum_{i,j,\sigma} t_{ij} \hat{c}_{i\sigma}^\dagger \hat{c}_{j\sigma} + U \sum_{i,\sigma} \hat{n}_{i\sigma} (\hat{n}_{i,-\sigma}), \quad (1)$$

where $\hat{c}_{i\sigma}$ and $\hat{c}_{i\sigma}^\dagger$ are, respectively, annihilation and creation operators of electrons in atomic π -orbitals at lattice site i with spin σ . t_{ij} is the tight-binding hopping parameter between sites i and j , whereas U is the Hubbard interaction parameter coupling the $-\sigma$ spin density $\langle \hat{n}_{i,-\sigma} \rangle$ to the σ density through the occupation number operator $\hat{n}_{i\sigma} = \hat{c}_{i\sigma}^\dagger \hat{c}_{i\sigma}$. In the following, we take $U = 2.0$ eV and include up to third-nearest neighbour interaction using hopping integrals $t_1 = -2.7$ eV, $t_2 = -0.2$ eV and $t_3 = -0.18$ eV. These Hubbard and tight-binding parameters were previously shown to reproduce DFT LSDA results for ZGNRs⁴², and we here confirm that they are transferable to GAL structures by comparison with our SIESTA model. Using this Hamiltonian, the initially anti-ferromagnetic densities are iterated to self-consistency.

III. RESULTS AND DISCUSSION

As already discussed, at sufficiently large S the GALs under investigation are expected to display anti-ferromagnetic behaviour akin to what is observed for ZGNRs. This is indeed what we find, with an example shown in Fig. 2 where anti-ferromagnetic ordering is seen with respect to the A and B sub-lattices indicated by blue and red atoms in Fig. 1. At the armchair corners joining two oppositely polarized edges, polarization is strongly suppressed while a maximum is found at the edge centre atom. All spin-polarized GALs investigated here follow this general trend, and below we present a systematic

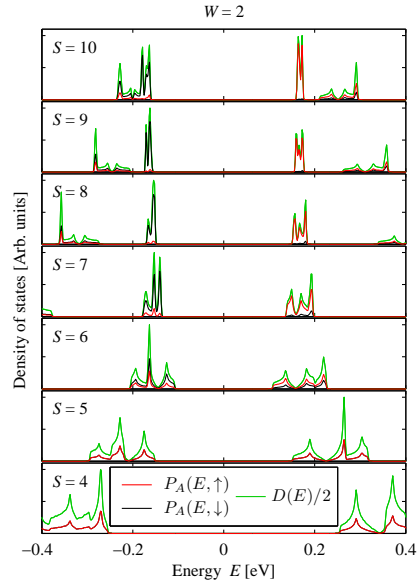


Figure 3. Density of states calculated using our HTB model for a few triangular GALs, with sub-ribbon width $W = 2$ and varying edge length S , projected onto the edge-atoms of the A sub-lattice (red and black curves) in addition to the total density of states (green curve).

investigation of the influence of the dimensions (i.e. W and S) on spin-polarization and band gaps. However, we first make some general comments on the modulation of the electronic structure upon including spin-polarization in the problem.

In Fig. 3, we display the density of states calculated for each spin projected onto the edge-atoms of the A sub-lattice $P_A(E, \sigma)$ for a $W = 2$ structure and a few edge lengths. Note that the same quantity for the B sub-lattice is found by simply interchanging spin index due to the anti-ferromagnetic symmetry of the sub-lattices, as can be readily seen from the spin-density difference in Fig. 2. By inspection of the electron wave function, the edge-localization of the states nearest the band gap was confirmed and it is clearly observed by comparison with the total density of states $D(E)$ that these dominate in this energy region. Additionally, at $S > 5$ the edge-states become spin-polarized with a clear difference in up and down densities. Interestingly, the opposite polarization is observed for edge-states just above the band gap, hinting at why spin-polarization is suppressed by occupying the lowest conduction band states by, e.g., doping. Furthermore, only states near the band gap are polarized, while states with significant weight near the edges extending further into the valence/conduction band range remain unpolarized. This trend can be seen by comparing the

weakly polarized (i.e. small difference between $P_A(E, \uparrow)$ and $P_A(E, \downarrow)$) peaks near -0.35 eV for the $S = 8$ structure in Fig. 3 with the strongly polarized peaks near -0.18 eV, where the projected density of states is almost exclusively spin down.

In order to systematically quantify the degree of spin-polarization in the investigated GALs, we use "maximum spin-polarization". In general, this value is simply the absolute spin density difference (onsite occupation for the HTB model and out-of-plane integrated density for the DFT model) found at the middle of (any) sub-ribbon edge.

A. Spin-polarization and band gap

In Fig. 4, we consider the scaling of the maximum spin-polarization (lower panel) and band gap (upper panel) with edge length S and width W . We find a characteristic length of $S = 5$ above which structures of all widths W are spin-polarized. Both DFT and HTB results display this behaviour, which can simply be interpreted as a competition between the energy gain due to polarization of the zigzag sub-ribbons and the energy penalty of polarizing the armchair corners. We note that Ref. 16 reports DFT calculations showing a weakly spin-polarized $S = 5$ structure in contrast to our findings. However, their calculations were performed using a $2 \times 2 \times 1$ k -point sampling, which we found insufficient as discussed previously.

As demonstrated in the upper panel of Fig. 4, the onset of spin-polarization coincides with a dramatic opening of the band gap in comparison to the unpolarized case for $S > 5$. Hence, spin-polarization breaks the tendency of decreasing band gap with S and leads to gaps tending asymptotically to values resembling those of spin-polarized infinite ZGNRs of similar widths W . Conversely, in calculations excluding Hubbard interaction (i.e., setting $U = 0$ eV in Eq. 1) the band gap decreases monotonically with increasing S , although with weak oscillations at $S > 10$ due to confinement effects depending on edge lengths. Hence, the band gaps of even relatively large GALs are expected to be on the order of hundreds of meV, as opposed to our previous predictions for circular holes without spin-polarization⁸, enforcing the idea of utilizing GALs in semiconductor devices.

For circular, unpolarized holes, a simple scaling law was proposed by Pedersen *et al.*⁸ for the band gap $E_g \approx \alpha N_{\text{rem}}^{1/2} / N_{\text{tot}}$, with N_{rem} indicating the number atoms removed from a unit cell that would otherwise contain N_{tot} atoms and α a fitting parameter. For the present case, in which $N_{\text{rem}}^{1/2} / N_{\text{tot}} = S / [\sqrt{6}(W + S)^2]$, we note that the band gap dependency only follows such simple scaling law for the smallest holes as demonstrated in Fig. 5. In the original work, $\alpha = 25$ eV was found by fitting to tight-binding band gaps for circular holes, whereas α was set to values ranging from ~ 4 to 25 eV by Liu *et al.*¹⁴ allowing

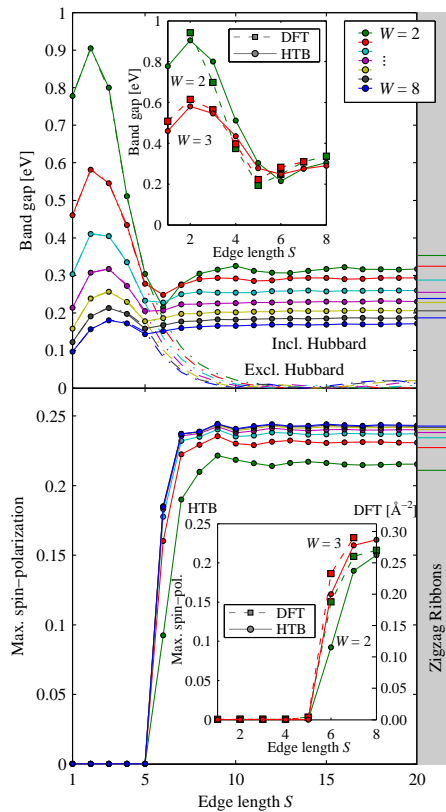


Figure 4. Band gap (top) and maximum spin-polarization (bottom) of triangular GALs of varying dimensions calculated using the Hubbard model. The band gap is seen to vanish with increasing hole size for fixed W if spin is neglected (dashed-dotted lines). However, the Hubbard interaction term introduces a finite band gap, resembling those of ZGNRs, shown in the shaded region, for large hole sizes. A band gap increase is seen at edge lengths S larger than five for all structures, matching the onset of spin-polarization. DFT results are shown in the insets, where the onset of spin-polarization is in full agreement with the HTB model. Additionally, the DFT and HTB band gaps are in reasonable agreement, with the position of the band gap minimum near $S = 5$ reproduced by both methods.

fits to triangular and rhombohedral holes. Hence, this law is widely used as a benchmark for comparing band gaps in GALs of varying geometries. For very small holes, $S = \{1, 2\}$, a good fit can be made to our results using $\alpha = 19$ eV (shown as the black line of Fig. 5) for a wide range of unit cell sizes L . However, with edge lengths $S > 2$ this tendency is broken. By adjusting the value of α and introducing corrections similar to those in Ref. 14 reasonable fits in a large range of L can still be obtained

B. LARGE AND STABLE BAND GAPS IN SPIN-POLARIZED GRAPHENE ANTIDOT LATTICES

5

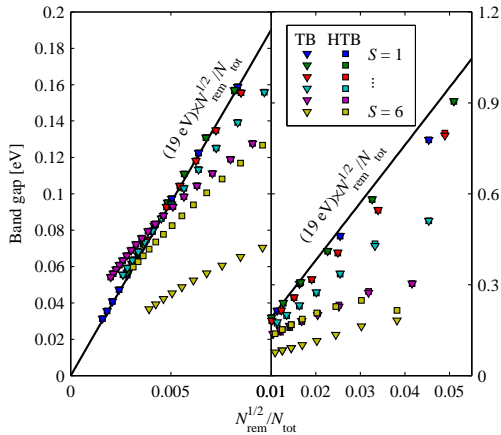


Figure 5. Comparison of the tight-binding models including (HTB) and neglecting (TB) Hubbard interaction with scaling rule of Ref. 8 (full black line).

for $2 < S < 6$. At $S > 5$, spin-polarization sets in which increases the band gap, causing a non-linear behaviour in $N_{\text{rem}}^{1/2}/N_{\text{tot}}$ clearly seen near $N_{\text{rem}}^{1/2}/N_{\text{tot}} = 0.04$ for the $S = 6$ structure. Hence, for structures with larger holes ($S > 5$), significant deviations between the simple scaling law and our results are found, becoming increasingly severe with hole size. In the limit of very small holes, however, the simple scaling law does seem to hold, as is seen in the left panel of Fig. 5. In this regime, inclusion of spin-polarization actually improves the agreement between the scaling law and the tight-binding models. For the structures produced experimentally by Shimizu *et al.*³⁶, we can estimate $N_{\text{rem}}^{1/2}/N_{\text{tot}} \sim 10^{-3}$ based on the atomic force microscopy images presented in that letter. Other fabrication techniques, such as block copolymer methods³⁰, allow $N_{\text{rem}}^{1/2}/N_{\text{tot}} \sim 0.01$. Hence, experimentally available structures are well within the regime considered here. However, we do not expect structures with extended zigzag edges to follow the above scaling law. Rather, band gaps in such structures must approach those of the nanoribbons comprising the structure. For example, the case of large S and modest W is better described by the scaling rule presented in Ref. 5: $E_g \approx 9.33 \text{ eV} \cdot \text{\AA} / (w + 15.0 \text{\AA})$ for band gaps in spin-polarized, infinite graphene zigzag nanoribbons of width $w = W\sqrt{3}a_0$.

In Ref. 14, results for rhombohedral holes in a triangular lattice with zigzag edges calculated using a nearest neighbour Hubbard tight-binding model were reported. There, a band gap increase from $\sim 250 \text{ meV}$ to $\sim 500 \text{ meV}$ with hole side length varying from $5a_0$ to $10a_0$ for constant unit-cell side length $14a_0$ was found. The opposite holds true for increasing unit cell size (between $10a_0$ and $15a_0$) with constant hole side length ($5a_0$).

Additionally, they found the ground state to be anti-ferromagnetically spin-polarized. These results agree closely with ours, even though their calculations are performed for rhombohedral holes.

Hence, the existence of a relatively short edge-length over which spin-polarization becomes a dominating effect suggests that this may indeed not be negligible in experimentally feasible systems. The question remains, however, how robust this magnetic ordering is against, e.g., temperature increase and doping levels, as will be discussed below.

B. Band gap rules for rotated hole

In Ref. 12, Petersen *et al.* formulated a semi-empirical rule stating that only every third rotated triangular GAL displays a significant band gap, requiring $L = 3n + 3$, where n is an integer and the unit cell size L for the rotated structure is defined as the number of zigzags along the unit cell edge indicated in Fig. 6. Similarly, Ouyang *et al.*¹⁵ observed an alternating semiconducting/metallic behaviour of triangular GALs with hole separation distance. Recently, Liu *et al.*⁹ demonstrated that these results are particular realizations of a universal rule governing band gap opening in all triangular super lattices spanned by integer combinations of graphene lattice vectors. We have considered a range of rotated triangular unit cells, both including and excluding Hubbard interaction, and verify this rule in the latter case. However, upon including Hubbard interaction the rotated triangular structures are found to be anti-ferromagnetically spin polarized, breaking the A - B sub-lattice symmetry. This, in turn, induces a band gap comparable to those in Fig. 4.

This is exemplified by the results in Fig. 6. No common threshold edge length S , above which all structures are spin-polarized, could be found for these structures. Instead this threshold depends on the width parameter W , in contrast to what is observed in Fig. 4. The spin-polarization (not shown) increases abruptly exactly at edge lengths where the band gaps including and excluding Hubbard interaction diverge, similarly to Fig. 4. Band gap openings similar to the ones observed here are expected for other structures, why care should be taken in generalizing the aforementioned band gap rules to any structure containing extended, possibly spin-polarized zigzag edges.

C. Doping and temperature effects

Band gaps induced by spin-polarization in ZGNRs are known to close by doping⁴³. Here, we consider to what extent a similar effect is found for the anti-ferromagnetic ordering of GALs. We investigate the effects of both thermal excitations and carriers injected by dopants or charge reservoirs such as a metallic substrate. Thermal

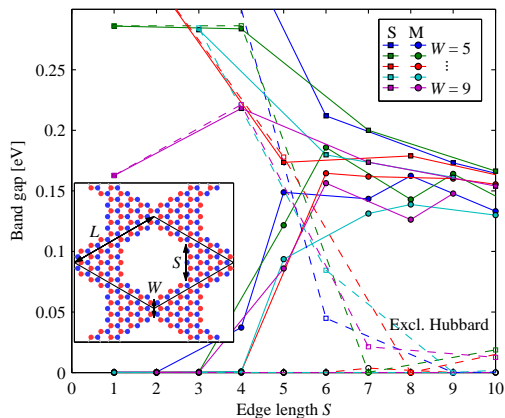


Figure 6. Band gaps of a few rotated triangular GALs calculated using the HTB model. Structures which are metallic in the absence of Hubbard interaction are denoted by circles as indicated by the "M" in the legend, whereas squares indicate semiconducting structures, denoted by "S" in the legend. The full and dashed lines indicate results including and excluding Hubbard interaction, respectively. The inset illustrates the unit cell (full black line) of the rotated triangular structure, together with the side length parameters S and L in addition to a width parameter $W = L - 2S$.

excitations are included by applying finite temperature Fermi-Dirac statistics when calculating the electron density. Thus, the bottom conduction bands displaying a spin-polarization opposite that of the top valence bands contribute to the charge density, causing an overall reduction in spin-polarization. This, in turn, causes a reduction of the band gap which allows the thermal excitation of further conduction band electrons reducing the band gap even more. The results are shown in Fig. 7 for structures of the type presented in Fig. 1, where it is clearly observed how all GALs depolarize near 1000 K, regardless of band gap.

Charge carriers injected (at zero temperature) by, e.g., chemical doping can be treated by adjusting the Fermi-level into the conduction band range at an energy yielding an electron number satisfying the chosen doping level, and the results are displayed in Fig. 8. A clear spin-depolarization (and hence decreasing band gap) is observed with increasing number of injected electrons. However, for all ribbons a complete depolarization is only observed at relatively high doping levels close to one percent increase in electrons per unit cell relative to the intrinsic case. Additionally, all GALs appear increasingly sensitive towards doping with increasing W for constant S . This trend can be understood by noting that the number of edge-states is proportional to the edge length S , while the number of doping electrons scales with the number of atoms per unit cell (the doping levels are given

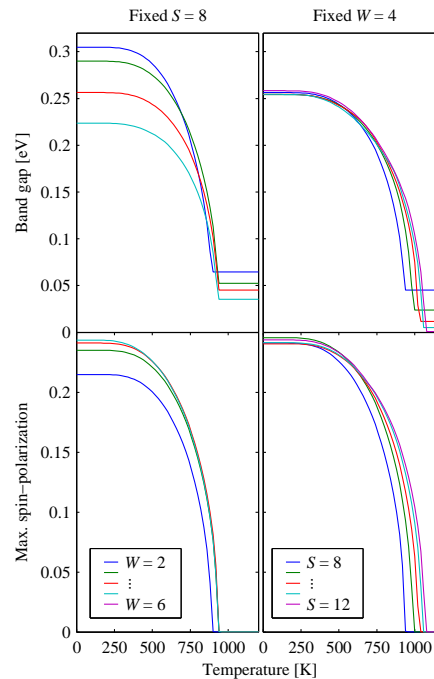


Figure 7. Band gap and maximum spin-polarization of several triangular GALs at varying temperatures calculated using the HTB model. All species tend to depolarize at temperatures larger than approximately 1000 K, regardless of band gap.

in percentages of electrons per unit cell) and hence W . Thus, with increasing W and constant S , the doping level per edge-state increases. These edge-states are energetically located near the conduction band minimum with spin-polarization anti-symmetric to those of the top valence bands, as discussed previously. It follows that occupation of conduction band edge-states causes an overall spin-depolarization. We note that in order to accurately model chemical doping at the highest levels considered here, modulations of the band structure should be taken into account^{44,45}, but this complication is ignored here.

D. Linear optical response

Noting the dramatic effects of spin-polarization on the band structure near the band gap, we expect substantial modifications of the optical properties of GALs relative to results calculated neglecting Hubbard interaction, e.g., in Ref. 20. We calculate the optical conductivity using the method described in that paper both including and excluding Hubbard interaction for triangular GALs of $W = 2$, and present the results in Fig.

B. LARGE AND STABLE BAND GAPS IN SPIN-POLARIZED GRAPHENE ANTIDOT LATTICES

7

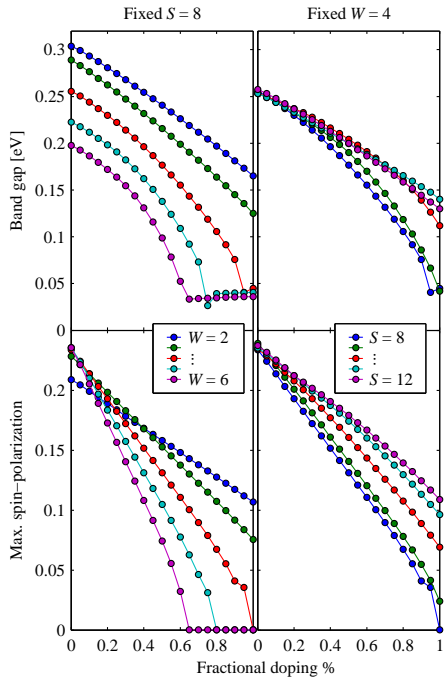


Figure 8. Band gap and maximum spin-polarization of triangular GALs calculated for various doping levels and structure parameters using the HTB model.

9. The optical spectra for small holes ($S < 5$) are nearly identical regardless of Hubbard interaction, however, for larger structures ($S > 5$) dramatic modulations in the optical spectra are found. Most notably, the band edge transition is blue-shifted by several hundred meV due to spin-polarization as might be expected due to the changing band gap. Additionally, the peak shapes tend to differ slightly for larger holes due to the flattening of the edge-state bands upon inclusion of Hubbard interaction. We note that the results presented here are calculated neglecting complications such as excitonic effects or electron-phonon interaction. While such phenomena are expected to affect the optical response to some extent, the single-particle spectra remain an important first approximation, demonstrating the impact of spin-polarization on a readily measurable quantity. An equally dramatic impact on the transport properties of GALs with hole edge lengths larger than $5a_0$ might also be expected.

IV. CONCLUSION

The ground state electron densities of graphene antidot structures with hexagonal holes in a triangular lattice

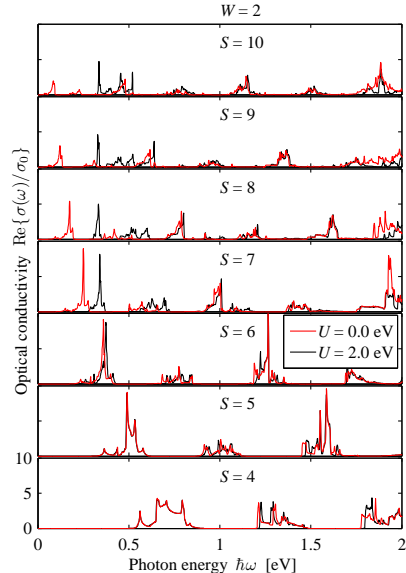


Figure 9. Optical response of various triangular $W = 2$ GALs from the HTB model in units of the static conductivity of graphene $\sigma_0 = e^2/(4h)$.

display anti-ferromagnetic spin-polarization similarly to what is observed for graphene zigzag nanoribbons, but only for hole sizes with an edge length larger than five graphene lattice constants. This has a large effect on the band structure near the Fermi level, with a substantial band gap increase of several hundred meV. Also, structures with a rotated hole, previously reported to display an alternating semiconducting/metallic behaviour with increasing unit cell size, were found to be purely semiconducting with the inclusion of spin-polarization and modest hole sizes. For antidots with extended zigzag edges, this result questions the validity of simple scaling laws and rules for band gap opening based on calculations neglecting spin-polarization.

The states near the band gap are localized at the graphene edges and display a strong spin-polarization, with the states just above or below the Fermi level being oppositely polarized. Thus, with increasing temperature and doping, electrons occupy edge bands on both sides of the band gap. This results in a net reduction of the spin-polarization and consequently reduced band gaps. However, the spin-polarization is only negligible at temperatures larger than ~ 1000 K and doping at the percent level, enforcing that spin-polarization should be included in any study of larger graphene antidot lattices having zigzag edges. The increased band gap has a clear impact on the optical properties of GALs, demonstrating the importance of including this type of interaction when

calculating physical observables such as optical response.

ACKNOWLEDGEMENTS

TGP gratefully acknowledges the financial support from the Center for Nanostructured Graphene (project

DNRF58) financed by the Danish National Research Foundation. We thank J. G. Pedersen and A.-P. Jauho for useful comments on the manuscript.

-
- * mlt@nano.aau.dk
- ¹ K. S. Novoselov, V. I. Fal'ko, L. Colombo, P. R. Gellert, M. G. Schwab, and K. Kim, *Nature* **490**, 192 (2012).
 - ² A. S. Mayorov, R. V. Gorbachev, S. V. Morozov, L. Britnell, R. Jalil, L. A. Ponomarenko, P. Blake, K. S. Novoselov, K. Watanabe, T. Taniguchi, and A. K. Geim, *Nano Lett.* **11**, 2396 (2011).
 - ³ A. Reina, X. Jia, J. Ho, D. Nezich, H. Son, V. Bulovic, M. S. Dresselhaus, and J. Kong, *Nano Lett.* **9**, 30 (2009).
 - ⁴ B. Obradovic, R. Kotlyar, F. Heinz, P. Matagne, T. Rakhshit, M. D. Giles, M. A. Stettler, and D. E. Nikonov, *Appl. Phys. Lett.* **88**, 142102 (2006).
 - ⁵ Y.-W. Son, M. L. Cohen, and S. G. Louie, *Phys. Rev. Lett.* **97**, 216803 (2006).
 - ⁶ E. McCann, *Phys. Rev. B* **74**, 161403 (2006).
 - ⁷ Y. Zhang, T.-T. Tang, C. Girit, Z. Hao, M. C. Martin, A. Zettl, M. F. Crommie, Y. R. Shen, and F. Wang, *Nature* **459**, 820 (2009).
 - ⁸ T. G. Pedersen, C. Flindt, J. Pedersen, N. A. Mortensen, A.-P. Jauho, and K. Pedersen, *Phys. Rev. Lett.* **100**, 136804 (2008).
 - ⁹ X. Liu, Z. Zhang, and W. Guo, *Small* **9**, 1405 (2013).
 - ¹⁰ J. A. Fürst, J. G. Pedersen, C. Flindt, N. A. Mortensen, M. Brandbyge, T. G. Pedersen, and A.-P. Jauho, *New J. Phys.* **11**, 095020 (2009).
 - ¹¹ R. Petersen and T. G. Pedersen, *Phys. Rev. B* **80**, 113404 (2009).
 - ¹² R. Petersen, T. G. Pedersen, and A.-P. Jauho, *ACS Nano* **5**, 523 (2011).
 - ¹³ H. Y. He, Y. Zhang, and B. C. Pan, *J. Appl. Phys.* **107**, 114322 (2010).
 - ¹⁴ W. Liu, Z. F. Wang, Q. W. Shi, J. Yang, and F. Liu, *Phys. Rev. B* **80**, 233405 (2009).
 - ¹⁵ F. Ouyang, S. Peng, Z. Liu, and Z. Liu, *ACS Nano* **5**, 4023 (2011).
 - ¹⁶ D. Yu, E. M. Lupton, M. Liu, W. Liu, and F. Liu, *Nano Res.* **1**, 56 (2008).
 - ¹⁷ L. Chen, D. Yu, and F. Liu, *Appl. Phys. Lett.* **93**, 223106 (2008).
 - ¹⁸ H.-X. Yang, M. Chshiev, D. W. Boukhvalov, X. Waintal, and S. Roche, *Phys. Rev. B* **84**, 214404 (2011).
 - ¹⁹ J. J. Palacios, J. Fernández-Rossier, and L. Brey, *Phys. Rev. B* **77**, 195428 (2008).
 - ²⁰ T. G. Pedersen, C. Flindt, J. Pedersen, A.-P. Jauho, N. A. Mortensen, and K. Pedersen, *Phys. Rev. B* **77**, 245431 (2008).
 - ²¹ T. G. Pedersen and J. G. Pedersen, *J. Appl. Phys.* **112**, 113715 (2012).
 - ²² T. Gunst, T. Markussen, A.-P. Jauho, and M. Brandbyge, *Phys. Rev. B* **84**, 155449 (2011).
 - ²³ L. Rosales, M. Pacheco, Z. Barticevic, A. León, A. Latgé, and P. A. Orellana, *Phys. Rev. B* **80**, 073402 (2009).
 - ²⁴ Y.-T. Zhang, Q.-M. Li, Y.-C. Li, Y.-Y. Zhang, and F. Zhai, *J. Phys.: Condens. Matter* **22**, 315304 (2010).
 - ²⁵ H. Jippo, M. Ohfuchi, and C. Kaneta, *Phys. Rev. B* **84**, 075467 (2011).
 - ²⁶ C. Tao, L. Jiao, O. V. Yazyev, Y.-C. Chen, J. Feng, X. Zhang, R. B. Capaz, J. M. Tour, A. Zettl, S. G. Louie, H. Dai, and M. F. Crommie, *Nature Phys.* **7**, 616 (2011).
 - ²⁷ O. V. Yazyev, R. B. Capaz, and S. G. Louie, *Phys. Rev. B* **84**, 115406 (2011).
 - ²⁸ J. Fernández-Rossier, *Phys. Rev. B* **77**, 075430 (2008).
 - ²⁹ S. R. Power, V. M. de Menezes, S. B. Fagan, and M. S. Ferreira, *Phys. Rev. B* **84**, 195431 (2011).
 - ³⁰ M. Kim, N. S. Safron, E. Han, M. S. Arnold, and P. Gopalan, *Nano Lett.* **10**, 1125 (2010).
 - ³¹ J. Bai, X. Zhong, S. Jiang, Y. Huang, and X. Duan, *Nature Nanotechnol.* **5**, 190 (2010).
 - ³² M. Begliarbekov, O. Sul, J. Santanello, N. Ai, X. Zhang, E.-H. Yang, and S. Strauf, *Nano Lett.* **11**, 1254 (2011).
 - ³³ J. Eroms and D. Weiss, *New J. Phys.* **11**, 095021 (2009).
 - ³⁴ X. Jia, M. Hofmann, V. Meunier, B. G. Sumpter, J. Campos-Delgado, J. M. Romo-Herrera, H. Son, Y.-P. Hsieh, A. Reina, J. Kong, M. Terrones, and M. S. Dresselhaus, *Science* **323**, 1701 (2009).
 - ³⁵ Ç. Ö. Girit, J. C. Meyer, R. Erni, M. D. Rossel, C. Kisielowski, L. Yang, C.-H. Park, M. F. Crommie, M. L. Cohen, S. G. Louie, and A. Zettl, *Science* **323**, 1705 (2009).
 - ³⁶ T. Shimizu, J. Nakamura, K. Tada, Y. Yagi, and J. Haruyama, *Appl. Phys. Lett.* **100**, 023104 (2012).
 - ³⁷ E. H. Lieb, *Phys. Rev. Lett.* **62**, 1201 (1989).
 - ³⁸ J. A. Fürst, T. G. Pedersen, M. Brandbyge, and A.-P. Jauho, *Phys. Rev. B* **80**, 115117 (2009).
 - ³⁹ D. Sánchez-Portal, P. Ordejón, and E. Canadell, *Struct. Bond.* **112**, 113715 (2004).
 - ⁴⁰ N. Troullier and J. L. Martins, *Phys. Rev. B* **43**, 1993 (1991).
 - ⁴¹ J. P. Perdew and A. Zunger, *Phys. Rev. B* **23**, 5048 (1981).
 - ⁴² Y. Hancock, A. Uppstu, K. Saloriutta, A. Harju, and M. J. Puska, *Phys. Rev. B* **81**, 245402 (2010).
 - ⁴³ W. Zhu, G. Ding, and B. Dong, *Appl. Phys. Lett.* **100**, 103101 (2012).
 - ⁴⁴ A. Lherbier, X. Blase, Y.-M. Niquet, F. Triozon, and S. Roche, *Phys. Rev. Lett.* **101**, 036808 (2008).
 - ⁴⁵ L. Ci, L. Song, C. Jin, D. Jariwala, D. Wu, Y. Li, A. Srivastava, Z. F. Wang, K. Storr, L. Balicas, F. Liu, and P. M. Ajayan, *Nature Mater.* **7**, 430 (2010).